STUDY ON IDENTIFICATION OF PEAT FIRE RISK AREA USING POLARIMETRIC AND INTERFEROMETRIC SYNTHETIC APERTURE RADAR

August 2020

JOKO WIDODO

Graduate School of Advanced Integration Science

CHIBA UNIVERSITY

(千葉大学審査学位論文)

STUDY ON IDENTIFICATION OF PEAT FIRE RISK AREA USING POLARIMETRIC AND INTERFEROMETRIC SYNTHETIC APERTURE RADAR

偏波・干渉合成開口レーダ解析による泥炭地火災危険地域の検出評価

2020 年 8 月

JOKO WIDODO

ジョコ　ウィドド

大学院融合科学研究科

千葉大学

Declaration

I hereby declare that this submission is my own work and that, to the best of my knowledge and belief, it contains no material which to a substantial extent has been accepted for the award of any other degree or diploma of university or other institutes of higher learning, except where due acknowledgment has been made in the text.

Joko Widodo, August 2020

Abstract

Most of the forest fire in Indonesia occurs in peatland areas. High potential forest fire takes place in dry peat that has a groundwater table more than 40 cm. The fire will cause degradation of the peatland. This thesis describes a novel method to detect peat fire risk by combining the impedance model and the Differential Interferometric SAR (DInSAR) technique in Siak, Riau Province, Indonesia, based on the groundwater table's annual subsidy. In this study, the current impedance model was then modified by incorporating surface roughness. The proposed method was then validated with groundwater table data. This work has successfully identified the peat area with fire risk by impedance model and DInSAR method in the dry peatland using backscattering coefficient simulation. The results from model simulation show that the dry peat has an average backscattering coefficient of -13.97 dB, with -11.5 dB of the minimum value, and -17.29 dB of the maximum value. The correlation coefficient from the backscattering coefficient between model simulation and ALOS-2/PALSAR-2 data is 0.8, with an average root square error of 1.4. Correlation between the measurement and the model of the groundwater table using two model of pair A and pair B show the result of 0.71 and 0.85, respectively. The overall results disclose that peat fire hazard areas were successfully identified using both methods. The dielectric constant of the peat soil indicated the risk of the peat fire due to high dry soil conditions in the research areas. Two models were suggested to obtain precise detection data. Moreover, another study in Kalimantan also shown that the identification of degraded peatland associate with forest fire based on DInSAR method using ALOS-2 data is more accurate compared to Water Table Depth Stations that installed in the field.

アブストラクト

インドネシアにおける森林火災のほとんどが泥炭地帯に集中しており，特に地下水位が 40cm 以下の乾燥した泥炭地では大きな火災危険性を伴う．本論文では，年間の地下水位変化に基づいた，インドネシア・リアウ州シアク区におけるインピーダンスモデルと差分干渉合成開口レーダ（DInSAR）解析による泥炭地火災危険地域の特定に関する研究を行った．本研究では従来のインピーダンスモデルに土壌表面粗度を導入したモデルを提案した．この手法は地下水位の現地観測データにより検証を行った．本研究は乾燥泥炭を想定した後方散乱係数のシミュレーションに基づくインピーダンスモデルにより，泥炭火災危険地域の予測に成功した．シミュレーションモデルより、乾燥した泥炭地における後方散乱係数の平均値，最小値，最大値はそれぞれ-13.97dB，-11.5dB，-17.29dB を取得した．またシミュレーションと ALOS-2 データから得られた後方散乱係数の相関係数は 0.8 で、平均二乗誤差は 1.4 である．更に DInSAR による乾燥泥炭地域の観測が可能であることを示した．現地観測値とモデルによる地下水位の相関係数はペア A で 0.71，ペア B で 0.85 の結果である．両結果より、泥炭火災危険地域の検出が可能であることを示唆した．また，泥炭土壌の誘電率は高い乾燥度は泥炭火災のリスクを示唆した．また，ボルネオ島の場合，ALOS-2 データの DInSAR 解析により森林火災で荒廃した泥炭地の観測が

可能であることがわかった。将来、本研究で得た手法が泥炭火災危険地域のモニタリングに活用できると期待する。

Acknowledgments

By the grace of God, this research work has been accomplished.

This research work is part of the Synthetic Aperture Radar project in tropical peatland of Indonesia under The Josaphat Microwave Remote Sensing Laboratory (JMRSL) and Centre of Environmental Remote Sensing (CEReS), Chiba University.

I would like to express my gratitude to Prof. Josaphat Tetuko Sri Sumantyo as an academic supervisor for all sincere guidance, supports, and advice. I would like to extend my sincere thanks to my co-supervisor, Prof. Hiroaki Kuze, for his support during my study.

I would also like to extend my highest appreciation to my co-researchers: Yuta Izumi, Ayaka Takahashi, Husnul Kausarian, Daniele Perissin, Albertus Sulaiman, Awaluddin, Agung Riyadi, Mohammad Nasucha, especially to Husnul Kausarian for all of the coordination supporting during a field survey in Siak, and Yuta Izumi and Ayata Takahashi for accompanying during a field survey in the Siak Regency, and all of JMRSL members, Center of Environmental Remote Sensing, Chiba University

Special thanks to my senior and colleagues at the Agency for The Assessment and Application of Technology (BPPT): Dr. Ir. Hammam Riza, APU (Head of BPPT), Ir. Yudi Anantasena, M.Eng (Deputy of TPSA BPPT), Dr. Eng. Rudi Nugroho, M.Eng (Head of Center for Environmental Technology), Dr. Arie Herlambang, all of PTL members, and all of LSP-TLIP members.

I present this research thesis to my family: my beloved wife Devitra Saka Rani, my two sons Jovi Rauhillah Wiranu and Alviko Ishaq Wiranu who have sacrificed

everything to accompany their father to study in Japan, my parents and parents-in-law, and brothers and sisters and younger siblings, especially Dwi Riyantoro and Nurhayati. They made everything easy when I first came to Japan.

Finally, thank you profusely for the Ministry of Research and Technology, Program RISET-Pro, World Bank Loan, who has provided scholarships for my Ph.D., Local Government Siak Regency, and Faculty Geology, Universitas Islam Riau for all of supporting during the survey in Siak Regency

Content

Declaration iii

Abstract iv

Acknowledgments vii

Content ix

List of Tables xii

List of Figures xiii

Chapter 1. Introduction 1

1.1. Research Background 1

1.2. Motivation 7

1.3. Objectives 7

1.4. Outline 7

Chapter 2. Technical Background and Related Works 8

2.1. Technical Background of Research 8

2.1.1. Synthetic Aperture Radar 8

2.1.3. Polarimetric Synthetic Aperture Radar 15

2.1.4. Interferometric Synthetic Aperture Radar 24

2.2. Related Works 42

2.3. State of The Arts 44

Chapter 3. Proposed Method 45

3.1. SAR Polarimetry Method 45

3.2. SAR Interferometry Method 48

3.3. Backscattering Coefficient of Satelite Data. 51

3.4. Flowchart of Research 52

3.4.1. Research 1 (Location: Siak Regency, Sumatera, Indonesia) 52
3.4.2. Research 2 (Location: Pulang Pisau, Central Kalimantan, Indonesia) ……..53
3.5. Material and Field Survey 54
3.5.1. Material 54
3.5.2. Field Survey 54
Chapter 4. Result and Discussion 60
4.1. Identification of peatland in the field area..... 60
4.2. Relationship between the dielectric constant water table depth (groundwater) in Peatland 62
4.3. Relationship between backscattering coefficient (sigma zero) and water table depth (groundwater) in Peatland..... 66
4.4. Identification of flammable peatland area based on transmission line theory …….69
4.5. Identification of flammable peatland area based on the DInSAR method …….73
4.6. Assessment of degraded peatland based on DInSAR and groundwater table depth stations related to forest fire..... 79
4.6.1. Degraded of peatlands based on DInSAR..... 79
4.6.2. Review of groundwater table station's effectivity to detect degraded peatland area related to the forest fire..... 81
Chapter 5. Conclusion..... 90
Chapter 6. Summary..... 92
6.1. Summary of The Work..... 92
6.2. Contribution..... 93
6.3. Originality 93

6.4. Significance of Work 94
6.5. Limitation of Research 94
6.6. Future Work 95
Appendix – List of Publications 96
1. Peer-reviewed Journal Papers 96
2. Conference Papers 96
Bibliography 100

List of Tables

Table 2. 1. Detail history of Space-borne Radar Launched in the world. 10
Table 3. 1. Specification of ALOS-2 PALSAR-2 data …… ……54
Table 3. 2. Sampling coordinate in Siak Regency, Riau Province 56
Table 3. 3. Position of Water Table Depth Stations in Kalimantan 58
Table. 4. 1. pH content in Peatland……60
Table. 4. 2. The dielectric constant and groundwater table level data among all of the samples 63
Table. 4. 3. Table of Bacscatteing Coefficient among sampling point 67
Table. 4. 4. Table of coefficient correlation and coefficient determination between the backscattering coefficient and groundwater table 68
Table. 4. 5. Incident angle and soil roughness captured from satellite data and the ground 69
Table. 4. 6. Backscattering Coefficient captured from ALOS-2 PALSAR-2 data and based on the simulation model 70
Table. 4. 7. Subsidence rate and simulation of groundwater in Siak Regency 75
Table. 4. 8. Data of forest fire occurred in Pulang Pisau, Kalimantan and degraded peatland based on DinSAR and indicated by groundwater level stations..... 86

List of Figures

Figure 2. 1. Microwave Sensor Classes [45]..... 9
Figure 2. 2. Concept of synthetic aperture [45] 12
Figure 2. 3. "Doppler" beam-sharpener [45]..... 14
Figure 2. 4. Polarization ellipse in the x-y plane, in the z-direction [45]..... 16
Figure 2. 5. Sketches of polarization base on various combinations of rotation angle and ellipticity angle for a wave direction out of the page [45] 17
Figure 2. 6. Wave traveling of linear polarization in the +z direction [45] 18
Figure 2. 7. Circuit of transmission line theory segment Δz [50] 19
Figure 2. 8. Interferometric cross-track setups in (a) and (b) [45]..... 26
Figure 2. 9. InSAR geometry parallel-ray approximation of R1 = R and R2 = R− β [45] 27
Figure 2. 10. The illuminated swatch is centered in an angle about a middle look angle [45] 30
Figure 2. 11. Component of baseline (parallel and perpendicular) [45] 32
Figure 2. 12. Cross-correlation between image 1 and image 2 [45] 33
Figure 2. 13. Decorrelation model imaging geometry [45] 36
Figure 2. 14. Comparison between the unwrapped phase wrapped phase and unwrapped topographic phase of the interferogram [45]..... 39
Figure 2. 15. Sample Image of Interferogram Processing (a) SAR Image, (b) Interferogram, (c) correlation between interferogram component (d) topography image [45] 41
Figure 3. 1. The basic model of the research [63]…….45
Figure 3. 2. Mechanism of scattering between layers [63] 46
Figure 3. 3. Flowchart of the research in Siak Regency [63]..... 52
Figure 3. 4. Flowchart combination method based on DInSAR and Ground Water Table Depth. [44] 53
Figure 3. 5. Sampling position in Siak Regency..... 55
Figure 3. 6. a) GPS measurement, b) Sampling of water level in peatland c) SR measurement, d) soil collection, e) Dielectric constant analysis in JMRSL [63] . 57

Figure 3. 7. Distribution of Water Table Depth Stations in Kalimantan 59
Figure 4. 1. Geological Map and Yamaguchi 4 Component Polarimetric Decomposition in RGB of Peatland in Siak, Riau Province, Indonesia [11] ……61
Figure 4. 2. Land cover and Scene boundary of ALOS-2 PALSAR-2 data used for Central Kalimantan Study (Research 2) [24] 62
Figure 4. 3. Graph that shown correlation between groundwater table and real part of dielectric constant [20]..... 65
Figure 4. 4. Graph that shown relationship between groundwater table and imaginary part of dielectric constant [20] 65
Figure 4. 5. Image of ALOS-2 PALSAR-2 data of Siak Regency, Riau, Indonesia, base on (a) Horizontal-Horizontal, (b) Horizontal-Vertical, (c) Vertical-Horizontal, and (d) Vertical-vertical polarization 66
Figure 4. 6. Relationship backscattering based on satellite data and simulation [20] 72
Figure 4. 7. (a) Coherence map and (b) Interferogram of Pair A, and (c) Coherence Map and (d) Interferogram of Pair B [20]..... 74
Figure 4. 8. The fire occurred in peatland areas during a field survey 76
Figure 4. 9. The relationship among the groundwater table simulation of Pair A (red line) and Pair B (blue line) and field survey data. [20] 77
Figure 4. 10. (a) Peat fire risk area shown in red color (b) Backscattering coefficient of ALOS-S PALSAR-2 data (c) Peat fire risk area on RGB composite of Yamaguchi Decomposition (d) Subsidence rate of of PaIr A, and (e) Subsidence rate of Pair B [20]..... 78
Figure 4. 11. (a) Coherence map; (b) image of phase interferogram; and (c) land subsidence map over google earth application [24] 80
Figure 4. 12. Degraded and un-degraded peatland area in Kalimantan based on DInSAR and Woosten Model 81
Figure 4. 13. Real-time water table depth graph of 13 stations of Pulang Pisau and Kapuas Regency [24] 83

Figure 4. 14. Map of degraded peatland areas, and position of groundwater level station related to the forest fire in Pulang Pisau and Kapuas Regency in Kalimantan [24]. 87
Figure 4. 15. Forest fire in the peatland area, Kalimantan that occurred in the open area [73]. 88

Chapter 1. Introduction

1.1. Research Background

The Josaphat Microwave Remote Sensing Laboratory (JMRSL) is a laboratory under the Centre of Environmental Remote Sensing (CEReS), Graduate School of Advanced Integration Science, Chiba University, Japan with a research focus on remote sensing, and particularly on Synthetic Aperture Radars.

One of a priority of JMRSL research is the use of Synthetic Aperture Radar in the assessment of tropical peatland in Indonesia through the establishment of a Memorandum of Understanding (MoU), with various stakeholders in Indonesia including the local government of Siak Regency in Riau Provence, and the Agency for The Assessment and Application of Technology (BPPT) Indonesia.

The landmass of Indonesia contains about 12 percent of approximately 14.9 million hectares of peatland, several of which are Sumatra, around 7.1 million hectares, 6.5 million hectares of Kalimantan, and other areas of Papua[1]. The region of peat forests are vulnerable to anthropogenic operations, for example, irrigation, conversion of seed, burning, and fuel, and the mining of biomass [2]. Human activities have increased rapidly over the past two decades and have triggered significant environmental changes [3][4]. Drainage and forestry clearance threaten the stability of peatlands and make them fire-prone [4]. The land clearance also occurs in the wildlife areas with the highest cleared peatland areas are in Riau, Central Kalimantan, and South Sumatra, with a total area of 450,000 ha, 400,000 ha, and 320,000 ha, respectively [5].

The biggest problem in Indonesia is a forest fire that started in 1982. About 75% of forestry fire occurred in peatlands and predominantly in open areas [5]. During 1990- 2015, Indonesia has lost the woodlands about 27.5 million ha due to fires,

logging, and land conversion of palm oil plantation. Only 44.5 million ha of the forest is remaining to be covered in the land. In 1997/1998 and 2006, the worst forest fires took place 140,000 hotspots during El Nino. This situation was similar in 2015 when forest fires began in late June 2015 and were stopped only despite the fact that the rainy season starts in November 2015 [6][7]

In July and October 2015, Indonesia's land has burnt 2.6 million hectares, which is equal to four and a half times Bali Island's size. About 100,000 hotspots have been used to make the land for agriculture and access to land cheaply by man-made fires. More than 100 000 hectares had been burnt out in 8 provinces, namely Papua, Riau, Jambi, West Kalimantan, South Sumatera, Central Kalimantan, South, and East Kalimantan. The hardest fire has appeared on Sumatera and Kalimantan Island, with a total of the burned area of 23% and 16%, respectively. Most of the burned areas are peatlands [6].

The rainforest that is destroyed by fires is a home for orangutan (Pongo sp.), rhinoceroses (Dicerorhinus sumatrensis harrissoni), tiger (Panthera tigris), and Asian elephant (Elephas maximus). The fire and the smoke affected to orangutan habitats in Kalimantan, as well as elephant and tiger habitats in Sumatra Indonesia. This forest fire is the fifth rank among the highest emitters of greenhouse gases—afterward, forest fires in 2015, Indonesia still in the fourth rank of the largest emitter. During 2000-2005, Annual wood and peat degradation in Indonesia emissions stood to approximately 800 million tons of CO2, nearly equal to the yearly German emissions. Around 3.66 billion tones of CO2 were emitted only from Riau province in the period of 1990-2007. As much as 1.39 billion tons were emitted from peat soils combustion whereas 0.78 billion tons of CO2 emitted through decomposition in drained peat soils [6]

The country suffered considerable economic losses from an Indonesian forest fire and crop smog, some $200million in 1997-2007 [7], and at least $16.1billion in 2015 or equivalents of 1.9 percent of GDP [5]. The burning and smog of forests

impacted even countries, including Malaysia, Singapore, Thailand, and Brunei [6] in neighboring countries.

Indonesia has the intention to participate in forest fire prevention programs, and both the international and community level, as prevention is the effective key to handle forest fire. Effective tracking and collection of data should be performed, along with the necessity of early warning systems at the provincial level [7]. Fire Danger Rating System (FDRS) that developed for Indonesia and applied from 2004 is one good monitoring system based on temperature, relative humidity, wind speed, and rainfall. The result of this monitoring system is defined as The Fire Weather Index (FWI) [8].

The application of remote optical sensing information, for example, MODIS satellite data, has demonstrated the ability to recognize number large fuel connection scales patterns that possible to monitor fire hazard patterns using the theory of the graph[9]. Remote sensing is at the forefront in developing fuel maps for evaluation live fuel humidity amongst most notably important fire system components: topography, fuel, and weather[10]. The NOAA-AVHRR is also confirmed that optional input data, in particular, in the detection and comprehension of soil moisture as a fire hazard indicator[11]. The main issues with optical remote sensing are that information about the surface of the soil is only available in a clear condition and at day. In a different circumstance, synthetic opening radar (SAR) provides surface information that has the benefit of penetrating cloud cover, penetrating rain in a certain depth, and operating at night. All these competencies are important to add optical impairment [12] and offer a substantial reason for using the study SAR data.

The SAR data analysis [14] showed the close relationship between the Backscattering coefficient and FWI by RADARSAT-1 C-Band SAR in Canada. Other research studies have evaluated the ERS sensor for fire hazard prediction in a boreal area where there is also a significant correlation among burning backscatter,

backscatter forest, and FWI [13]. The study from Chavez et al. [14] reveals a method for monitoring surface soil moisture by spatial and temporal monitoring in the disrupted boreal forest, whereas Tanase et al. [15] gave a method for monitoring live fuel moisture in semi-arid areas. Recently, JMRSL developed a novel soil moisture recovery that utilizes data from SAR regarding peat fire risk monitoring [16].

In the context of the Advanced Land Observation Satellite (ALOS) operated by Japan Exploration Space Agency (JAXA), it consists of PALSAR, PALSAR-2, and the next PALSAR-3 are famous SAR L-Band Frequency sensors. These sensors can be used as inputs to track the different conditions in the peatland field, as an example changes in soil moisture, forest biomass, detection of peat dome, peat density, and subsidence of peat [17] and groundwater table [18].

The groundwater level has a correlation with the fire in the peatland region. The peatlands are easier to burn when the groundwater level is low. The groundwater level is a great indicator for mapping the peat fire risk area [19]. Indonesia's Regulation states that peatlands of more than 40 cm groundwater level are protected by depletion of bogs [20] [21] and have high fire potential.

Furthermore, ALOS data works effectively for detecting soil moisture [22] burn coal seam thickness [23] of fire scars [24], topsoil thickness [25], and layer thickness estimates for silica sand distribution [26]. All of the applications are using impedance models that correlate with dielectric constants, incident angles, and backscattering coefficients. Nevertheless, contrary to actual conditions on the ground, the impedance model is built without surface roughness.

Some studies have shown that the DInSAR technique has been used to detect the area of peat degradation. DInSAR mainly extracts the differences in phase among SAR images then converts information for deformation (land subsidence) after removing interferogram topography contribution using a Digital Elevation

Model[27]. Many studies have used subsistence data to suggest degraded peatlands and to get the groundwater table information and others in the peatland region[28][29][17][30].

New impedance models and the DInSAR method were used in this research to identify peatland areas at risk. This new model of impedance considers the soil roughness parameter to be a new circuit model parameter and an independent layer to improve an impedance model based on the transmission line theory. This is a step forward relative to others in this research [22]-[26]. The combination of the impedance model and DInSAR provides more accurate analytical results using phase information from the SAR image. The method that combining those model is an innovation in the fields regarding peat fire detection compared to previous studies [9]-[15]. The addition of surface roughness parameters combining with DInSAR offers benefits by means of accurateness of model impedance analysis and reciprocal cross-checking.

This research also compared the identification of degraded peatlands using the DInSAR method and table of water depth station regarding forest fire. Table of Water (WT) (also known as water table depth or groundwater level) is now widely accepted to be a central parameter in the peatland research safety. The decline of the WT depth is driving many negative peat processes, such as carbon decomposition, fire susceptibility, increased production of methane (CH4), etc. [31][32][33][34]. The reduction of WT scope contributes in principle to emissions of greenhouse gases. WT is thus the critical criterion for determining whether the peatland is degraded.

There can be a variety of approaches to identifying degraded peatlands, including biogeochemical use as an indicator[35]. C, N, ash content, carbon age parameters, volume density, can, however, not all be used quantitatively whether the peatland is degraded or not. In conjunction with many optical remote sensing devices, such as aerial image datasets and Compact Airborne Spectrographic Imager (CASI).

Light Detection and Ranging (LIDAR) techniques are also beneficial for detecting and mapping degraded peatland over typical terrestrial surveys [36]. The measurement of soil moisture and water table depth is crucial parameters that have been investigated by a remote sensor, particularly remote sensing microwave [18][16].

Synthetic Aperture Radar (SAR) microwaves remote sensing was used extensively to perform subsidy mapping on peatlands with the SAR (InSAR) technique [37][29][38][28]. Data about subsidence of bogs is relevant because it has to do with a number of issues, such as depth levels at the water table and carbon emissions [39]. Peatland subsidies (in cm/year), which was found, are equal to the water table depth (in cm) multiplied by 0.04 [30]. Peatlands fire is one of Indonesia's major problems. The fires generally occur in peatlands area with water table depth is more than 40 cm [40]. The regulations also denote that the peatlands with the value of water table depths are more than 40 cm is classified as degraded areas [41] [21]. This circumstance allows the fire to spread to dry peat quickly.[30][40] [20][21][42][42][43].

This work also uses the Interferometry SAR method to classify degraded peatlands linked to forest fire with data from ALOS-2 PALSAR-2 then compares them with the real-time WT depth monitoring system. In conjunction with the Peatland Restoration Agency (BRG) Indonesia, SIPALAGA, BPPT has developed an in real-time WT depth monitoring system. This system measured the depth of the water table, soil moisture, and precipitation. The machine sends data every hour to the read-down station without interruption. We measure degraded peatlands by SAR interferometry and water table depth monitoring systems for WT in conjunction with this study and the incidence of forest fires in peatlands, then compare the precision of the two methods [44].

This method is also a new approach for the determination of degraded peatland use ALOS-2 PALSAR-2 SAR Interferometry and fields non-stop WT Depth Measuring.

It refers to the use of SAR data to map degraded peatlands to prevent forest fires and forestry management.

1.2. Motivation

- Every year, forest fires appear in Indonesia, particularly in peatlands areas. This phenomenon has inspired me to contribute thoughts and ideas to mitigate the devastating forest fires in Indonesia.
- Moreover, Indonesia's peatlands are large, cover 14 million hectares, and are the largest tropical peatlands, so advanced technology is required to monitor and study them.
- For Indonesia, the Synthetic Aperture Radar application is beneficial with nearly always cloudy tropical conditions. Microwave capability, which can penetrate clouds and record at night, is a benefit in comparison with remote optical sensing technology.

1.3. Objectives

We were exploring the new methods, identifying the fire-risk areas in the peatlands, using synthetic aperture radar data, mainly L-band frequency, to mitigate forest fire disasters.

1.4. Outline

This thesis is presented in 6 chapters, as described below:

- Chapter 1 Introduction
- Chapter 2 Technical Background and Related of Work
- Chapter 3 Proposed Method
- Chapter 4 Result and Discussion
- Chapter 5 Conclusion
- Chapter 6 Summary

Chapter 2. Technical Background and Related Works

2.1. Technical Background of Research

2.1.1. Synthetic Aperture Radar

2.1.1.1. History of Synthetic Aperture Radar

Microwave remote sensing started to be applied in the 1960s and is much newer than the optical remote sensing developed in the 1800s. The benefit of remote microwave sensing is that it is unique and can capture more complex information from the earth's surface than remote optical sensing [45]. In addition, the microwave remote sensing systems can overcome obstacles such as cloud, rain and not rely on sunlight, so that it can also be used for nocturnal acquisition data. One explanation for the use of microwaves is that they can penetrate deeper than optical waves into vegetation.

The sensors of the microwave are divided into two classes: passive (radiometer) and active (radar) sensors. Passive microwave remote sensing can also be divided into two, namely real aperture in the form of a radiometer and a sounder and synthetic aperture consisting of one dimension with two dimensions.

Active microwave remote sensing divided into two, namely real aperture, consisting of scatter meter, altimeter, side-looking airborne radar (SLAR), and meteorological radar, as well as synthetic-aperture, consisting of synthetic radar aperture (SAR) and inverse synthetic aperture radar (ISAR).

In 1903 Radar was first used by Hu¨lsmeyer, who received his design patent in 1904 to track vessels. The first pulsed radar was used in 1925 for remote sensing ionospheric sound experiments. The pulses transmitted by Taylor, Breit and the

Tuve were transmitted by a radio station and observed at a few miles distance in order to measure the ionosphere height. [46].

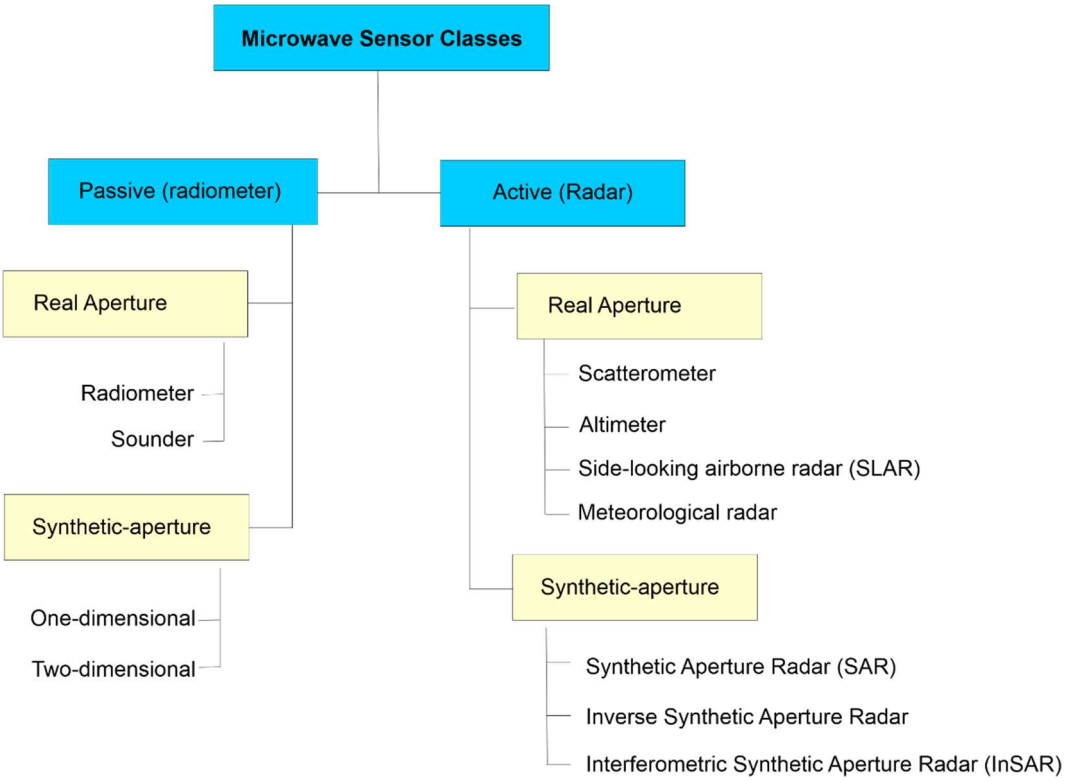

Figure 2. 1. Microwave Sensor Classes [1]

Pulse radars were not developed until the early 1930s to distinguish objects closer to the Earth, and America's first pulsed effective radar was operated in 1936 by the NRL (Naval Research Laboratory). Sir Robert Watson-Watt has developed pulse radars in the UK around 1957. Frequency modulated altimeters with around 400 MHz were the first airborne radars to use extensively in advance of World War II.

In the near future, the MIT Radiation Laboratory (MIT Rad. Lab., 1948-52) and similar labs in the U.S. showed airborne radars at microwave frequencies, which could produce soil images in other countries [45].

A new type of radar, the airborne radar side looking (SLAR), was developed in the 1950s. The SLAR could provide finer resolution images since the antenna was fixed parallel to the plane fuselage for a considerable amount of time. Based on what Wiley called a "doppler beam sharpening system," an airborne radar was developed in 1952. This is the first of the Synthetic Aperture Radar (SAR) [47]

Despite this, the new synthetic aperture radar system is gradually being developed for military and civilian applications. Proposals for Earth observation using spaceborne radar were made in the early 1960s, but the first radar such as this to fly in space was on the SEASAT Oceanographic Satellite, launched in June 1978 by NASA, United States of America (USA). The spaceborne launched after SEASAT mission then shown in Table 2. 1 below

Table 2. 1. Detail history of Space-borne Radar Launched in the world.

Year	**Satellite**	**Band**	**Inc.Angle**	**Polarization**
1978	SEASAT (USA)	L (1.3 GHz)	23°	HH
1981	SIR-A (USA)	L (1.3 GHz)	50°	HH
1984	SIR-B (USA)	L (1.3 GHz)	15°-65°	HH
1991	ERS-1 (Europe)	C (5.3 GHz)	23°	VV
1991	ALMAZ-1 (USSR)	S (3.0 GHz)	30°-60°	HH
1992	JERS-1 (Japan)	L (1.3 GHz)	39°	HH
1994	SIR-C/X-SAR (USA, Germany)	L (1.3 GHz), C (5.3 GHz), X (9.6 GHz)	15°-55°	HH, HV, VV, VH (SIR-C), VV (X-SAR)
1995	ERS-2 (Europe)	C (5.3 GHz)	23°	VV
1995	Radarsat-1 (Canada)	C (5.3 GHz)	20°-50°	HH
2000	SRTM (USA, Germany)	C (5.3 GHz), X (9.6 GHz)	54°	HH, VV (C), VV (X)
2002	ENVISAT (Europe)	C (5.3 GHz)	15°-45°	HH, HV, VV, VH
2006	ALOS-1 (Japan)	L (1.3 GHz)	8°-60°	HH, HV, VV, VH
2007	TerraSAR-X (Germany)	X (9.7 GHz)	15°-60°	HH, HV, VV, VH
2007	Radarsat-2 (Canada)	C (5.3 GHz)	10°-60°	HH, HV, VV, VH

200710	COSMO-SkyMed 1-4 (Italy)	X (9.6 GHz)	20°-59°	HH, HV, VV, VH
2010	TanDEM-X (Germany)	X (9.7 GHz)	15°-60°	HH, HV, VV, VH
2014	ALOS-2 (Japan)	L (1.3 GHz)	8°-70°	HH, HV, VV, VH
2014	Sentinel-1A (Europe)	C (5.4 GHz)	20°-45°	HH/HV, VV/VH
2016	Sentinel-1B (Europe)	C (5.4 GHz)	20°-45°	HH/HV, VV/VH

Source: [2] with modification

Following Table 2. 1 after the launch by the USA of the SEASAT satellite radar, successive satellites launched the SIR-A and SIR-B radar by the US, Europe's ERS-1, USSR's ALMAZ-1 and Japan's single-polarization JESR-1. In 1994, Germany introduced SIR-C / X-SAR with full polarimetric data in cooperation with the USA.

In 1995, Europe and Canada Launched ERS-2 and Radasat-1, both using C-Band frequency and single polarization. In 2000, the international research between USA and Germany launched Shuttle Radar Topography Mission (SRTM) to obtain digital elevation models on a near-global scale.

Then, ENVISAT (Europe), ALOS-1 (Japan), TerraSAR-X (Germany), Radarsat-2 (Canada), COSMO-Skymed 1-4 (Italy), Tandem-X (Germany), ALOS-2 (Japan), Sentinel 1-A, also Sentinel 1-B launched respectively using the various band of L-Band, X-Band, and C-Band).

2.1.1.2. Basic Concept of Synthetic Aperture Radar

Basically, SAR is based on radar antenna movement across a stationary target area. An airborne radar system of synthetic aperture combines the processing of radar and signal into high-resolution backscattering images. Pulses are generated and received in the operation of a SAR when the radar goes through the target area. The received signals are combined for each pulse to produce a high-resolution radar image.

As its name suggests, a synthetic aperture radar is used to ' synthesize ' a long gap for the antenna in the direction of finer resolution. The synthesis happens when the signal is obtained at each antenna location along a linear track, and then the signals are merged as if the antenna were captured at the same time by an array; SAR is actually thought of with time-storage and platform motion to build a long array antenna. Concept of synthetic aperture shown in Figure 2. 2. below:

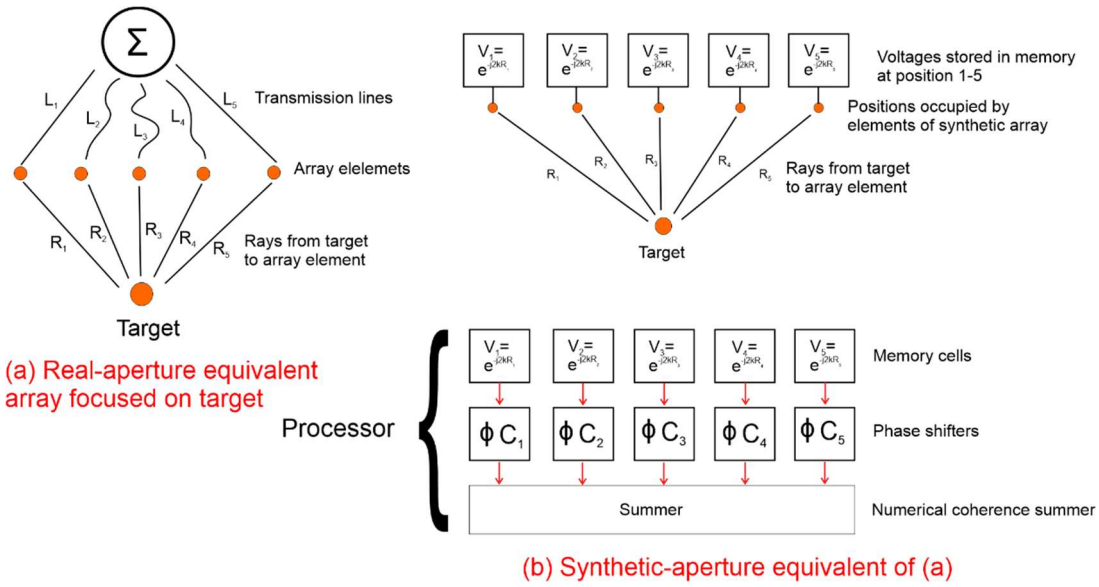

Figure 2. 2. Concept of synthetic aperture [1]

A synthetic aperture radar typically has such a long aperture that the beam must be focused on the point of aiming as much as the camera's lens is concentrated on nearby objects. In comparison with the camera, we might say the "lens" (antenna) is centered on infinity through real-opening systems. For a synthetic opening, the lens or the antenna array is focused on a nearby object.

The average phase delay for the signal coming from the target point should be the same for each element if the input of the individual elements is to be applied in phase; when placed in phase, the array should be centered at the point of destination.

It implies that each item must have the same total distance from the target to the summing point, so that:

$$L1 + R1 = L2 + R2 = L3 + R3 = L4 + R4 = L5 + R5 \qquad (2.\ 1)$$

Lengths Li is the "equal free-space lengths" of transmission lines; i.e., we choose the line length so that the pulse delay in the transmission lines is equivalent to the time of the wave in space. Through propagation, the signals all arrive from the point of reception, so that the phase change along every path is the same as that along every other path. As a result, for the destination T, the overall round trip change for each element is the same, and the electrical fields of the various aspects are all applied during the process.

Received signal for the ith aperture then calculated as:

$$V = \sum_{i=1}^{N} a_i e^{j2kR_i}\ V_i \qquad (2.\ 2)$$

Where Vi is the received signal for the ith opening position, Ri is the distance between the target and the ith aperture position, and Ai is an Optional weighting function to control azimuth sidelobes.

The first synthetic-aperture radar developed by Wiley in the early 1950s was known as the "Doppler" beam-sharpener and was employed in the late 1950s as a "synthetic aperture." And shown in the figure, below:

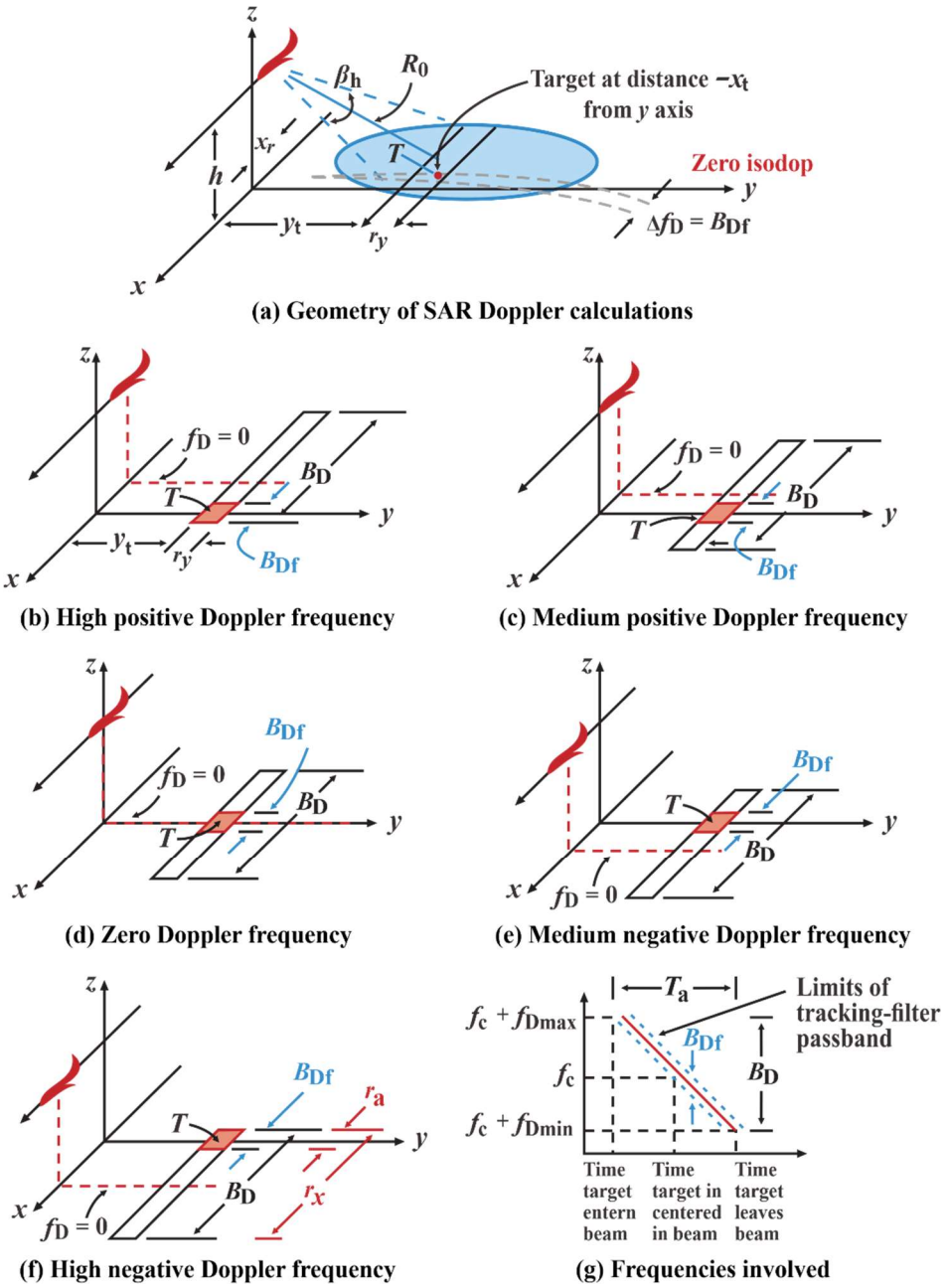

Figure 2. 3. "Doppler" beam-sharpener [1].

In Figure 2. 3. (a) the radar is shown on an aircraft at a distance xr back from the origin of coordinates at a height h; i.e., the aircraft coordinates are (−xr,0,h) and the coordinates of the target T are (−xt,yt,0).

The figure shows the ellipse of the half-power contour of the antenna illumination on the field of the primary aircraft antenna. The ellipse's diameter is distorted for clarity; it is usually a short fan-beam the diameter of the beam in the direction of β h. The efficient field range resolution is shown. The shaded area around the target and bordered by the edges of the beam in the x-direction shows the region, which contributes to the return at a certain point in time. The dotted lines are constant frequency Doppler values (isodopes) around the target. Spacing is the Doppler filter's BDf bandwidth used for beam sharpening.

The Doppler frequency for the target, in this case, is given by

$$f_{dT} = \frac{2u(X_r - 1X_t)}{\lambda R} \qquad (2.\ 3)$$

For the picture in Figure 2.3. (a), the Doppler frequency is positive because both values are negative, and the xr frequency is higher. When xr increases (it becomes less positive initially), the strength of the Doppler reduces. If we ignore a shift in R (the slanting angle from the radar to the target) while the beam is over the target, the decrease in frequency is constant, as shown in Figure 2. 3. (g).

Figure 2. 3. (b)–(f) demonstrate the influence of the beam-sharpening device "oriented" by Doppler, as the target is lit up first on the forward side of the beam and then on the other half of the beam until it finally passes. The geometry of the figure, for example, Fig.2. 3. (a) will be simplified by moving the coordinated approach to position the target on the y-axis at (0, yt,0).

2.1.3. Polarimetric Synthetic Aperture Radar

2.1.3.1. Basic of Polarimetric SAR

In the early 1980s, the field of radar synthetic apertures changed dramatically as advanced radar techniques were introduced, i.e., such as interferometry and polarimetry [49]. Although these two techniques were demonstrated long before,

only the advent of NASA/JPL Airborne Synthetic Aperture Radar (AIRSAR) at the beginning of the 1980s was an operational research tool.

Through SAR polarimetry, electromagnetic waves transmit information from a target to a sensor in the recurrence substance, the polarization of the electromagnetic wave, the data might be encoded. The electromagnetic waves spread directly via free space or indirectly through reflection, dispersion, and radiation to the sensor from the velocity of light from the object. The contact between electromagnetic waves with natural surfaces and atmospheres is highly dependent on wave frequency.

The locus of the tip of E is an ellipse, and the wave is said to be polarized elliptically. Under some conditions, the ellipse can degenerate into a circle or a straight line, whereby the polarization state is called linear and circular polarization [45]

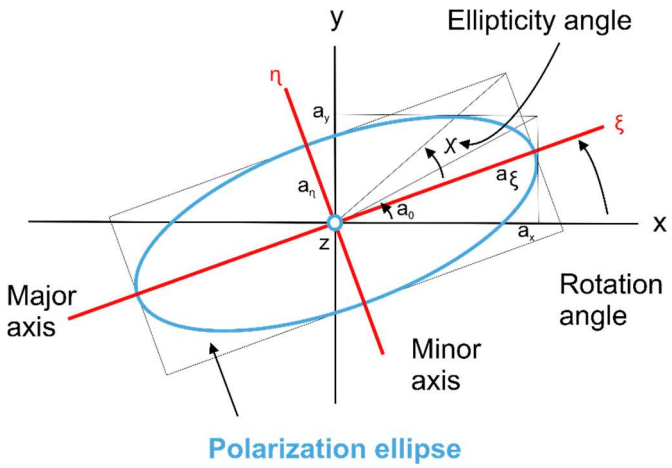

Figure 2. 4. Polarization ellipse in the x-y plane, in the z-direction [1]

Fig. 2.4 shown the ellipse polarization, where Ψ is the rotation angle (angle between the major axis and a reference direction (x-axis), with the range $-\pi/2 \leq \Psi \leq \pi/2$. χ is ellipticity angle and define as:

$$\tan\chi = \pm\frac{a_\eta}{a_\xi} = \pm\frac{1}{R} \qquad (2.4)$$

Where elliptical angle is between $-\pi/4 \leq X \leq \pi/4$, and the plus sign was corresponding to left-handed rotation and the minus sign corresponding to the right-handed rotation. R is the axial ratio from polarization ellipse, and it varies between 1 for circular polarization and unlimited for linear polarization.

Sketches of polarization base on various combinations of rotation angle and ellipticity angle are shown in Fig. 2.5.

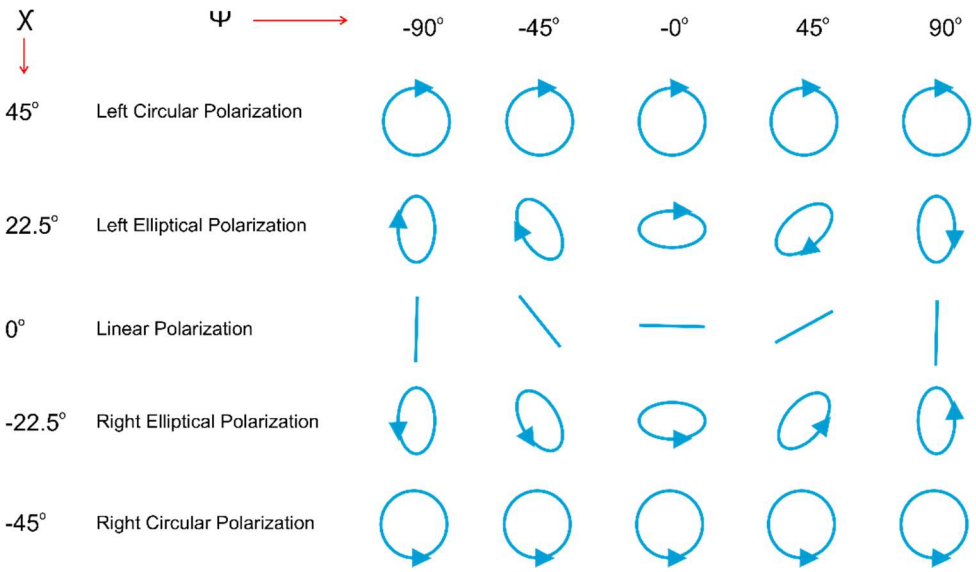

Figure 2. 5. Sketches of polarization base on various combinations of rotation angle and ellipticity angle for a wave direction out of the page [1]

A wave is stated to be linearly polarized if an E(z, t) tip traces a linear segment according to time for a fixed z. Ex(z, t) and Ey(z, t) in the phase (i.e. $\delta = 0$) or out the phase ($\delta = \pi$) exist, express as:

$$E(z,t) = \left(\hat{x}\, a_x + \hat{y}\, a_y\right)\cos(\omega t - kx) \text{ (in-phase)} \quad (2.5)$$

$$E(z,t) = \left(\hat{x}\, a_x - \hat{y}\, a_y\right)\cos(\omega t - kx) \quad (2.6)$$

(out of phase)

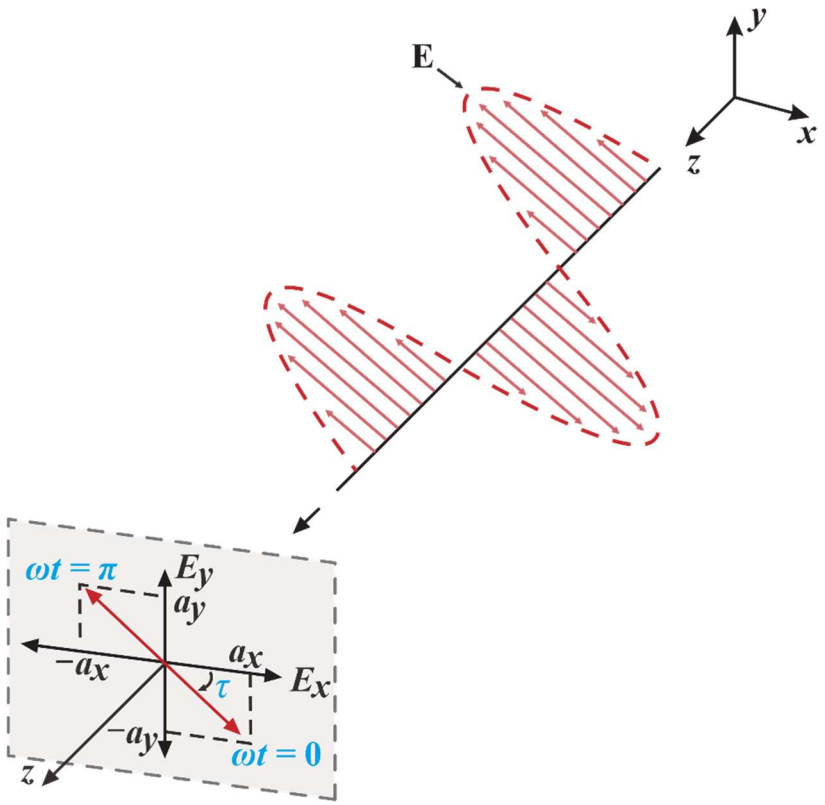

Figure 2. 6. Wave traveling of linear polarization in the +z direction [1]

Polarization will be horizontal if $a_y = 0$ then $\tau = 0^o$ *or* 180^o, and the polarization will be vertical if $a_x = 0$ then $\tau = 90^o$ *or* -90^o

2.1.3.2. Transmission Line Theory and Impedance Model

A transmission line is a structure comprising all or part of a path from one location to another that guides energy transmissions, such as electricity, optical waves and the microwave [50]

As shown, in Fig 2.7, the transmission line comprises parallel conductors that consider resistance R, conductance G, inductance L, and capacitance C, respectively. The transmission line parallel to the z-axis and Δz denotes the length of the segment.

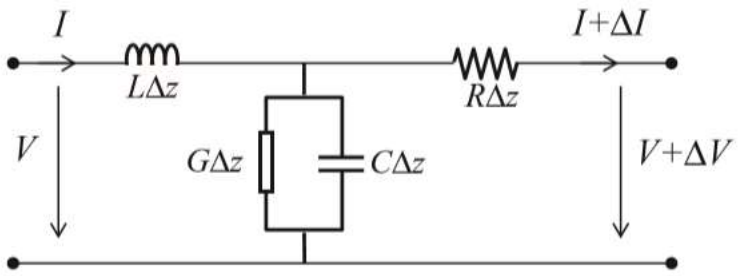

Figure 2. 7. Circuit of transmission line theory segment Δz [3]

Two equation below denotes differential equation that related to current and voltage based on Kirchhoff's law, as follow:

$$\frac{dV}{dz} + (j\omega L + R)I = 0 \tag{2. 7}$$

and

$$\frac{dl}{dz} + (j\omega C + G)V = 0 \tag{2. 8}$$

The second-order differential equation then developed by eliminating current I and voltage V, and express as:

$$\frac{d^2V}{dz^2} - \gamma^2 V = 0 \tag{2. 9}$$

and

$$\frac{d^2I}{dz^2} - \gamma^2 I = 0 \tag{2. 10}$$

Where $\gamma^2 = (j\omega L + R)(j\omega C + G)$, called the propagation constant, and the speed of propagation (phase velocity) is given by:

$$V_p = \frac{\omega}{\beta} = \frac{1}{\sqrt{LC}} \tag{2. 11}$$

β is the phase constant with unit rad/m. Then phase constant can be expressed as:

$$\beta = \frac{2\pi}{\lambda} \tag{2. 12}$$

The phase constant is therefore also known as the wavenumber

In the frequency domain, the current of the transmission line can be obtained from

$$\text{I (z)} = \sqrt{\frac{C}{L}}\,(a_+\, e^{-j\beta z} - a_-\, e^{j\beta z}) \tag{2. 13}$$

And in the time domain expressed as:

$$\mathrm{T}\,(z,t) = \sqrt{\frac{C}{L}}\,[|\,a_+\,|\cos(\omega\,t - \beta z + < a_+ - |a_-|\cos(\omega\,t - \beta z + < a_-]) \tag{2. 14}$$

The power carried by the wave expresses as:

$$\mathrm{P}\,(z,t) = T_+\,(z,t)V_+\,(z,t) = \sqrt{\frac{C}{L}}\,|\,a_+\,|\cos(\omega\,t - \beta z + < a_+) \tag{2. 15}$$

The electric energy store in the unit length expresses as:

$$E\,(z,t) = \frac{1}{2}\,CV_+^2(z,t) = \frac{1}{2}\,C|\,a_+\,|^2\,cos^2(\omega\,t - \beta z + < a_+) \tag{2. 16}$$

Then, the magnetic energy, expresses as:

$$H\,(z,t) = \frac{1}{2}\,CT_+^2(z,t) = \frac{1}{2}\,C|\,a_+\,|^2\,cos^2(\omega\,t - \beta z + < a_+) \tag{2. 17}$$

And the speed of energy propagation (energy velocity) thus given by

$$V_e = \frac{P_+(z,t)}{E(z,t) + H(z,t)} = \frac{1}{\sqrt{LC}} \tag{2. 18}$$

The characteristic impedance of the lossless transmission line is established as

$$Z_0 = \frac{V_+}{I_+} = \sqrt{\frac{L}{C}} \tag{2. 19}$$

The propagation constant of the general lossy transmission line is given by

$$\gamma = \pm\sqrt{(j\omega L + R)(j\omega C + G)} = \pm\alpha \pm j\beta \tag{2. 20}$$

where

$$\alpha = \sqrt{\frac{\omega^2 LC - RG}{2}}\sqrt{\sqrt{1 + \frac{\omega^2(GL + RC)^2}{(\omega^2 LC - RG)^2}} - 1} \tag{2. 21}$$

$$\beta = \sqrt{\frac{\omega^2 LC - RG}{2}}\sqrt{\sqrt{1 + \frac{\omega^2(GL + RC)^2}{(\omega^2 LC - RG)^2}} + 1} \tag{2. 22}$$

The instantaneous voltage is given by:

$$\begin{aligned} \mathrm{V}(\mathrm{z},\mathrm{t}) &= \mathrm{Re}\left[\,\mathrm{V}(\mathrm{z})e^{j\omega t}\right] \\ &= \mathrm{Re}\left[\,a_{+}\,e^{j\,(\omega t-\,\beta z)-\,\alpha z}\right. \\ &\quad +\;\; a_{-}\,e^{j\,(\omega t+\,\beta z)+\,\alpha z} \\ &= |\alpha_{+}|\,e^{-\alpha z}\cos\,(\omega t-\,\beta z+\,\angle\,\alpha_{+})+|\alpha_{-}|e^{\alpha z}\cos(\omega t+ \\ &\quad \beta z+\,\angle\,\alpha_{-}\,) \end{aligned} \tag{2. 23}$$

Where α is called the attenuation constant with a unit of Np/m. The current is given by

$$\mathrm{I}(\mathrm{z}) = \frac{\gamma}{j\omega L+R}\left[\,a_{+}e^{-\,(\alpha+j\beta)z-\,a_{-}e^{-\,(\alpha+j\beta)z}}\,\right] \tag{2. 24}$$

and the characteristic impedance expresses as

$$Z_0 = \frac{V_{+}}{I_{+}} = \frac{j\omega L+R}{\gamma} = \sqrt{\frac{j\omega L+R}{j\omega C+G}} \tag{2. 25}$$

When wave transmitted to the two mediums with different characteristic impedances Z_1 for z < 0 and Z_2 for z > 0, a portion of its power will be reflected, and the remainder will be transmitted and continue to propagate along the +z direction. Coefficient reflection Γ and transmission T then will be expressed as:

$$\Gamma = \frac{Z_2-\,Z_1}{Z_2+\,Z_2},\;\; T = \frac{2\,Z_2}{Z_2+\,Z_1} \tag{2. 26}$$

2.1.4. Interferometric Synthetic Aperture Radar

2.1.4.1. History of Interferometric Synthetic Aperture Radar

Radar interferometry use for Earth-based observations to derive height information about the surfaces of Venus [51] and Moon [52]. The interference fringes modulated by Earth surface topography measurements were recorded on the interferometric radar of an aircraft as well as on satellite platforms, and Graham claimed to calculate the Earth's topography on the aircraft [52]. Nonetheless, though documented trends have demonstrated that, when observed interferometrically, topography produces a predictable phase signal, they have been challenging to analyze, and it has proven unworkable to extract topography data from phase signatures.

The airborne interferometric radar system was implemented by Zebker and Goldstein, at the beginning of the 1980s, on a NASA CV990 aircraft equipped with a digital data recording system. Two radar channels were recorded, one from two separately located radar antennas, and the data were then analyzed using a JPL digital correlator system. They reported that the phase difference between the two signals provides enough evidence to reconstruct the topography of the imaged radar scenes. It was also possible to correct the measured data for ever-present deviations from the flight path of the aircraft that induced radar images to generate artifacts. In addition, the digitally integrated radar interferometric technology can provide information on the digital elevation in the range of several meters, which is much greater than that which was feasible with the radar-stereometric technique in use at the time.

The Goldstein-Zebker team extended the work by the prospect of interferograms using radar antennas traveling along the flight path, which is time separation rather than space separation. With this tool, they were able to determine the heights of ocean waves and tides accurately. The interferogram is used for interferometric analysis for the first time [52]. Subsequently, JPL developed the InSAR platform

for spaceborne, using SEASAT SAR satellite data around the beginning of 1978. At present, the efficient evaluation of centimeter land deformation and its capacity to recreate the continuity of the phase radar, which was known as the unwrapping cycle, is the greatest achievement [53].

Following the launch of the ERS-1 satellite in 1991 by the European Space Agency (ESA), the Interferometric SAR method was quickly jumped using the C-Band bandwidth. The land deformation can subsequently be isolated and identified by Massonnet et al. from the French Center for Space Studies as the findings of InSAR analysis [54]. Following this, a topography radar satellite mission, namely the Shuttle Radar Topography Mission (SRTM) and the TanDEM-X was launched in 2000 [55]

In addition, the interferometric SAR system continued to develop, and after 2000, it was no longer only used with a single interferogram but applied to the interferogram of time series. Various methods, such as stacking [56], persistent scattering [57][58], and small baseline subset analysis [59], have been developed.
Hooper et al. [4] pioneered its applicability to natural terrains, showing that numerous surfaces or vegetation coverings do indeed display dispersion which does not sparkle in phase over months or years. Enhanced algorithms of persistent detection based on methods of maximum likelihood [5] have resulted in the more reliable implementation of those pixels for a longer duration.

2.1.4.2. Concept of Interferometric Synthetic Aperture Radar

InSAR methods are based on the combination of radar returns from two separate antennas, displaced in time or space. The radar scene is diverged between two images because of the parallax of the two measurements, resulting in a distortion of the one image from the other.
The two commonly used radar interferometry receiver configurations are:

1. Two independent radars, each of which has its own transmission / receiving antenna
2. Cross-track with common transmit antenna, but separate receive antennas
3. Track separated by two different radars

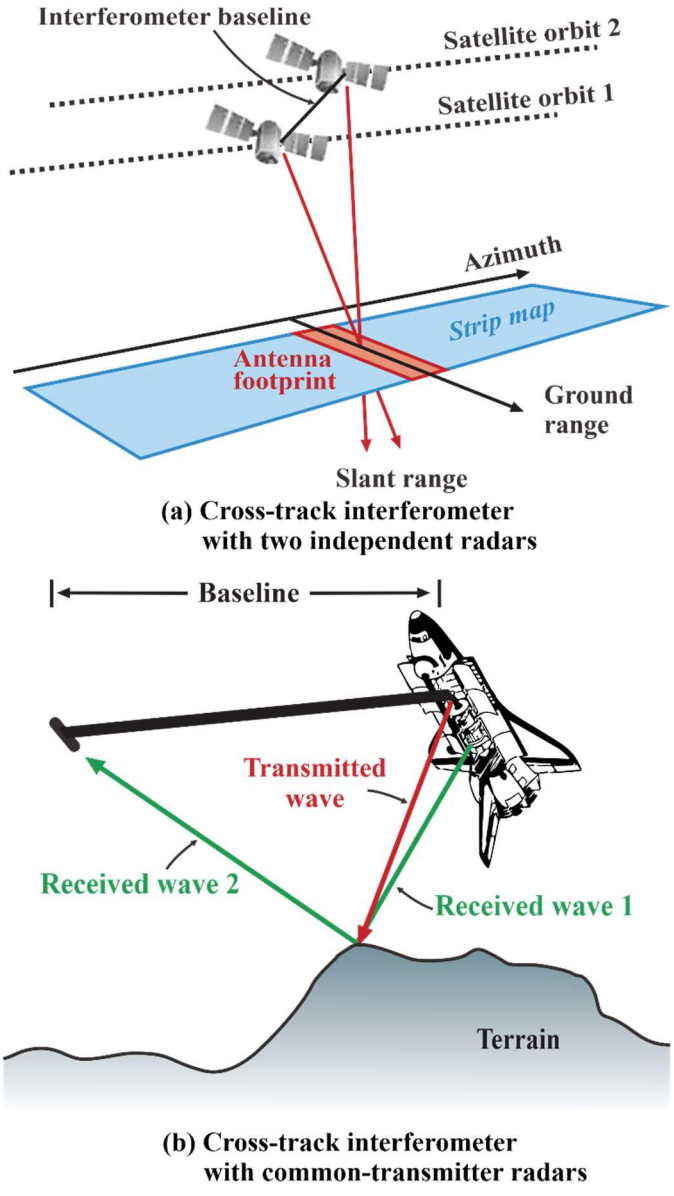

Figure 2. 8. Interferometric cross-track setups in (a) and (b) [1]

The interferometric technique of radar calculation is based on phase data and uses the Parallel Ray approximation, which in Fig. 2.9 needs the classes R1 and R2. The difference is 15-4 but by a tiny amount. There is significant distortion in the statistic of R1 and R2 between the two antennas, the baseline B. We class R2 as R−β and R1 as R for convenience.

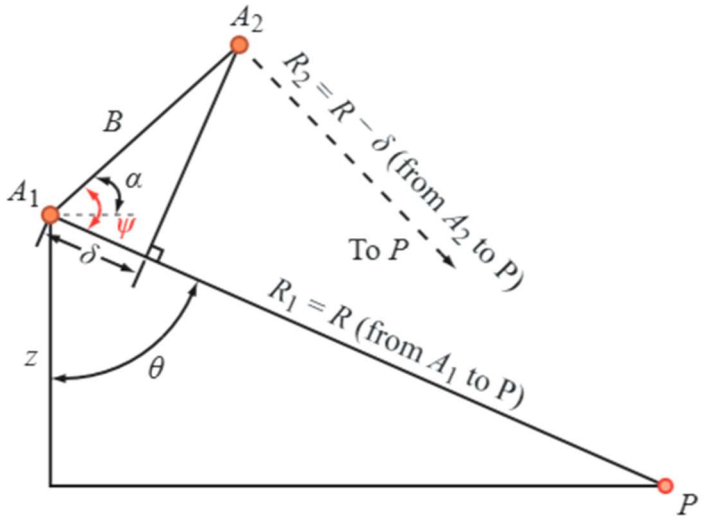

Figure 2. 9. InSAR geometry parallel-ray approximation of R1 = R and R2 = R− β [1]

For the two-independent-radars configuration [Fig. 2.8 (a)], the roundtrip path length between A1 and P is 2R, and for the second radar, it is 2R−2 δ. The corresponding interferometric phase difference (of radar A1 relative to radar A2) is

$$\emptyset_{int} = \emptyset_2 - \emptyset_1 = -2k\delta = -\frac{4\pi\delta}{\lambda} \qquad (2.\ 27)$$

If the same antenna is used, as in Fig. 2.4 (b), the length of the two-way path for the receiving antenna is just 2R−μ, where the difference in phase is

$$\emptyset_{int} = -k\delta = -\frac{2\pi\delta}{\lambda} \quad (2.28)$$

The two expressions for φ int can be combined into:

$$\emptyset_{int} = -k\delta = -\frac{2\pi n\delta}{\lambda} \quad (2.29)$$

where

$$n = \begin{cases} 1 & for\ common-transmit\ antenna \\ 2 & for\ two\ independent\ radars \end{cases} \quad (2.30)$$

In fig. 2.9, its show the horizontal axis orientation of baseline B in the angle α. For A1A2P triangle, the angle is defined by

$$\psi = \frac{\pi}{2} - \theta + \alpha \quad (2.31)$$

and from the cosine law

$$((R-\delta)^2 = R^2 + B^2 - 2RB\cos(\frac{\pi}{2} - \theta + \alpha) \quad (2.32)$$

Since δ "R, however, we can use the parallel-ray approximation to

$$\delta = B\sin(\theta - \alpha) \quad (2.33)$$

Based on Fig. 2.5, then z calculates as:

$$z = R\cos\theta \tag{2. 34}$$

A critical parameter for the design of a topographic mapping system is the estimated height error (precision) associated with the measurement of z, to which we assign the standard deviation symbol Sz. The accuracy Sz is related to the precision with which δ can be measured.

The estimated height error (precision) associated with measuring z, to which we assign a standard deviation symbol S_z, is a critical parameter for the development of the topographical mapping system. The precision S_z, is linked to the precise measurement of δ. The accuracy with δ which can be measured is based on the accurate measurement of the interferometric phase difference $\emptyset_{int}$

$$S_z = \frac{R}{B}\frac{\lambda}{2\pi n} \tag{2. 35}$$

The variance of the phase gap measured $S^2\ \emptyset_{int}$, due to the random phase component of the signal accompanying noise introduced and is approximately proportional to the inverse of the SNR,

$$S^2_{\emptyset_{int}} \approx \frac{1}{SNR} \tag{2. 36}$$

In radar interferometry generation, two antennas offset from each other are used for a radar interferometer. By cross-track interferometry, the two antennas are displaced across the path while they are displaced along the long-track interferometric line. The two antennas are mounted on a single platform in single-pass interferometry, and the data are gathered simultaneously. Data is collected at

different times by multiple platforms or several passes over the data collection area with the same platform for multiple-pass interferometry.

Based on the definitive explanation, it determined that the phase difference between the two antennas ' signals contains information on the topography of the surface. The image of the difference in phase is called the interferogram.

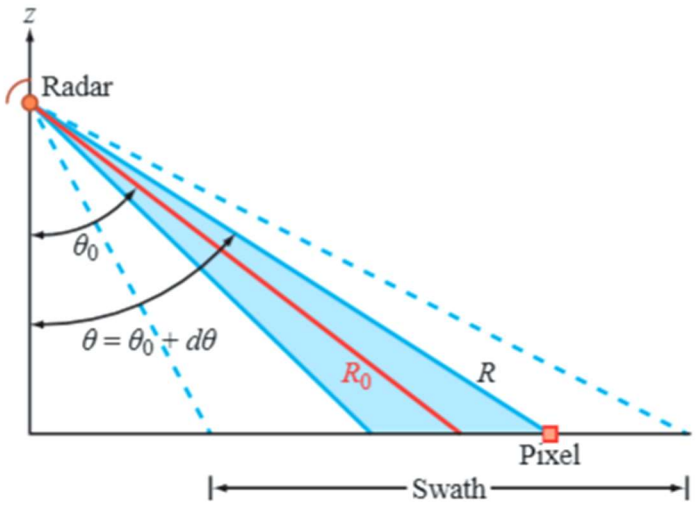

Figure 2. 10. The illuminated swatch is centered in an angle about a middle look angle [1]

In generating and storing an interferogram, the spectrum of a pixel is referred to as the middle of the image region. The incidence angle along the middle of the swath is depicted in Fig 2.10. and the corresponding ranges are R_0. The beamwidth of a SAR satellite is typically a few degrees, e.g., for ERS 1 and 2 from 20^o means that dθ from θ_0 is 3° for the pixel P.

The explanation about displacement versus range is based on Fig. 2.10, dan related to regurgitating with Eq. 10 and Eq. 11. By replacing θ with $\theta_0 + d\theta$ and using the guesstimates sin (d θ) ≈ d θ and cos (d θ) ≈ 1 then

$$z = R\cos(\theta_0 + d\theta) \approx R\,|\cos\theta_0 - \sin\theta_0\, d\theta| \tag{2. 37}$$

and

$$\delta = B\sin(\theta_0 - \alpha + d\theta) \tag{2. 38}$$
$$\delta = B|\sin(\theta_0 - \alpha) + \cos(\theta_0 - \alpha)d\theta$$

Then $d\theta$ express as

$$d\theta = \frac{R\cos\theta_0 - z}{R\sin\theta_0} \tag{2. 39}$$

When Eq. 16 insert to Eq.15 then:

$$\delta = B\sin(\theta_0 - \alpha) + B(\cos\theta_0 - \alpha)\frac{\cos\theta_0 - z/R}{\sin\theta_0} \tag{2. 40}$$
$$\delta = B\sin(\theta_0 - \alpha) + \frac{B\cos\theta_0 - \alpha)}{\tan\theta_0} - \frac{B\cos\theta_0 - \alpha)}{\sin\theta_0}\frac{z}{R}$$

When $R = R_0 + dR$ then

$$\frac{z}{R} = \frac{z}{R_0 + dR} = \frac{z}{R_0}\left[\frac{1}{1 + (dR/R_0}\right] \tag{2. 41}$$
$$\approx \frac{z}{R_0}\left(1 - \frac{dR}{R_0}\right) = \frac{z}{R_0} - \frac{zdR}{R_0^2}$$

Integration from Eq. 2.39 into Eq. 2.40 then:

$$\delta = B\sin(\theta_0 - \alpha) + \frac{B\cos\theta_0 - \alpha)}{\tan\theta_0} \tag{2. 42}$$
$$- \frac{B\cos\theta_0 - \alpha)}{\sin\theta_0}\left(\frac{z}{R_0} - \frac{z}{R_0^2}\,dR\right)$$

Based on consideration of estimation that z ≈ $R_0 \cos\theta_0$ Eq. 19 then can simplify to:

$$\delta = B\sin(\theta_0 - \alpha) + \frac{B\cos\theta_0 - \alpha)}{\tan\theta_0}\frac{dR}{R_0} \quad (2.43)$$

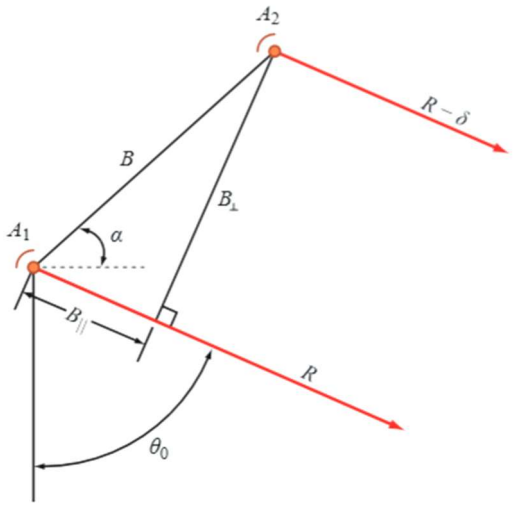

Figure 2. 11. Component of baseline (parallel and perpendicular) [1]

Based on Figure 2.11. we understood that baseline has two components, namely a parallel and perpendicular component. The total of offset between the images then can be express as a function of the two InSAR baseline component as:

$$\delta = B \parallel + B \perp \frac{dR}{R_0 \tan\theta_0} \quad (2.44)$$

where

$$B \parallel = B\sin(\theta_0 - \alpha), and \quad (2.45)$$
$$B \perp = B\cos(\theta_0 - \alpha)$$

The phase difference, when forming an interferogram, refers to the phase in a pixel in image 1 to the phase of a different pixel location of the same target at picture 2. A formatting relation between each pixel in image 2 and its respective location in image 1 must then be established.

The interferogram is done in practice by calculating the change in image 2 in conjunction with image 1. Its also done through the detection of the related points between two images, and as the solution to an offset equation. This is called the interferometric offset field or image co-registration.

There are many ways to determine compensation, but just one recipe is considered for brevity. In general, we adopt a 2-D approach to solve the shift estimating problem because both range and azimuth can change in the case.

Offsets can be found by selecting a small area in image 1, and cross-cutting them across a similar area in image 2 for the best matching terrain. The direction of the correlation highest at that point gives the offset

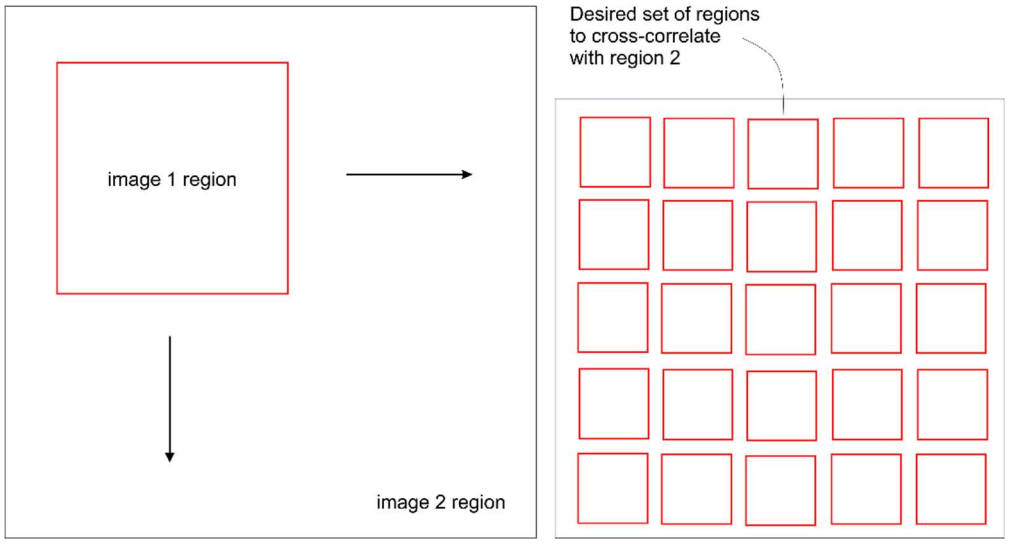

Figure 2. 12. Cross-correlation between image 1 and image 2 [1]

Cross-correlation function Kc (1, k) then computed using:

$$Kc\ (1,k) = \frac{\Sigma_i\ \Sigma_k C_1(m,n) C_2^*\ (m_2+i, n_2+k)}{\sqrt{\overline{C_1}\,\overline{C_2}}} \qquad (2.\ 46)$$

$$\text{with: } \overline{C_1} = \ \Sigma\Sigma\ \ C_1(m,n)\ C_1^*(m,n)$$

$$\overline{C_2} = \ \Sigma\Sigma\ C_2(m_2+i, n_2+k)\ C_2^*(m_2+i, n_2+k)$$

Someplace quantities over a region of C_1 size are measured. In practice, this calculation uses a two-dimensional signal processing window. As the initial offset is not known, C_2 is usually chosen to be larger than C_1, as shown in Fig. 2.8.

Since the images are complex, the complicated correlation described in Eq 2.47 lists the required shift directly. The complex correlation in low scattering areas can, however, lead to inaccurate estimates if the noise of the pixel phase is large (for example, because of low SNR) and the image power correlation (pixel magnitude) is useful instead of complex pixel values.

After the interferogram has been calculated, it is generally desirable to view multiple data, so that the phase estimate is more exact, at the cost of spatial resolution. Multi looking means that in one or two dimensions, the pixel intensity is averaged to reduce fluctuations. More multiple data than single-look images are much smoother and can be sampled without losing much information. Multi looking also minimizes the calculation and storage volume required.

2.1.4.3. Correlation (Coherence)

The degree of correlation between the two images (coherence) is an essential measure of the interference quality, or of how close the phase in one image is the other. This amount varies between 0 for fully independent images to 1. The correlation of images can be calculated based on the equation:

$$\rho = \frac{\sum image\ 1_i\ image\ 2_i^*}{\sqrt{\sum image\ 1_i\ image\ 1_i^*}\sqrt{\sum image\ 2_i\ image\ 2_i^*}} \qquad (2.\ 47)$$

Where the complex values of a point corresponding to image 1 and image 2 are images 1i and 2i after the estimated shift is resampled from image 2.

The degree of correlation is generally based on the SNR and local target characteristics

2.1.4.4. Decorrelation

a. Geometric Decorrelation

When measured phases and amplitudes coincide, radar echoes are assumed to be "correlated" with each other and thus show the "same" interaction between radar signal and spreading terrain. In an imaging radar, this means that the dispersive properties or patterns detected are almost similar.

Speckle is a natural result of the radar's cohesive nature. It can be seen as "grainy" appear in radar images of one-look.

As V is the consistent number of the signal transmitted from the different dispersers within the resolution cell, a change in direction causes changes in the ranges of each disperser; hence, a change of magnitude and phase V. This contributes to geometric decorrelation. The degree of decorrelation depends on the amount of angular compensation between the two antennas.

b. Temporal Decorrelation

When the acquisition of the two images did at different times, we consider the correlation of them. Although the backscattering phase is a random amount, as it is a sum of n-dispersion echoes from R_1 to Rn if the scene area is unchanged between the observation time and the radar is at the same location. The R_1 to Rn will remain unchanged, with total echoes fully correlated. But if some of the scattered moves slightly, the echoes differ somewhat. This condition is referred to as temporal decorrelation.

Temporal Decorrelation expressed as:

$$\rho_{temporal} = \left[-\frac{1}{2}\left(\frac{4\pi}{\lambda}\right)^2 (S_y^2 \sin^2\theta + S_z^2 \cos^2\theta\right] \qquad (2.48)$$

c. Spatial Decorrelation

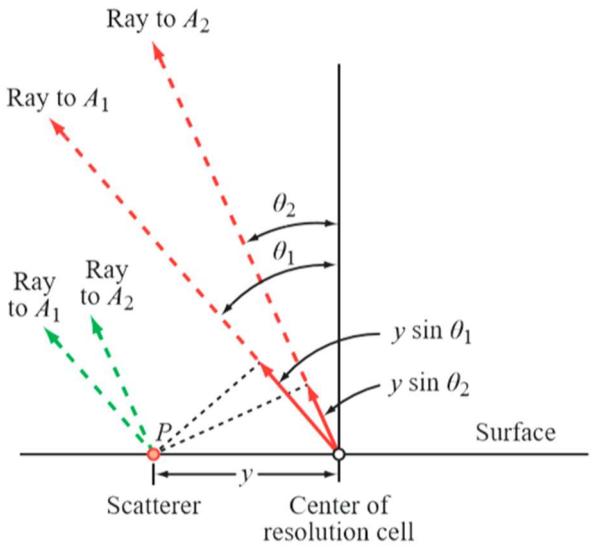

Figure 2. 13. Decorrelation model imaging geometry [1]

Based on Fig. 2.13, consider the reflecting phase of the scattered at P, in contrast with the reflection phase of the resolution center cell. By the parallel rays' approximation, the P to A1 phase is advanced using y sin θ_2 relative to the O to A1 ray and the equivalent y sin to 2 phase advance applies to an A2 antenna. If there are a lot of dispersing elements in the cell, the total signal V_1 at antenna 1 can be modeled as an integral part of the signal reflected by all scatters in the resolution portion.

$$V_1 = \iint S\,(x - x_{0,}\; y - \; y_0\;)\; exp\;\left[-j\;\frac{4\pi}{\lambda}\;(R\;+\;y\sin\theta_1\right].\,p(x,y)\;dx\;dy \tag{2. 49}$$

Where S (x, y) represents the complex scattering amplitude of (x, y) on the surface, and p (x, y) is a function of space coordinate radar system pulse response. The sum of all the contributions from the points weighted by the impulse response in the resolution cell.

V2 of antenna 2 then calculate as:

$$V_2 = \iint S\,(x - x_{0,}\; y - \; y_0\;)\; exp\;\left[-j\;\frac{4\pi}{\lambda}\;(R\;+\;y\sin\theta_2\right].\,p(x,y)\;dx\;dy \tag{2. 50}$$

Spatial correlation compute by equation

$$\rho_{\text{spatial}} = \frac{\langle V_1 V_2^* \rangle}{\sqrt{\langle V_1 V_1^* \rangle \langle V_2 V_2^* \rangle}} \tag{2. 51}$$

Based on Fig 2.13. then can express as:

$$\rho_{\text{spatial}} = 1 - \frac{2B_{\perp} r_y \cos\theta}{\lambda R} \quad (2.52)$$

d. Rotational Decorrelation

When the radar flight track of a pass is rotated relative to the track of the second pass (i.e., not parallel), the second source of decorrelation is added due to the geometry of the image.

The rotating correlation is expressed as

$$\rho_{\text{rotation}} = 1 - \frac{2\, r_x d\phi \sin\theta}{\lambda} \quad (2.53)$$

Where r_x is the resolution of azimuth and $d\phi$ is the angular difference between both tracks

2.1.4.5. Unwrapping

We have developed a set of equations in the above sections which relate the phase difference $\ddot{\phi}_{int}$ (measured by interferometric SAR) of a pixel to the height z of that pixel. Therefore, it should be possible to create a topographical map of the image scene, given the image geometry and the absolute values of ϕ_{int} for each pixel.

Phase, however, is only measured modulo 2π, which means that the phase must first be unwrapped before applying it to determine z. The measured phase modulo 2 π is

known as the wrapped phase. The process of converting the wrapped phase into the absolute phase is called phase unwrapping. It entails determining how many multiples of 2 π should be added to the wrapped phase to produce a continuous phase surface.

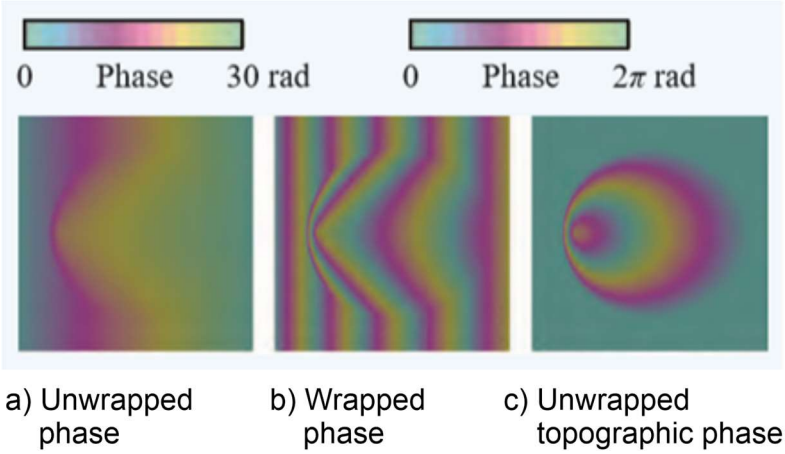

Figure 2. 14. Comparison between the unwrapped phase wrapped phase and unwrapped topographic phase of the interferogram [1]

The (absolute) phase difference is for an InSAR with two different radars and expresses as

$$\phi_{int} = -\frac{4\pi}{\lambda}\,\delta = -\frac{4\pi B}{\lambda R}\left[\sqrt{R^2} - z^2\cos\alpha - z\sin\alpha\right] \qquad (2.\ 54)$$

An additional step of the unwrapping process includes segregating from the flat Earth reference the two components of φ_{int}, the component topographical (height) variations, of the component φ. The phase pattern that Interferometric SAR measures if $z = z_0$ is constant everywhere in the image.

We specified z0 as the mean surface height to distinguish the two-phase components and dz as the deviation from z0 due to the topographical height. Z then replacing by z0 + dz, and the equation then expressed as:

$$\phi_{int} = -\frac{4\pi B}{\lambda R}\left[\sqrt{R^2} - (z_0 + d_z)^2 \cos\alpha - (z_0 + d_z)\sin\alpha\right]$$
$$= -\frac{4\pi B}{\lambda R}\left[\sqrt{R^2} - (z_0^2 + 2\,z_0 d_z + dz^2 \cos\alpha - (z_0 + d_z)\sin\alpha\right] \quad (2.55)$$

By neglecting dz^2, factoring $\sqrt{R^2} - z_0^2$, and using Taylor series expansion, the equation and then can express as:

$$\phi_{int} = -\frac{4\pi B}{\lambda R}\left[\sqrt{R^2 - z_0^2\left(1 - \frac{z_0 d_z}{R_0^2 - z_0^2}\right)}\cos\alpha - z_0\sin\alpha - d_z\sin\alpha\right] \quad (2.56)$$

Flat-Earth component calculated by setting dz = 0:

$$\phi_{fe} = -\frac{4\pi B}{\lambda R}\left[\sqrt{R^2} - z^2\cos\alpha - z\sin\alpha\right] \quad (2.57)$$

And the topographic component is given based on the equation:

$$\phi_{topo} = \phi_{int} - \phi_{fe}$$
$$= \frac{4\pi B}{\lambda R}\left[\frac{z_0 \cos\alpha}{\sqrt{R^2 - z_0^2}} + \sin\alpha\right] dz \quad (2.\ 58)$$
$$= \frac{4\pi B}{\lambda R}\left[\frac{\cos\alpha}{\tan\theta} + \sin\alpha\right] dz$$

And then ambiguity height calculates by

$$\Delta_z = -\frac{\lambda R}{2B\left(\frac{\cos\alpha}{\tan\theta_0} + \sin\alpha\right.} \quad (2.\ 59)$$

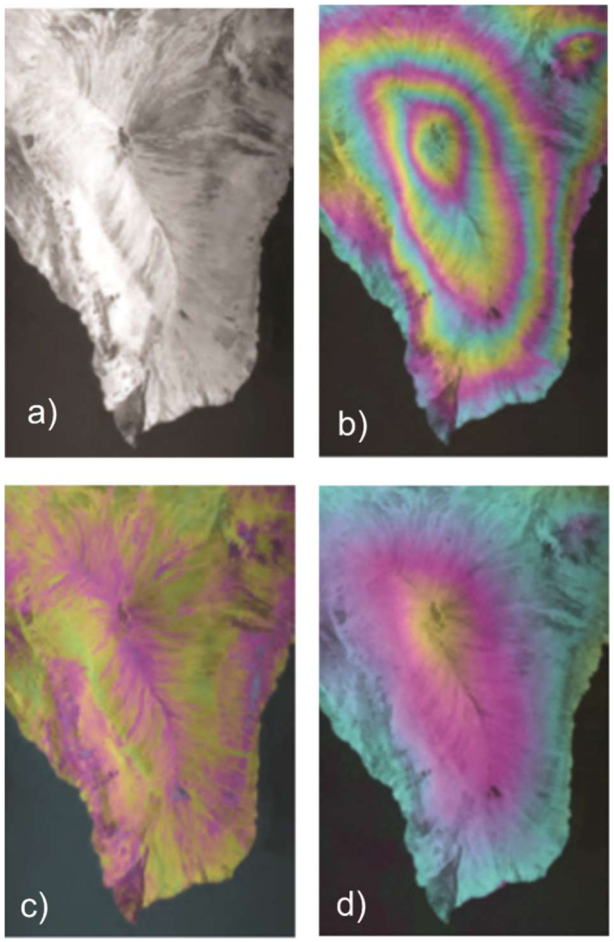

Figure 2. 15. Sample Image of Interferogram Processing (a) SAR Image, (b) Interferogram, (c) correlation between interferogram component (d) topography image [1]

2.2. Related Works

Some research using remote sensing optical data has been widely used in mapping forest fires, especially using MODIS data to detect several large scales of fuel connectivity patterns. It can be used to monitor fire hazard patterns using graph theory [10]. NOAA-AVHRR is also used to detect soil moisture related to forest fire [11]. Problems with optical satellite data are that information about the soil surface is not available in a cloudy condition and at night. The Fire Weather Index (FWI) calculated by The Canadian Forest Fire Danger Rating System (FDRS), based on weather information: temperature, relative moisture, wind speed, and rain, was installed in Indonesia starting in 2004 [9s]. The study using RADARSAT-1 C-Band data [7] has shown that the backscattering coefficient and FWI has strongly correlated. Other research studies have evaluated the ERS sensor for fire hazard prediction in a boreal area where there is also a significant correlation among burn backscatter, forest backscatter, and FWI [8]. The study [9] shows a method for monitoring spatial and temporal surface moisture of soil in the fire that disturbed the boreal forest and also [10] for monitoring live fuel moisture in semi-arid areas. Soil moisture recovery developed using SAR data, which is important for monitoring peat fire risk [11].

ALOS PALSAR data is also worked to detect burn-coal seam thickness [12] of fire scars [13], topsoil thickness [14], and layer thickness estimates for silica sand distribution [15]. The impedance model considered the relationship between dielectric constants, incident angles, and backscattering coefficients.

Other studies employed subsidence information to indicate degraded peatlands and to retrieve the groundwater table and others in the area of peatlands [16][17][18][19].

Using JERS-1 SAR L-Band Frequency, transmission line theory was employed to detected burn-coal seam thickness [12]. This method employed to calculate the

backscattering coefficient and also burn-coal seam thickness. Based on the study, burn-coal thickness classified as 4 class, namely: burnt coal seam 1, burnt coal seam 2, burnt coal seam 3, and burn coal seam 4, with backscattering coefficient -7, - 6.5, -5.8, -5 in dB, and thickness 0.52, 0.48, 0.37, and 0.33 in meter unit. In this study, soil roughness not yet considers in the calculation.

Based on [13], transmission line theory is also used to estimate the thickness of fire scars. Based on the result, fire scars thickness in the area study is 0.52 meters. The model based on three layers consists of free space, burnt coal seam, and peatland.

The transmission line theory is also employed to estimate topsoil thickness in arid and semi-arid areas by using JERS-1 data L-Band frequency [14]. Based on the study, a multilayer of soil is simulated by the assumption that under the soil area consists of limestones layer. The soil consists of three class names: Hardpan topsoil, Qaa topsoil, and Topsoil of herbaceous area. The average backscattering coefficient, respectively, is -34, -34.5, and -32.8 dB. Estimation of thickness is 73,84, and 54 with the ground data thickness 50-120, 70-100, and 40-80 cm.

Other research in Riau employed the transmission line theory model to estimate the thickness of Silica [15]. Using ALOS PALSAR data, this research successfully estimated the thickness of Silica in Rupat Island, Riau Province. The backscattering of Silica found -51 until -59 dB with the thickness of Silica between 59 – 74 cm. This research, however, did not use soil roughness information because the surface of the sand was almost flat.

Other research employed Interferometric SAR to monitor peatland in the United Kingdom and Central Kalimantan [16] [17]. The study used C-Band data and L-Band data and detected a subsidence rate of around 0.3 cm/year, and 2 cm decreased between 2002 – 2010. In this research found that L-Band data provides high coherence data compare to C-Band data. The study also successfully to estimate

CO^2 emission and monitor the effectivity of peatland restoration based on spatial and temporal changes of peat hight.

Monitoring the dynamic subsidence done in the tropical peatland area [19]. This study aims to learn the relationship between subsidence of peatland and groundwater level. Based on this study, the increase in subsidence rate was 0.9 cm per year for each 10 cm lowering of the groundwater level.

2.3. State of The Arts

Several experiments using optical remote sensing data widely used to identify peat fire risk area, among others, are to detect several large scales of fuel connectivity patterns by using MODIS data, and soil moisture by using NOAA-AVHRR data.

Another research identified the peat fire risk area in peatland using SAR data based on soil moisture retrieval method. This research employed SAR data to identify the peat fire risk area based on groundwater table conditions by using polarimetric and SAR Interferometry approaches.

Chapter 3. Proposed Method

3.1. SAR Polarimetry Method

In this analysis, an impedance-based approach was used using the principle of line theory. Impedance models are built based on the idea of the theory of transmission line through which surface roughness layer, peatland layer, and the layer of soil are impeded. The scattering mechanism is displayed in Fig. 3.2., while the model circuit is shown in Fig. 3.1. The model has 4 layers based on the scattering mechanism of the air layer, surface roughness layer, peatland layer, and soil layer.

According to this model, the media consist of a constant amount of air layer, surface roughness layer, peatland layer, and soil thickness layer. The three-dimensional model is expressed based on impedance based.

According to the model of the circuit, Z_R denotes an essential impedance of sequence layer roughness for the soil, Z_P and Z_S denote the parallel model of the peatland layer. Due to the limitations of the penetration of electromagnetic waves in deep land, the involvedness of the study was condensed by the negligible the soil layer (Z_S) of parallel impedance. The parallel impedance of the soil layer then nulls considered.

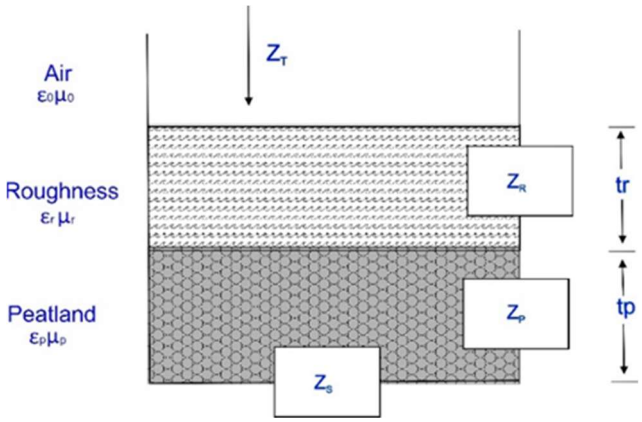

Figure 3. 1. The basic model of the research [20]

Thus, an incident wave is often known to be a wave plane by an incident angle [21] formerly the total contribution of the impedance model for surface roughness is resolute by

$$Z_{T1} = Z_R \frac{Z_P + Z_R \tanh \gamma c^t}{Z_R + Z_P \tanh \gamma c^t} \tag{3.1}$$

The above model is parallel with the complete peatland layer's input impedance function well-defined by:

$$Z_{T2} = Z_P \frac{Z_S + Z_P \tanh \gamma c^t}{Z_P + Z_S \tanh \gamma c^t} \tag{3.2}$$

Depending on the above theorem, γC is the propagation persistent of the surface roughness and also peatland layer. Thus, by employed Snell law at the boundary between air layer, surface roughness layer, and peatland layer and is expressed as follows

$$\sin \theta_i = \sqrt{\varepsilon_r \mu_1} \sin \theta_1 \tag{3.3}$$

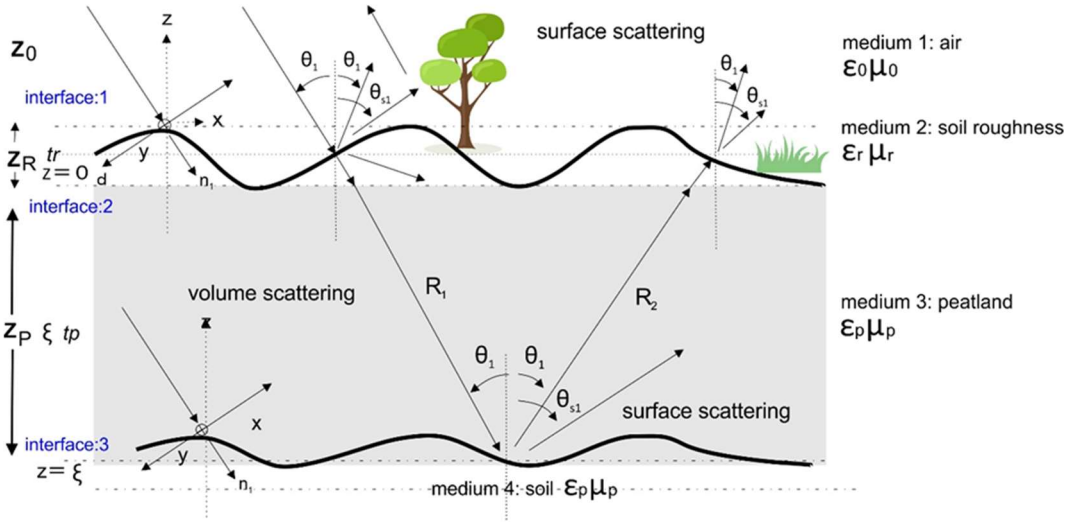

Figure 3. 2. Mechanism of scattering between layers [20]

Where θi is transmission angle, εr, μr, are multipart dielectric constant, and precise multipart permeability of surface roughness layer and peatland layer. Thus, the constant of propagation is then accomplished as,

$$\gamma_c = j\frac{2\pi}{\lambda}\sqrt{\varepsilon_r\mu_r - \sin^2\theta i} \tag{3.4}$$

The effectiveness of the impedance surface layer series (Z_R), then calculated based on the equation:

$$Z_R = Z_0\sqrt{\frac{\varepsilon_r}{\mu_r}\cos\theta_i}\ and\ Z_P = Z_R\sqrt{\frac{\varepsilon_r}{\mu_r}\cos\theta_i} \tag{3.5}$$

The impedance of the peatland layer was thus stated as

$$Z_P = Z_R\sqrt{\frac{\varepsilon_r}{\mu_r}\cos\theta_i} \tag{3.6}$$

The balance for the effective impedance of the sequence of the surface roughness layer may be shown as,

$$Z_{T1} = \frac{Z_0}{\varepsilon_r}\sqrt{\varepsilon_r\mu_r - \sin^2\theta_i}\ x \times \tanh\left(j\frac{2\pi t}{\lambda}\sqrt{\varepsilon_r\mu_r - \sin^2\theta_i}\right) \tag{3.7}$$

Parallel to a peatland layer impedance that can be defined as:

$$Z_{T2} = \frac{Z_R}{\varepsilon_r}\sqrt{\varepsilon_r\mu_r - \sin^2\theta_i} \times \tanh\left(j\frac{2\pi t}{\lambda}\sqrt{\varepsilon_r\mu_r - \sin^2\theta_i}\right) \tag{3.8}$$

Then the Z_T function is determined with the parallel circuit

$$\frac{1}{Z_T} = \frac{1}{Z_{T1}} + \frac{1}{Z_{T2}} \tag{3.9}$$

By considering the equation above, the coefficient reflection is formerly determined through:

$$\Gamma = \frac{Z_T - Z_0 \cos \theta_i}{Z_T + Z_0 \cos \theta_i} \tag{3.10}$$

Coefficient of backscattering dependent on the model of the impedance and thus attained as:

$$\sigma^0_{cal} = 20 \log|\Gamma| \tag{3.11}$$

The above model has a non-linear function of the dynamic dielectric constant and depth of the backscattered surface roughness layer and peatland layer. The surface roughness depth is measured in the field by a surface roughness ruler equipment designed by JMRSL. In this study, the thickness of the peatland layer for L-band frequency considered equal to lambda to make the model simpler.

3.2. SAR Interferometry Method

This study used the Interferogram based approach DInSAR which developed radar imaging active mode coherence technology. In 1974, Graham first conducted DInSAR experience. DInSAR has recently established and stayed actual helpful in defining the singularity of subsidence and land movement in the world, including continuity and subsidence of DInSAR in peatlands [22]

SAR interferometry analysis by the use of a phase as a wave element and transformation to distance, two images acquired by the same nominal geometry are needed. The exact range of the submillimeter can be generated because microwave signals have a centimeter wavelength. The first image is employed as a reference, and the second image is used as a slave to resample the equivalent grade from the master shot. In azimuth call lines, the pixel coordinates in the call sample range and pixel coordinates so that an image is named Img (s, l). and thus, the phase rate ø [22] corresponding.

The phase rate can then stated according to its Ri distance from the sensor.

$$\emptyset = \frac{4\pi}{\lambda} Ri \tag{3.12}$$

Where ø is a phase, lambda is the wavelength, L-band wavelength is 23.5 cm in this case.

The interferogram among I and k of images could be denoted as

$$Int_{ik}(s,l) = Img_i(s,l).Img_k^*(s,l) \tag{3.13}$$

The process of interferometric among images I and k can be stated as to once the result is pixel through the pixel. Thus, the star sign shows the complication of the conjugate as

$$\emptyset_{ik}(s,l) = \emptyset_i(s,l).\emptyset_k(s,l) \tag{3.14}$$

The equation can be expressed as a combination of two equations before:

$$\emptyset_{ik}(s,l) = \frac{4\pi}{\lambda}[R_i(s,l) - R_k(s,l)] \tag{3.15}$$

The normal baseline is the relative position of the master and slave image laterally towards the normal reference angle, with a relation with incidence Δθ angle as

$$\Delta\theta = \frac{Bn}{R_k} \tag{3.16}$$

where the primary reference point O is Rk= SkO, and the interferometric relative is therefore

$$\Delta\phi_{ik} = \phi_{ik}(P) - \phi_{ik}(O) = \frac{4\pi}{\lambda}[R_{ik}(P) - R_{ik}(O)] \tag{3.17}$$

The relative interferometric process is expressible as

$$\Delta\phi_{\text{ik}} = \Delta\phi_{ik}^{flat} + \Delta\phi_{ik}^{height} \tag{3.18}$$

Where flat and topographical (high) step words are respectively

$$\Delta\phi_{ik}^{flat} = \frac{4\pi}{\lambda}\frac{Bn}{R_k}\frac{\Delta r}{\tan\theta} \; and \; \Delta\phi_{ik}^{height} = \frac{4\pi}{\lambda}\frac{Bn}{R_k}\frac{\Delta h}{\sin\theta} \tag{3.19}$$

The flat terrain step is then eliminated since it is not suitable for any sort of use; this step named interferogram flattening. The height of ambiguity is Δ, ha, the height that creates a spin is equivalent to 2π. The height of uncertainty is thus computed through:

$$\Delta h_a = \frac{\lambda R_k sin\,\theta}{2B_n} \tag{3.20}$$

The following step is to eliminate the topographical phase, and the next step is to produce the differential interferometric phase on the basis on equations

$$\Delta\phi_{ik}^{DInSAR} = \Delta\phi_{ik} - \Delta\phi_{ik}^{flat} - \Delta\phi_{ik}^{height} \quad (3.21)$$

After that, Goldstein 5x 5 is used, and ambiguities in the process are solved with unwrapping.

$$\Delta\phi_{\mathrm{ik}}^{UW}(s,l) = \phi_{ik}(s,l) \pm 2n\pi \quad (3.22)$$

The groundwater table (GWT) is then estimated using the Woosten Model [29]:

$$S = 0.04\ x\ WT \quad (3.23)$$

Where S is the yearly subsidy rate (cm/year). WT is the depth of the tropical peatland's groundwater table (cm), sometimes called GWT (Ground Water Table).

3.3. Backscattering Coefficient of Satelite Data.

The backscattering coefficient is determined for ALOS-2 PALSAR-2 Level 1.1 data by JAXA based on the calibration process. (Complex Single Look)

$$\sigma^{o} = 10 * \log_{10} < DN^{2} > -CF + A \quad (3.24)$$

Where σ^{o} is the backscatter coefficient and the digital number is DN, CF is the level 1.5 correction factor, and level 2.1 is the level 1.3 of ALOS-2 (-83 dB), and level 1.1 is the level 1.1 correction factor. Data ALOS-2= 32 dB [23].

3.4. Flowchart of Research

3.4.1. Research 1 (Location: Siak Regency, Sumatera, Indonesia)

The flow diagram of the research 1 shown in Figure below,

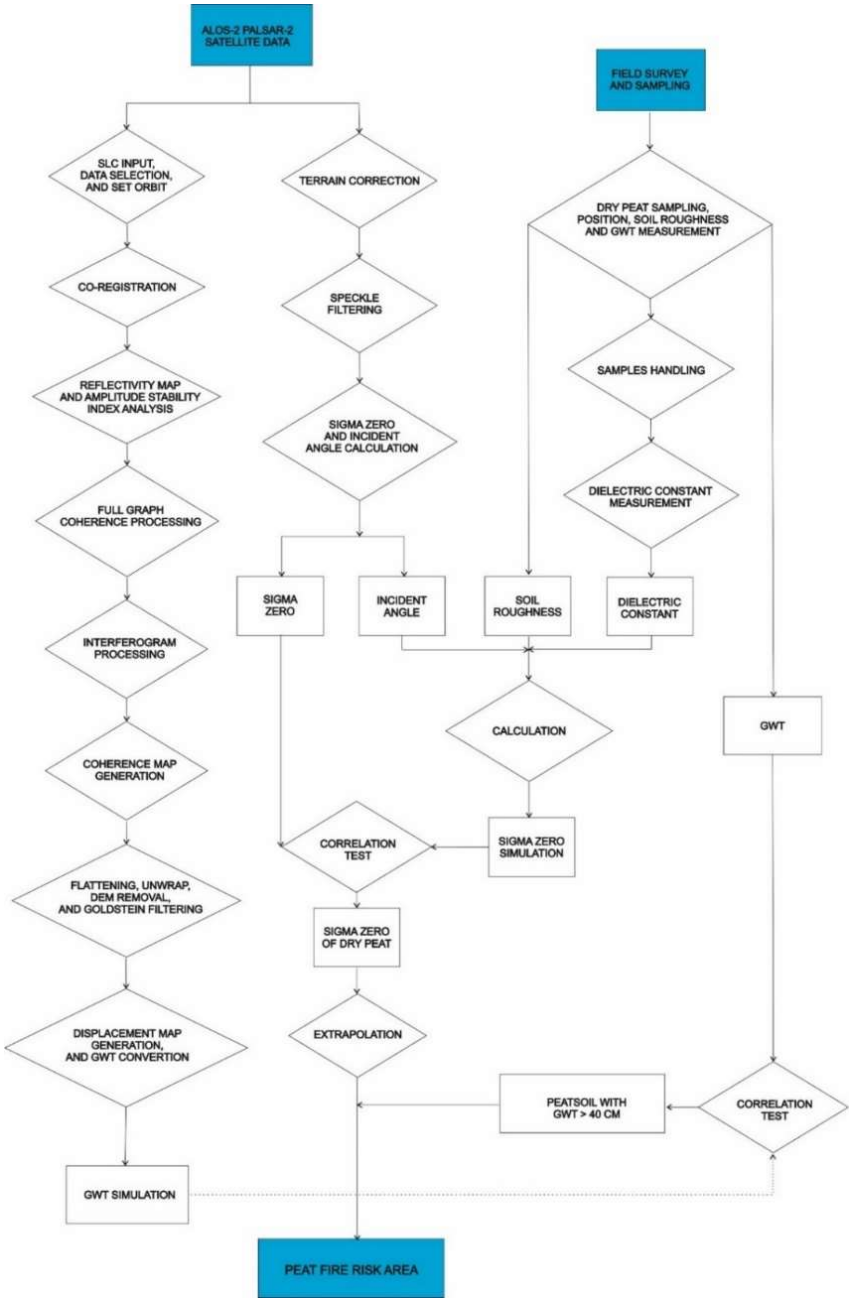

Figure 3. 3. Flowchart of the Research 1 [20]

3.4.2. Research 2 (Location: Pulang Pisau, Central Kalimantan, Indonesia)

I Research 2, DInSAR combined with Ground Water Depth Stations in Kalimantan Indonesia to detect peatland degradation area relate to forest fire, with the flowchart of research shown in Figure below.

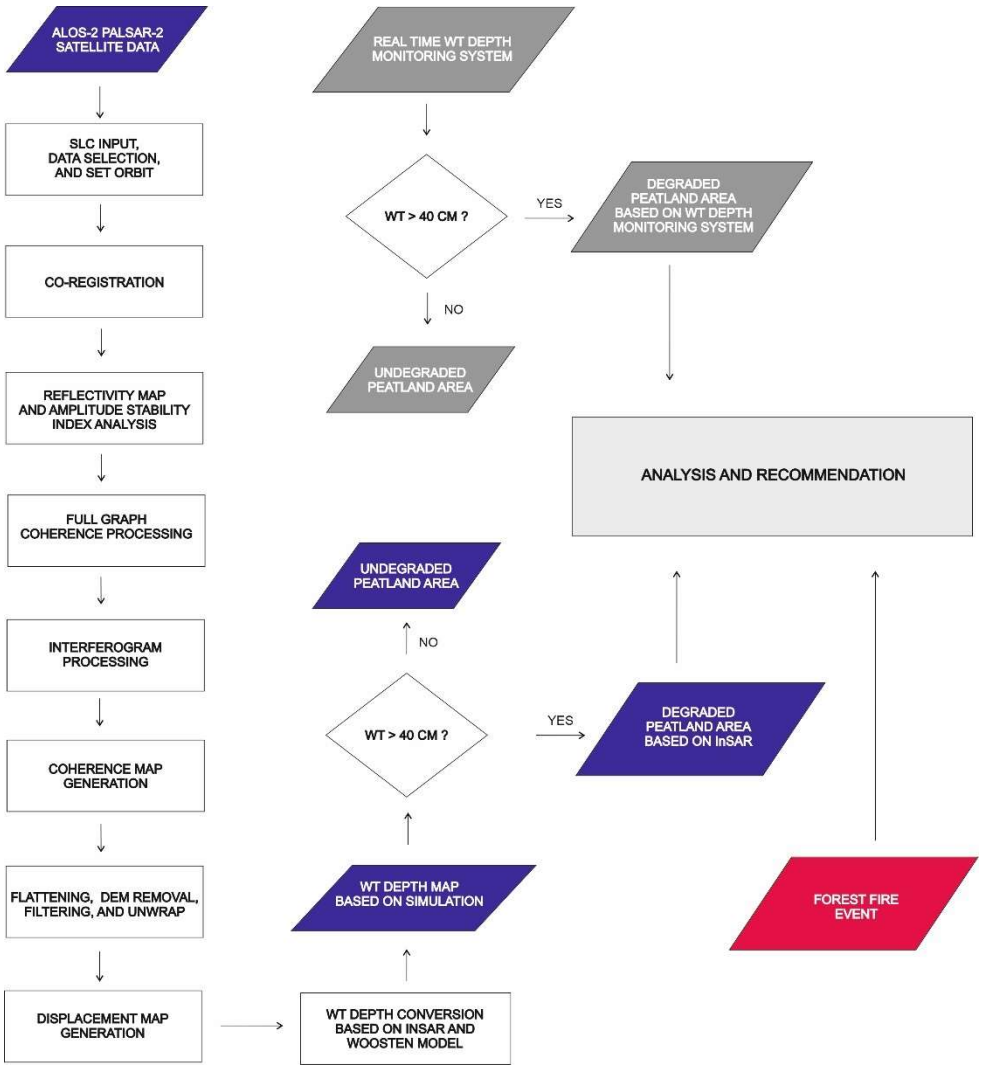

Figure 3. 4. Flowchart of Research 2 [24]

3.5. Material and Field Survey

3.5.1. Material

For the Siak, Sumatera, four ALOS-2 data images were to be processed in this research on August 30, 2014, May 9, 2015, March 25, 2017, and August 2, 2017. For Pulang Pisau Regency used data recorded on February 25, 2016, and February 2, 2018. Specification of the data as shown in Table 3.1, below

Table 3. 1.Brief information about ALOS-2 PALSAR-2 data

No	Item	Specifications
1	Sensor Type	ALOS-2 PALSAR 2
2	Data Format	SLC
3	Frequency	L-Band
4	Wavelength	0.24 meter
5	Polarization	Dual-Pol HH and VV
6	Acquisition Date	August 30, 2014, May 9, 2015, March 25, 2017, and August 2, 201725 (For Siak) and Feb. 2016 and 2 Feb. 2018 (For Pulang Pisau)
7	Acquisition Mode	Ascending
8	Acquisition Heading	−126.2211
9	Incident Angle	36.295 degree

3.5.2. Field Survey

Relate to Siak Regency, between 26 July to 10 August 2017, field surveys and samples obtained. In the peatland area, soil sampling was performed, consisting of 18 sample points. For position measurement, a handheld Global Positioning System was used, and another testing was determined by DGPS (Leica 1200+). Thus, soil samples were taken by the dielectric constant probe package (Agilent 85070E model), using the network analyzer to measure the dielectric constant real and imaginary. Twenty-five needles were used to capture the surface roughness, as soil roughness meters. Field survey activities are shown in Figure 3.6, where the sampling points and hydrological condition shown in Fig.3.5. and coordinate of sampling, as shown in Table 3.2.

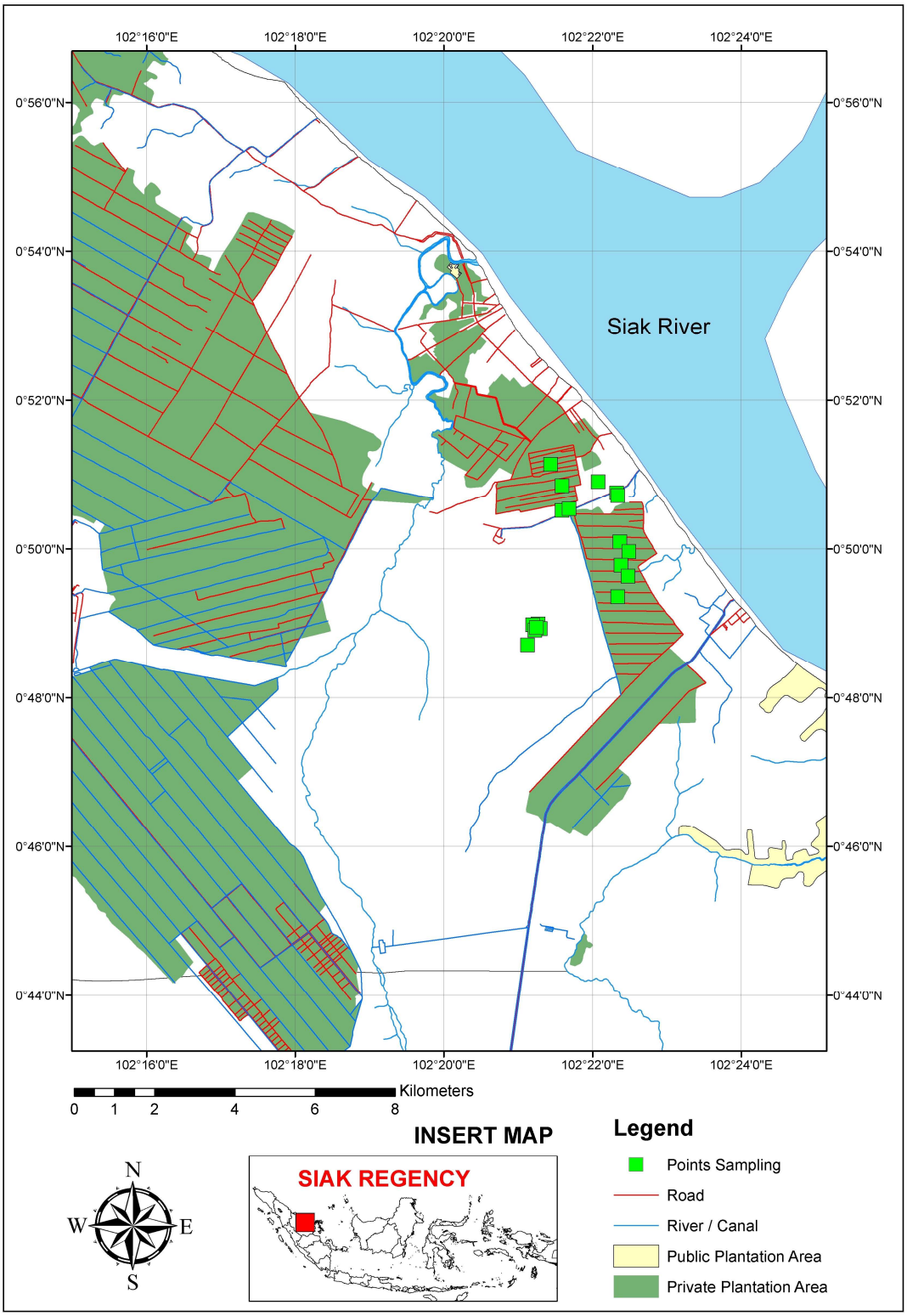

Figure 3. 5. Sampling position in Siak Regency

Table 3. 2. Sampling coordinate in Siak Regency, Riau Province

Point No.	Position	
	Latitude	Longitude
1	0.83492	102.37277
2	0.83273	102.37481
3	0.82263	102.37227
4	0.82965	102.37302
5	0.82721	102.37461
6	0.85234	102.35321
7	0.81651	102.35446
8	0.81551	102.35495
9	0.81636	102.35321
10	0.81511	102.35376
11	0.81576	102.35406
12	0.81183	102.35207
13	0.84194	102.35983
14	0.84274	102.36142
15	0.84751	102.35978
16	0.84846	102.36789
17	0.84592	102.37207
18	0.84527	102.37232

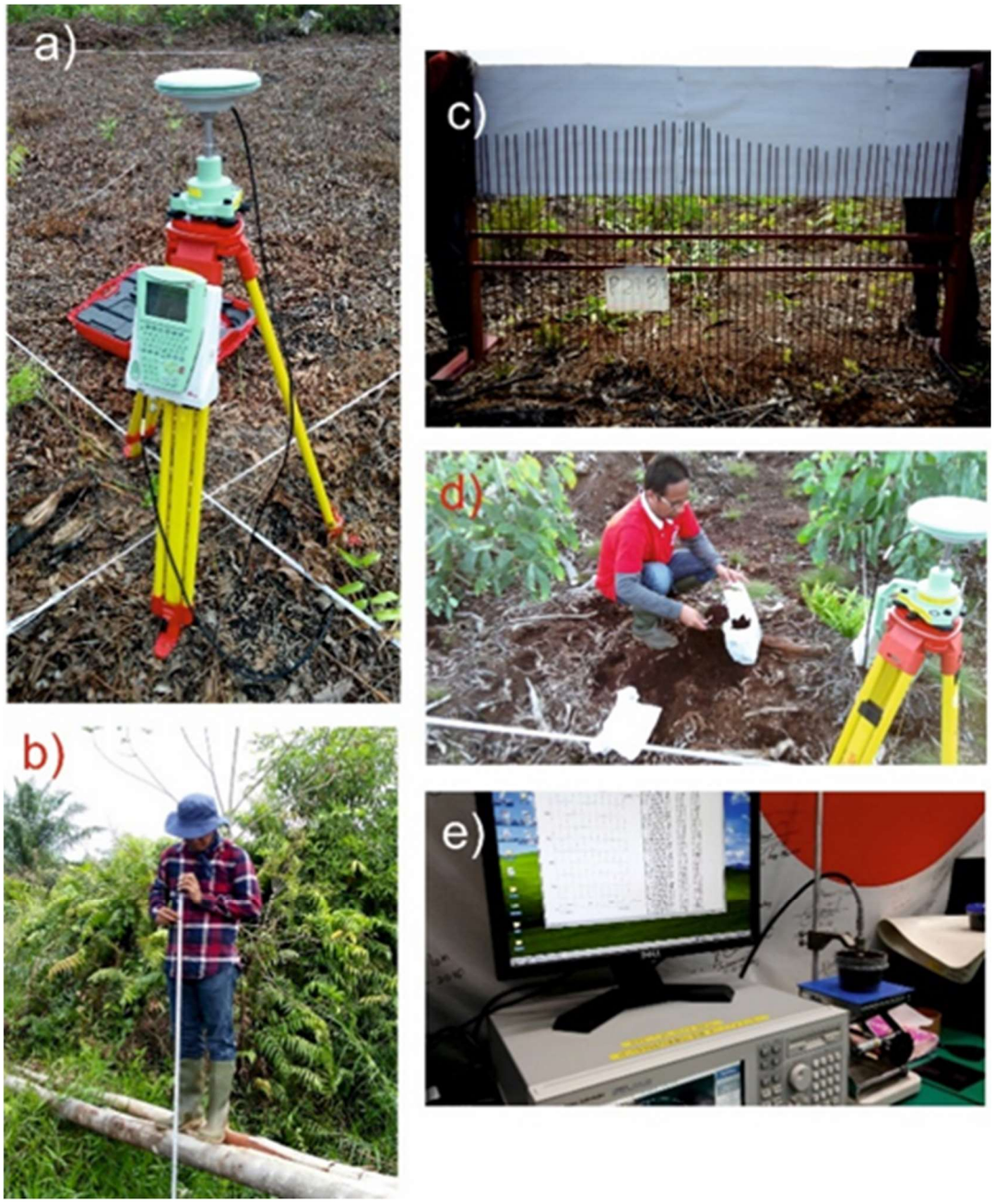

Figure 3. 6. a) GPS measurement, b) Sampling of water level in peatland c) SR measurement, d) soil collection, e) Dielectric constant analysis in JMRSL [20]

In the case of research in Kalimantan, this study used data from the groundwater table or water table depth station operated by Peatland Restoration Agency (BRG) and Agency for the Assessment and Application of Technology (BPPT). The station sends water table depth data every hour, namely SIPALAGA. The distribution of the stations shown in Table 3.2. below:

Table 3. 3. Position of Water Table Depth Stations in Kalimantan

No	Groundwater Station	Latitude	Longitude
1	Pilang 1, Jabiren Raya	−2.379	114.059
2	Pilang 2, Jabiren Raya	−2.486	114.195
3	Jabiren 1, Jabiren Raya	−2,508	114.169
4	Jabiren 2, Jabiren Raya	−2.544	114.169
5	Saka Kajang, Jabiren Raya	−2.552	114.181
6	Henda 1, Jabiren Raya	−2.612	114.244
7	Henda 2, Jabiren Raya	−2.599	114.192
8	Garung, Jabiren Raya	−2.65	114.22
9	Kalawa, Kahayan Hilir	−2.707	114.22
10	Buntoi, Kahayan Hilir	−2.831	114.175
11	Anjir Kalampan, Kapuas Barat	−2.812	114.313
12	Sebangau Jaya, Sebangau Kuala	−2.879	113.838
13	Medura Sebangau, Sebangau Kuala	−2.895	113.764

The distribution of station, shown in Fig. 3.7, below

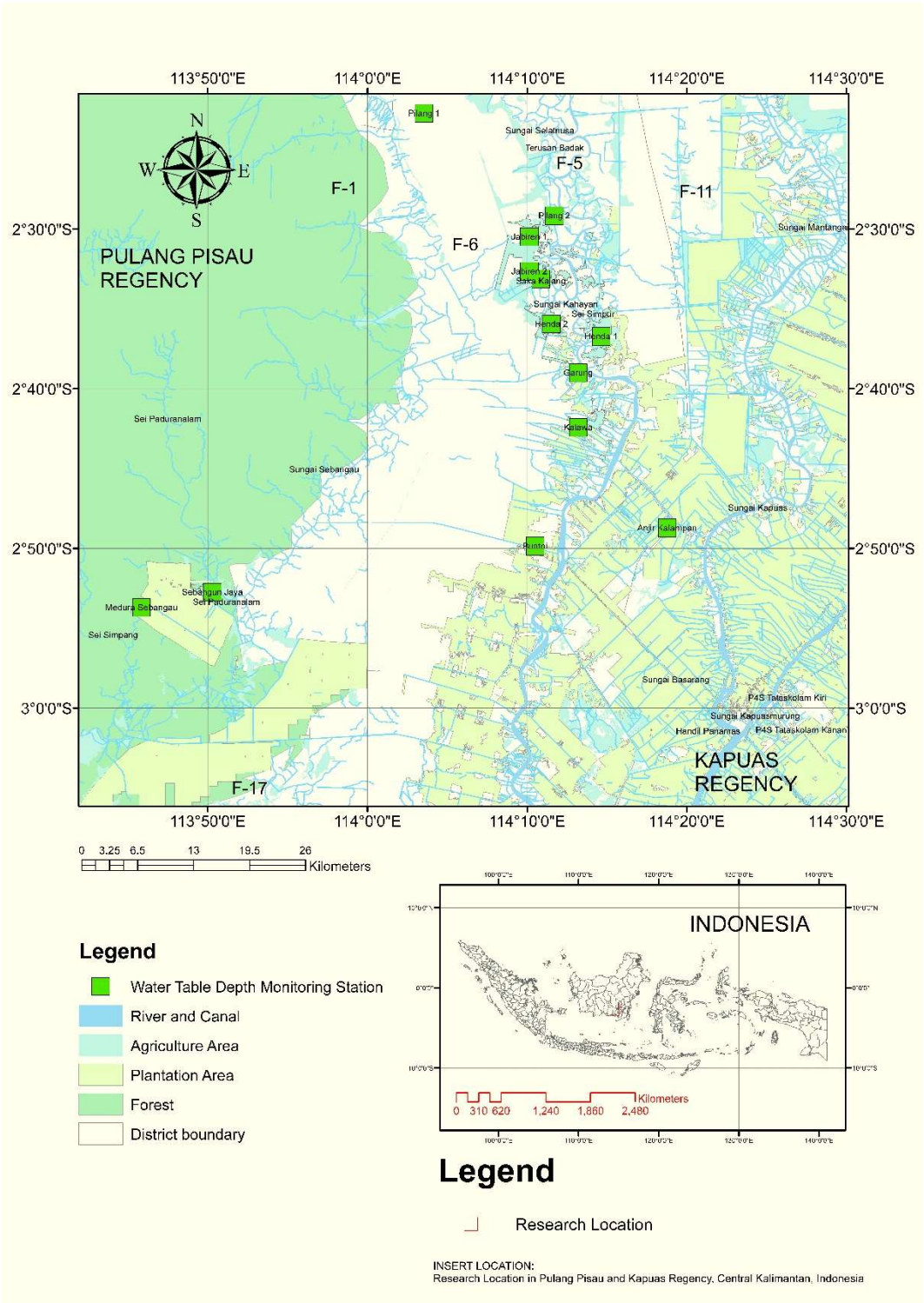

Figure 3. 7. Distribution of Water Table Depth Stations in Kalimantan

Chapter 4. Result and Discussion

4.1. Identification of peatland in the field area

Peatland is identified by the physical characteristics of the soil, which is dark in color [18]. Besides that, Peatland has a very high pH content, which is between 3-5.5. In this research, soil sampling and pH measurements were also carried out at the location with the results shown in Table 4.1.

Table. 4. 1. pH content in Peatland

Point Position No.	pH
1	3.25
2	3.46
3	3.62
4	3.55
5	3.73
6	3.65
7	3.56
8	3.6
9	4.05
10	3.87
11	3.50
12	3.72
13	4.19
14	3.70
15	4.24
16	3.82
17	4.06
18	3.71

Based on Table 4.1. the pH content is identical to peatland characteristics. In addition, the identification of peatlands is also assisted by based on data from a 1: 250,000 scale geologist map released by the Ministry of Energy and Mineral Resources, Indonesia, as shown in Figure 4.1.

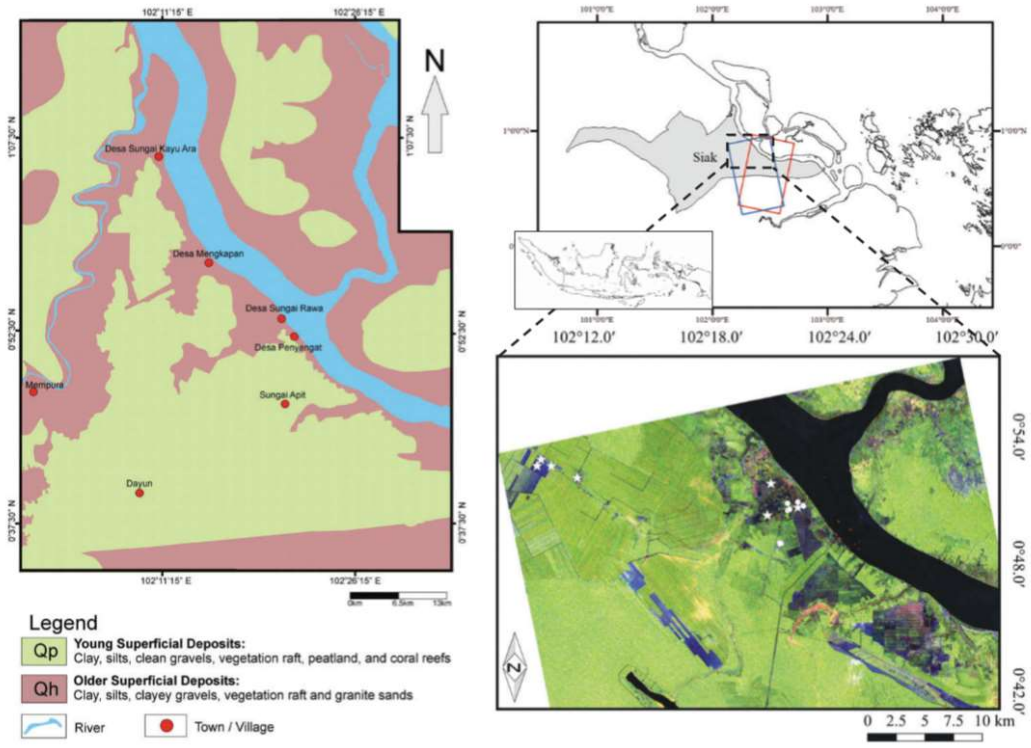

Figure 4. 1. Geological Map and Yamaguchi 4 Component Polarimetric Decomposition in RGB of Peatland in Siak, Riau Province, Indonesia [11]

Identification peatland area for Kalimantan Study (Research 2) based on the quadrant angle, Amuntai 1713 Indonesia geological map. Land cover and scene boundary of ALOS-2 PALSAR-2 in Kalimantan data shown in Fig. 4.2.

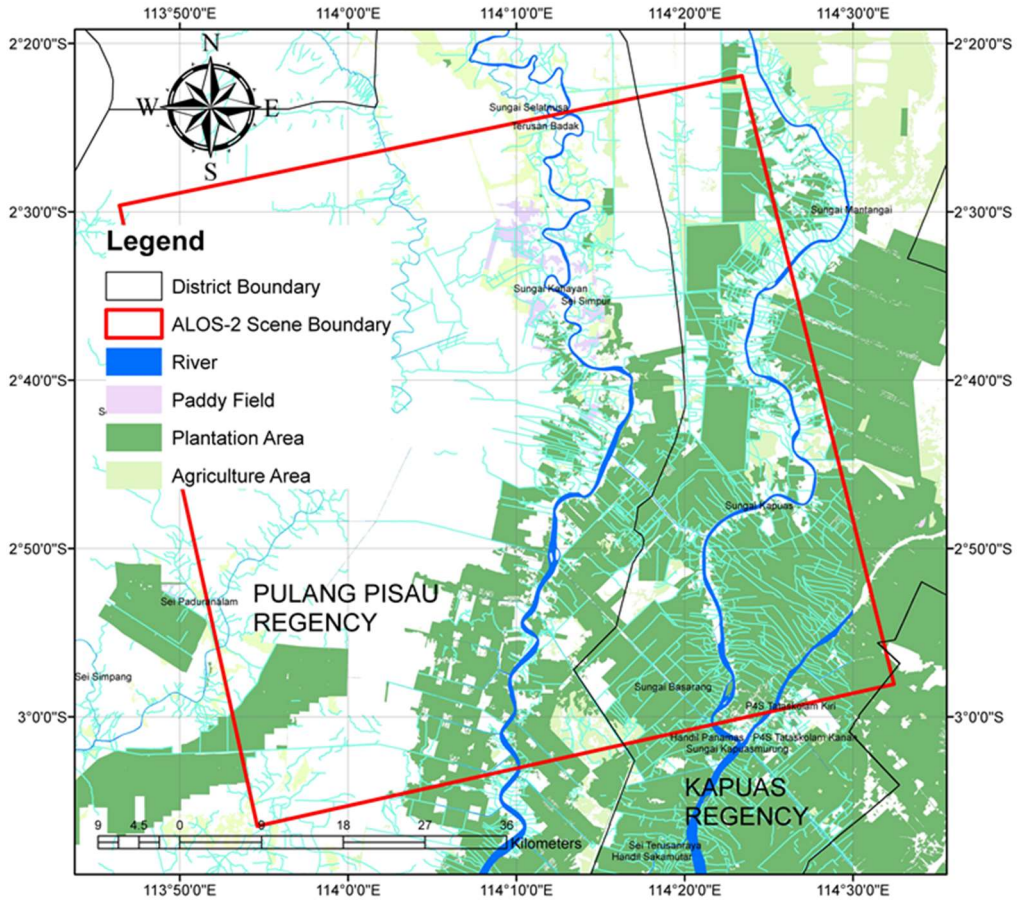

Figure 4. 2. Land cover and Scene boundary of ALOS-2 PALSAR-2 data used for Central Kalimantan Study (Research 2) [24]

4.2. Relationship between the dielectric constant water table depth (groundwater) in Peatland

Mc Pearson's method of correlation and linear regression used to know the relation between the dielectric constant and the groundwater table. Table 4.1. shows the sum of the dielectric constant calculated in both a real part and an imaginary component.

Table. 4. 2. The dielectric constant and groundwater table level data among all of the samples

Sample No.	Dielectric Constant (DC)		Groundwater Table (cm)
	Real	Imaginary	
1	3.2219	0.19	84
2	3.8458	0.25	68
3	3.4452	0.26	65
4	2.7105	0.17	86
5	2.7379	0.33	87
6	2.1517	0.17	101
7	2.7166	0.19	88
8	2.7184	0.21	88
9	3.3677	0.19	88
10	3.0056	0.26	88
11	2.5591	0.21	88
12	3.7626	0.19	87
13	3.1726	0.24	81
14	2.8511	0.23	87
15	2.4919	0.21	82
16	2.0697	0.18	100
17	2.5162	0.29	102
18	2.8700	0.24	102

The dielectric constant is the essential electromagnetic component of the satellite in terms of backscattering from the Earth. The moisture of soil and soil density affected to the dielectric constant. It increases with increased soil moisture [25].

Dry conditions of the peatland are the primary trigger of a forest fire. The dry peat condition is determined by the state of the groundwater table, while some researchers called water table depth.

The average dielectric constant actual components of peat soil samples are 2.9, minimum 2.07, and maximum 3.84, respectively, in the L-Band Frequency 1.275GHz. The dielectric constant imaginary of the average of the sample was 0.22, 0.17, and 0.33. It has shown that the condition is arid and has a high fire risk.

The table of water table depth is an essential pointer for detecting the area of peat fire hazard. Indonesian regulation states that peatlands with groundwater table above 40 cm are degraded [26][27]. According to previous research, soil humidity will fall since 0.9 cm3/cm3 at capacity toward around 0.50 cm3/cm3 if the water table depth drops below 40 cm. This condition drive leads to a rapid spread of peat fire.

The groundwater level was capture from the canals or slums near the point position of the survey. Water table depth conditions of points of study, as shown in the table, are 87,33 cm, 65 cm minimum, and 102 cm maximum.

The coefficient correlation between the dielectric constant real part and the water table depth (groundwater table) was 0.7 using linear regression. The determination coefficient (R2) was 0.5, and it shows a strong correlation. The correlation between the dielectric and the water table depth can be expressed as:

$$Y = -13.9\,\mathrm{x} + 127.8 \qquad (3.25)$$

Based on the above equation, y is the water table depth (the groundwater table), and x is the real part of dielectric constant. Figure 4.1. displays the connection between both of them.

The relationship shows that the smaller the dielectric constant, the lower the GWT, and if the peat soil drier, the potential for the forest fire was also higher.

The correlation between the dielectric constant (imaginary) and the GWT is small, approximately 0.17. It shows almost no relationship. The relationship is shown in Fig.4.3.

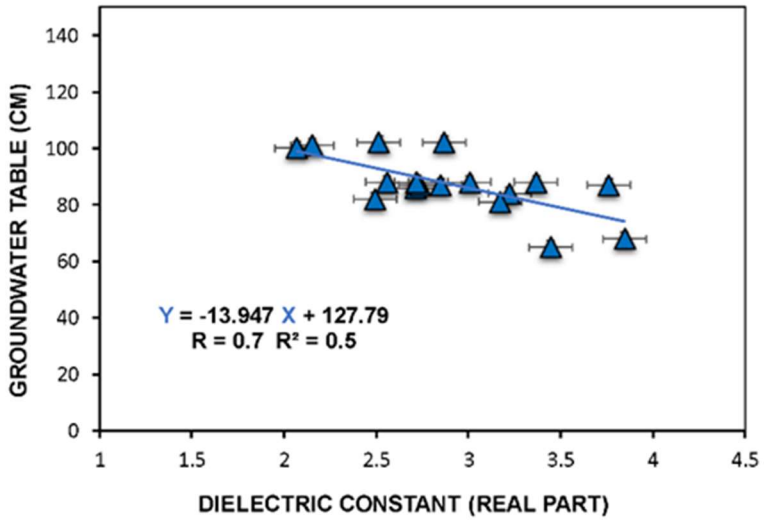

Figure 4. 3. Graph that shown correlation between groundwater table and real part of dielectric constant [20]

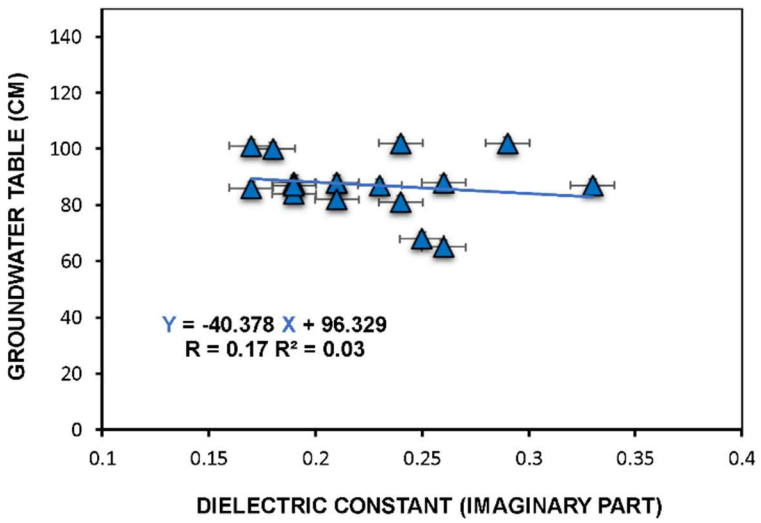

Figure 4. 4. Graph that shown relationship between groundwater table and imaginary part of dielectric constant [20]

4.3. Relationship between backscattering coefficient (sigma zero) and water table depth (groundwater) in Peatland

The relationship between the backscattering coefficient of ALOS-2 PALSAR-2 and the groundwater level was examined by this study. Backscattering coefficient captured, after processing step by Lee filtering 5x5, and Terrain Georectification. Image of HH, HV, VH, and VV polarization shown in Fig. 4.5.

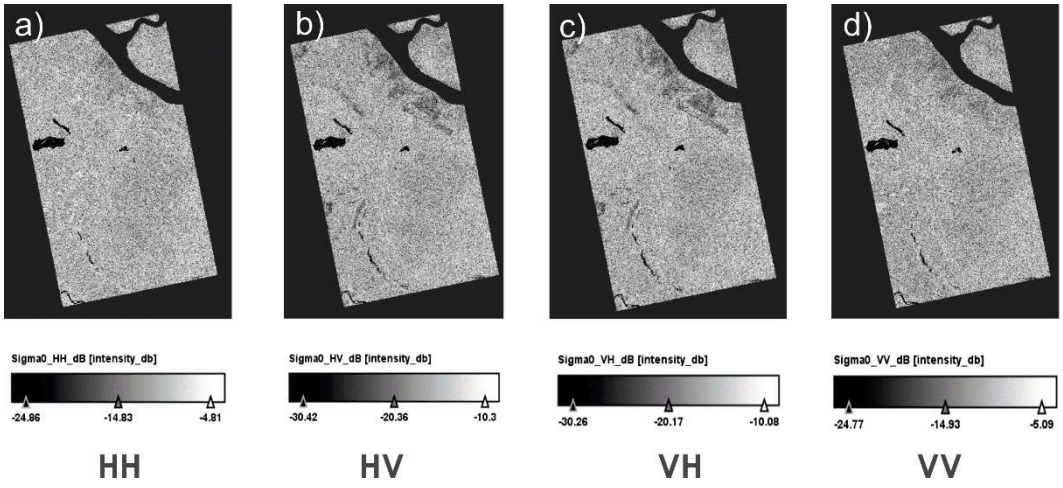

Figure 4. 5. Image of ALOS-2 PALSAR-2 data of Siak Regency, Riau, Indonesia, base on (a) Horizontal-Horizontal, (b) Horizontal-Vertical, (c) Vertical-Horizontal, and (d) Vertical-vertical polarization

Backscattering of all of the polarization mode ALOS-2 PALSAR data among point sampling, shown in Table 4.3.

Table. 4. 3. Table of Bacscatteing Coefficient among sampling point

Sample No.	Backscattering Coefficient (dB)			
	HH	HV	VH	VV
1	-12.80	-23.56	-18.09	-11.38
2	-13.50	-19.68	-17.52	-16.99
3	-12.81	-18.86	-19.98	-7.22
4	-12.50	-18.66	-18.93	-8.13
5	-13.54	-20.04	-23.93	-17.12
6	-16.34	-29.17	-22.39	-16.49
7	-14.65	-18.15	-27.39	-12.82
8	-13.38	-24.24	-22.07	-14.16
9	-12.06	-29.70	-19.66	-11.18
10	-13.80	-33.72	-34.91	-12.48
11	-12.15	-25.47	-31.30	-12.24
12	-11.40	-18.96	-20.14	-16.25
13	-13.90	-30.06	-19.63	-11.56
14	-13.41	-24.44	-22.46	-15.03
15	-14.16	-22.53	-23.09	-14.61
16	-16.60	-27.52	-19.34	-15.87
17	-15.13	-35.63	-21.16	-20.43
18	-13.87	-18.86	-25.53	-14.34

Relationship between the backscattering coefficient and groundwater level in peatland areas shown in Table. 4.3.

Table. 4. 4. Table of coefficient correlation and coefficient determination between the backscattering coefficient and groundwater table

	HH Polarization	HV Polarization	VH Polarization	VV Polarization
Coefficient Correlation	-0.5	-0.4	-0.2	-0.5
Coefficient Determination	0.2821	0.1600	0.0400	0.2333

Based on Table 4.4. the relationship between the backscattering coefficient and the groundwater table significant for HH and VV polarization amount 0.5. The result of the correlation coefficient also appropriates with the correlation coefficients between the dielectric constant and groundwater table.

In the relationship expressed by the equation:

$$Y = -3.6308\,X + 36.892 \quad (4.26)$$

Where Y is the groundwater table, and X is backscattering coefficient HH Polarization ALOS-2 L-Band Frequency.

and equation:

$$Y = -1.4843\,X + 66.858 \quad (4.2)$$

Where Y is the groundwater table, and X is backscattering coefficient VV Polarization ALOS-2 L-Band Frequency.

4.4. Identification of flammable peatland area based on transmission line theory

The basic idea of this method is to calculate the amount of backscattering coefficient based on various parameters that influence it based on the theory of the transmission of electromagnetic wave lines. These parameters include the incident angle, dielectric constant, and soil roughness. The incident angle was captured from ALOS-2 PALSAR-2 and the soil roughness obtained from the ground. Table 4.2. shows the incident angle and surface roughness from the ground.

Table. 4. 5. Incident angle and soil roughness captured from satellite data and the ground

Point Position No.	Incidence Angle	Soil Roughness
1	30.4	0.23
2	32.2	0.72
3	32.9	0.21
4	32.3	0.88
5	32.1	1.10
6	33.5	1.57
7	31.7	1.71
8	31.7	6.23
9	32.6	3.35
10	31.0	5.83
11	31.5	2.44
12	31.6	2.71
13	31.1	2.36

14	31.7	1.42
15	32.8	4.42
16	31.5	0.24
17	32.8	1.38
18	32.2	1.38

Thus, based on calculations, the backscattering coefficient value has been obtained based on ALOS-2 PALSAR-2 Horizontal-horizontal (HH) polarization data and backscattering coefficient simulated by impedance model, as exposed in Table 4.3.

Table. 4. 6. Backscattering Coefficient captured from ALOS-2 PALSAR-2 data and based on the simulation model

Point No.	Backscattering coefficient of ALOS-2 PALSAR-2	Backscattering Coefficient Based on Simulation
1	-12.80	-12.59
2	-13.50	-11.50
3	-12.81	-12.41
4	-12.5	-14.39
5	-13.54	-14.26
6	-16.34	-17.21
7	-14.65	-14.26
8	-13.38	-14.27
9	-12.06	-12.54
10	-13.80	-13.25
11	-12.15	-14.83
12	-11.40	-11.58
13	-13.90	-12.81
14	-13.41	-13.83
15	-14.16	-15.34

16	-16.6	-17.29
17	-15.13	-15.24
18	-13.87	-13.85

The backscattering coefficient of ALOS-2 PALSAR-2 data publicized in Table 4.3. with minimum -16.6 dB and maximum -11.4 dB, so that the average is -13.67 dB. Based on the simulation, the backscattering coefficient, minimum -11.5 dB, and maximum -17.29 dB, and then the average -13.97 dB.

This study determined the relationship between the backscattering coefficient information based on ALOS-2 PALSAR-2 data and the backscattering coefficient simulation by the impedance model simulation. The relationship of backscattering coefficient simulation and backscattering coefficient captured from ALOS-2 PALSAR-2 data is high; the coefficient correlation is 0.8, and the coefficient determinant is 0.6, and also, the RMSE is 0.4, as exposed in Fig.4.6. It means that the identification of the peatland risk fire area was successful based on the impedance model using ALOS-2 PALSAR-2 data. ALOS-2 PALSAR-2 backscattering coefficient represents a dry peat field with a weak dielectric constant. The area with a week dielectric constant then classified as high risk to fire or flammable area.

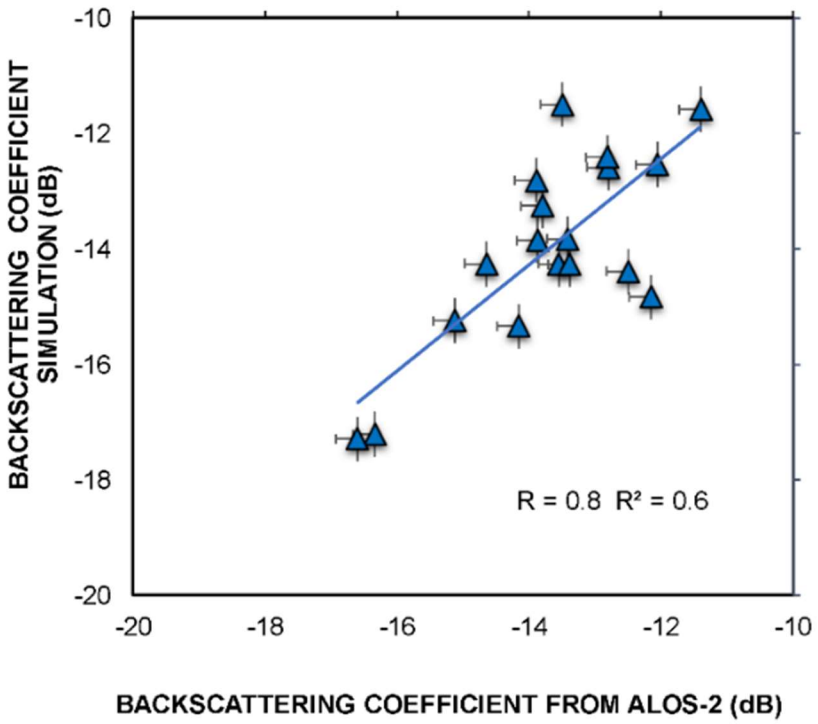

Figure 4. 6. Relationship backscattering based on satellite data and simulation [20]

Although this research has significant results, this method also has weaknesses, partly because of the thickness of the peat considered to be the same as the wavelength used. This assumption has done to facilitate the calculation due to the absence of clear peatland thickness information at this location.

The following matters also cause other limitations of this research:

1. Field sampling is not precisely the same as satellite recording due to difficulties in accessing sample point positions.
2. There are not many points of observation due to time constraints, which are only approximately seven days before and after recording satellite data.

4.5. Identification of flammable peatland area based on the DInSAR method

This study was also proposed with the DISAR Approach to detect peat fire risk areas. DInSAR was used in this study to backing a thesis based on the impedance model approach. DInSAR approach was employed on the basis that the subsidence and groundwater tables are closely related [19].

According to DInSAR method, a couple of ALOS-2 data captured in August 2014, May 2015, and March 2017 were processed. ALOS-2 PALSAR-2 data with the format by Single Look Complex was employed as a master and also slave image to the co-registration stepping work. Pair A used an image from ALOS-2 PALSAR-2 that was acquired on 30 August 2014 as master and acquired 09 May 2015 as a slave.

Pair B used the image that was acquired on May 9, 2015, as a master, and that was acquired on March 25, 2017, as a slave. The interferogram process was formed after co-registration. The coherence map and interferogram process are thus presented in Fig. 4.7.

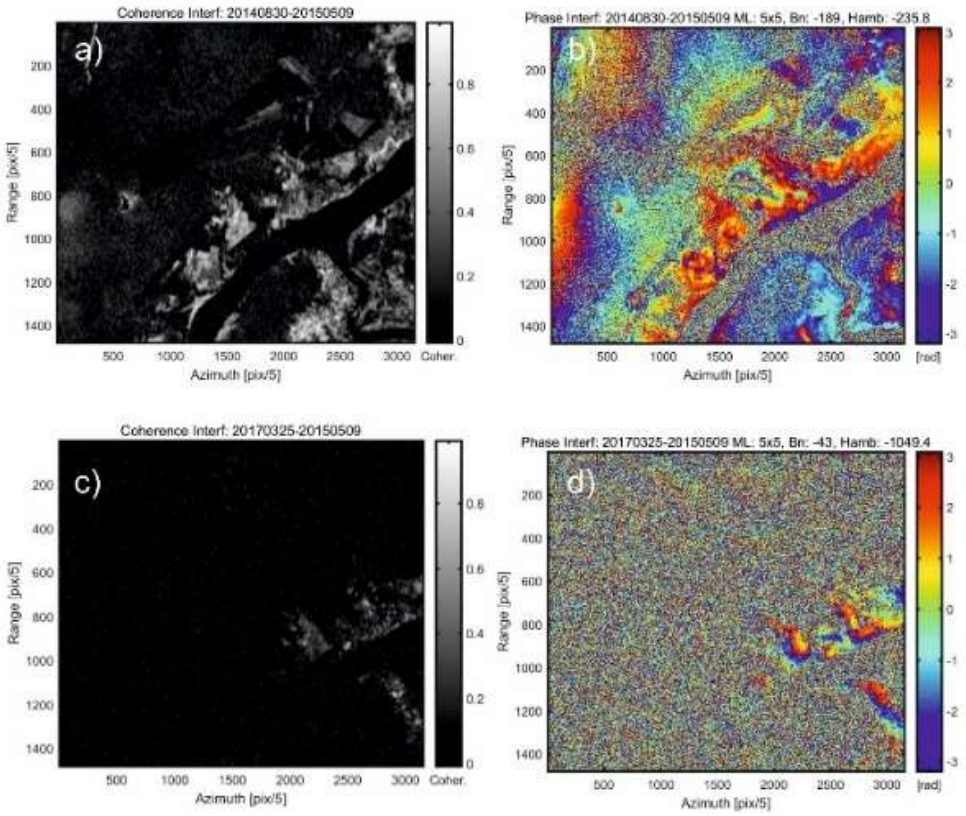

Figure 4. 7. (a) Coherence map and (b) Interferogram of Pair A, and (c) Coherence Map and (d) Interferogram of Pair B [20]

Phase interferogram of Pair A developed based on Multi Looking 5 x 5 pixels, Goldstein Filtering 5x5 pixels. Normal Baseline of this pair image is189 m, and ambiguity 235.8. Phase interferogram of Pair B developed with Multi Looking 5 x 5 pixels. Goldstein Filtering is employed by 5x5 pixels. The Normal Baseline of this pair image is 43 m, and height ambiguity 1049.4. The quality of interferogram influence by the normal baseline [20]. The coherence map of Pair A is more extensive then Pair B.

Based on the pair A and pair B processes, DInSAR requires that not all the 18 points used in the simulation of impedance models are compatible in the DInSAR system. There are ten coherence points based on Pair A, and there are seven coherence

points based on Pair B. The span between pair A and pair B was also different; pair A is nine months, and pair B is 24 months. Due to this condition, the calculation of the annual subsidence rate of pair A and pair B employed a different correction factor.

In order to calculate the annual subsidence rate, Pair A's subsidence result multiplied by 12/9 and Pair B's subsidence result, divided by 2 to calculate the yearly subsidence rate. Pair A typical annual subsistence rate was 6.6 cm/year, with a minimum of 6 cm/year and a maximum of 7.5 cm/year. For average pair B, the annual subsidence rate was 2.8 cm/year, and the minimum is 2.5 cm/year and a maximum 3.5 cm/year. The period of Pair A is connected to El Nino in Indonesia if it is dry, and a lot of forest fire takes place in Indonesia [7].

The relationship between annual rate subsidy and groundwater table depth is explained using the Woosten Model[29]. The groundwater table is calculated and shown in Table 4.4 based on the DInSAR approach.

Table. 4. 7. Subsidence rate and simulation of groundwater in Siak Regency

Point No.	Annual Subsidence Rate (cm/year)		GWT Depth Simulation (cm)	
	Pair A	Pair B	Pair A	Pair B
1	6.7	-	167	-
2	6.0	2.5	150	63
3	-	3.2	-	80
4	6.4	3.2	167	79
5	6.4	-	167	-
6	7.5	-	187	-
7	-	-	-	-
8	-	-	-	-
9	6.4	3.3	160	82
10	6.4	3.5	160	87
11	-	-	-	-
12	-	-	-	-

13	-	-	-	-
14	-	-	-	-
15	-	-	-	-
16	6.7	3.4	167	84
17	6.7	-	167	-
18	6.7	3.3	167	81

The simulation groundwater table for pair A, based on Table 4.4., is 165.6 cm on average, with a minimum value of 150 cm and a maximum value of 187 cm. On average, the groundwater table for Pair B is 69.4 cm, with a minimum of 63 cm and a maximum of 87 cm.

Based on the groundwater table simulation, it confirms that the groundwater table is less than 40 cm for each point and that the peatland region is dangerous for fire. The peat fire also happened in the field area during the field study, as shown in Fig. 4.8., water boom used by helicopters to keep the peatland from firing.

Figure 4. 8. The fire occurred in peatland areas during a field survey

Compare then using the Mac Pearson correlation test to validate the correlation between the simulation of the groundwater table and the groundwater table on a field study basis.

Based on the correlation test from the Pair A groundwater simulation table and the field survey, the value of the correlation coefficient was 0.71 (R), and the coefficient of determination (R2) was 0.51. Then, the correlation test between the Pair B simulation table and the field survey provided a correlation value (R) 0.85 and a coefficient of determination (R2) 0.73. The test graph is shown in Fig. 4.9.

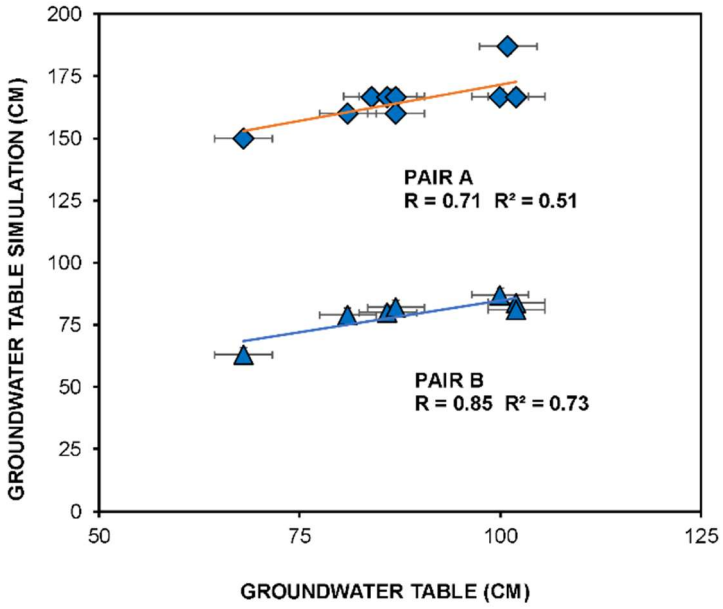

Figure 4. 9. The relationship among the groundwater table simulation of Pair A (red line) and Pair B (blue line) and field survey data. [20]

The DInSAR approach shows that the peat fire risk area can also be identified in this way.

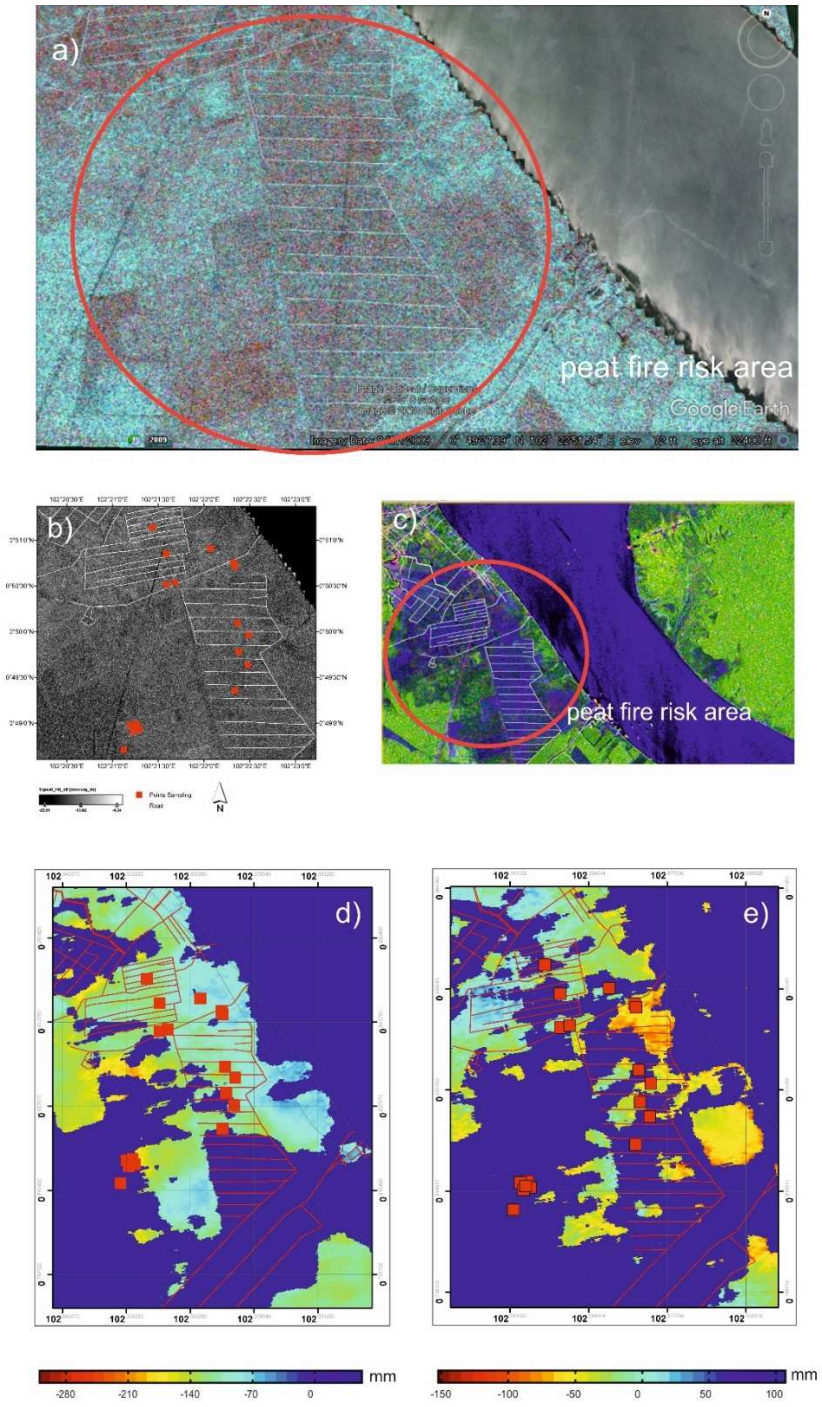

Figure 4. 10. (a) Peat fire risk area shown in red color (b) Backscattering coefficient of ALOS-S PALSAR-2 data (c) Peat fire risk area on RGB composite of Yamaguchi Decomposition (d) Subsidence rate of of PaIr A, and (e) Subsidence rate of Pair B [20]

4.6. Assessment of degraded peatland based on DInSAR and groundwater table depth stations related to forest fire

4.6.1. Degraded of peatlands based on DInSAR

Based on the SAR interferometry analysis, the coherence interferogram map was obtained using the ALOS-2 PALSAR-2 data. The ALOS-2 PALSAR-2 data recorded in Feb. 2016 and Feb. 2018 as a reference. The interferogram map for coherence is the product of a cross-relation of two image pairs. Concerning the analysis results, as shown in Figures 4.11.(a), due to significant temporal correlations, the interferogram could not be created on the entire image. Vegetation cover dynamics usually cause temporal decorrelation in peatlands.

The interferogram images have been created using a pair of synthetic aperture radar images, particularly in the area of coherence. The predicted interfaces are accurate, with a small standard baseline of -83 and uncertainty of -645. The land deformation map is created based on stepping the work of the interferogram image generation, flattening, remove Digital Elevation Model, and unwrapping.

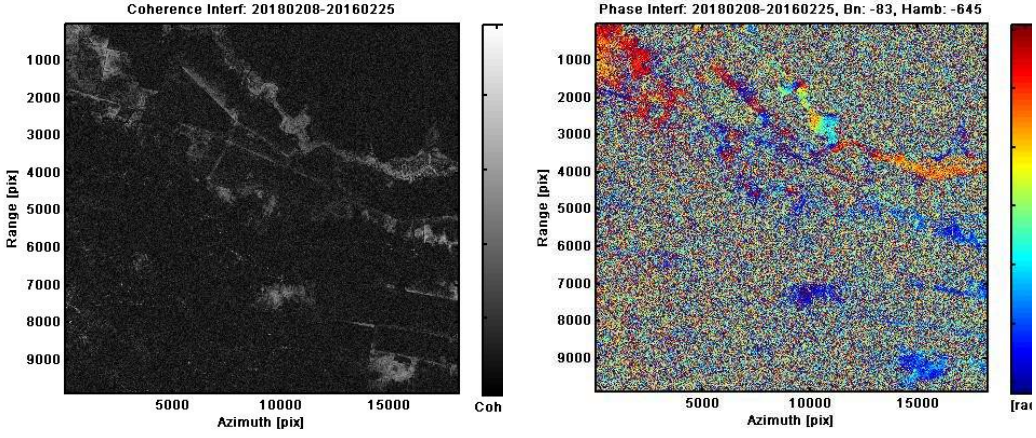

(**a**) (**b**)

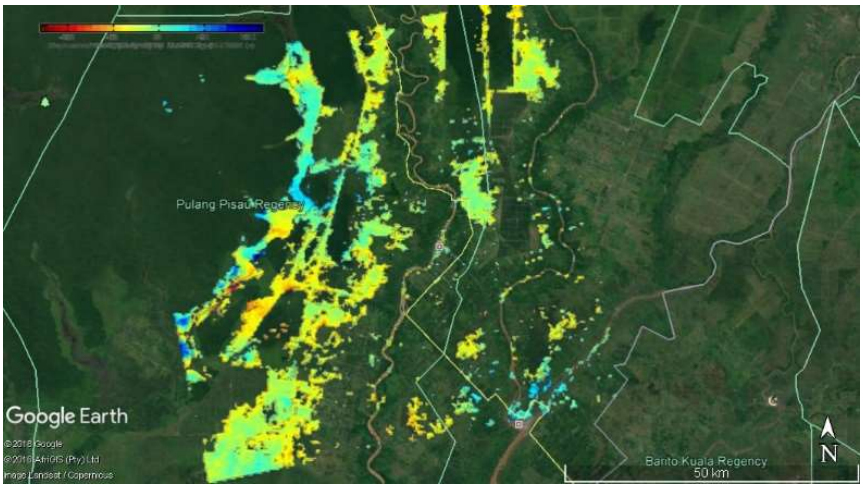

(**c**)

Figure 4. 11. (a) Coherence map; (b) image of phase interferogram; and (c) land subsidence map over google earth application [24]

Figure 4.8.(c) shows that land subsidence has occurred in most of the study areas that make up the peatland. This investigation was carried out in two neighboring districts, Pulang Pisau and Kapuas Regency, in which bogs were dominant in these areas. Figure 4.12. shows the map of degraded and non-degraded peatlands from study sites. Degraded peatland maps were generated annually following the Woosten model, based on the results of the land deformation analysis by SAR interferometry. It can also be realized that peatlands belong to degraded areas within the context of this research. There are only insignificant areas along the River of Sebangau and certain areas in the north-west wherever the peatland conditions are not degraded.

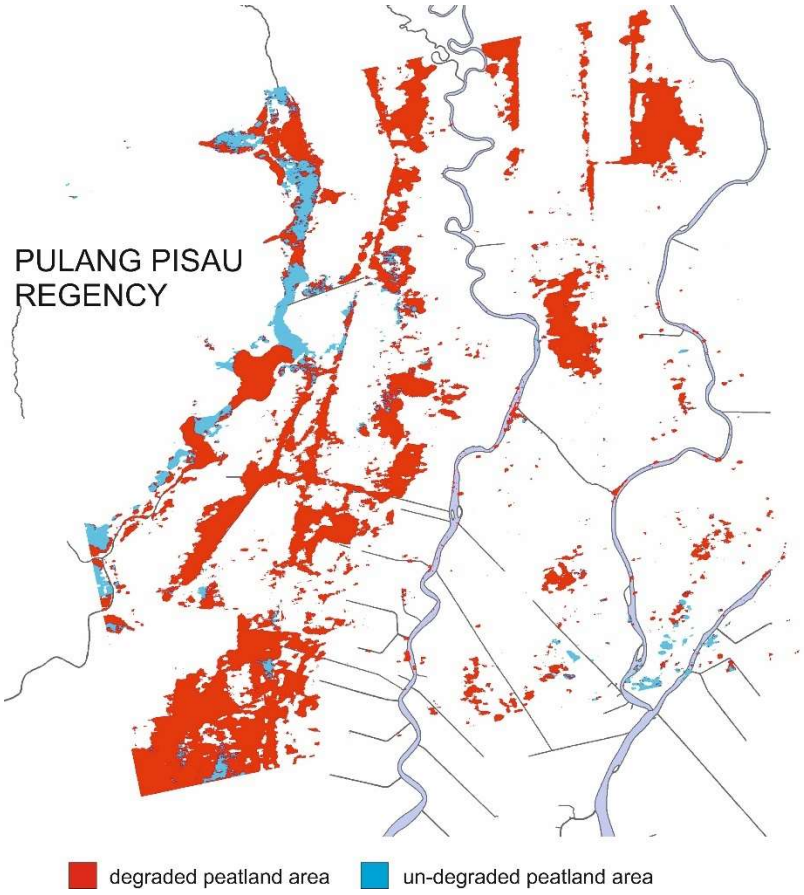

Figure 4. 12. Degraded and un-degraded peatland area in Kalimantan based on DInSAR and Woosten Model

4.6.2. Review of groundwater table station's effectivity to detect degraded peatland area related to the forest fire.

Data from the 13 water tables (WT) monitoring systems established by Peatland Restauration Agency of Indonesia (BRG) and SIPALAGA, including the location of the stations of Pilang 1, Pilang 2, Jabiren 1, Jabiren 2, Saka Kajang, Henda 1, Henda 2, Garung, Kalawa, Buntoi, Anjir Kalampan, Sebangau Jaya, Medura Sebangau, were used in these research projects. In Kapuas Regency district, only one station, namely Anjir Kalampan station, is involved, while in the Pulang Pisau Regency area, there are 12 other stations.

The station's groundwater table level/WT depth monitoring system in real-time transmit data to the ground station 24 hours a day. The results of the measurements from Jan. to July 2019, are the data used in this analysis, as shown in Fig. 4.13.

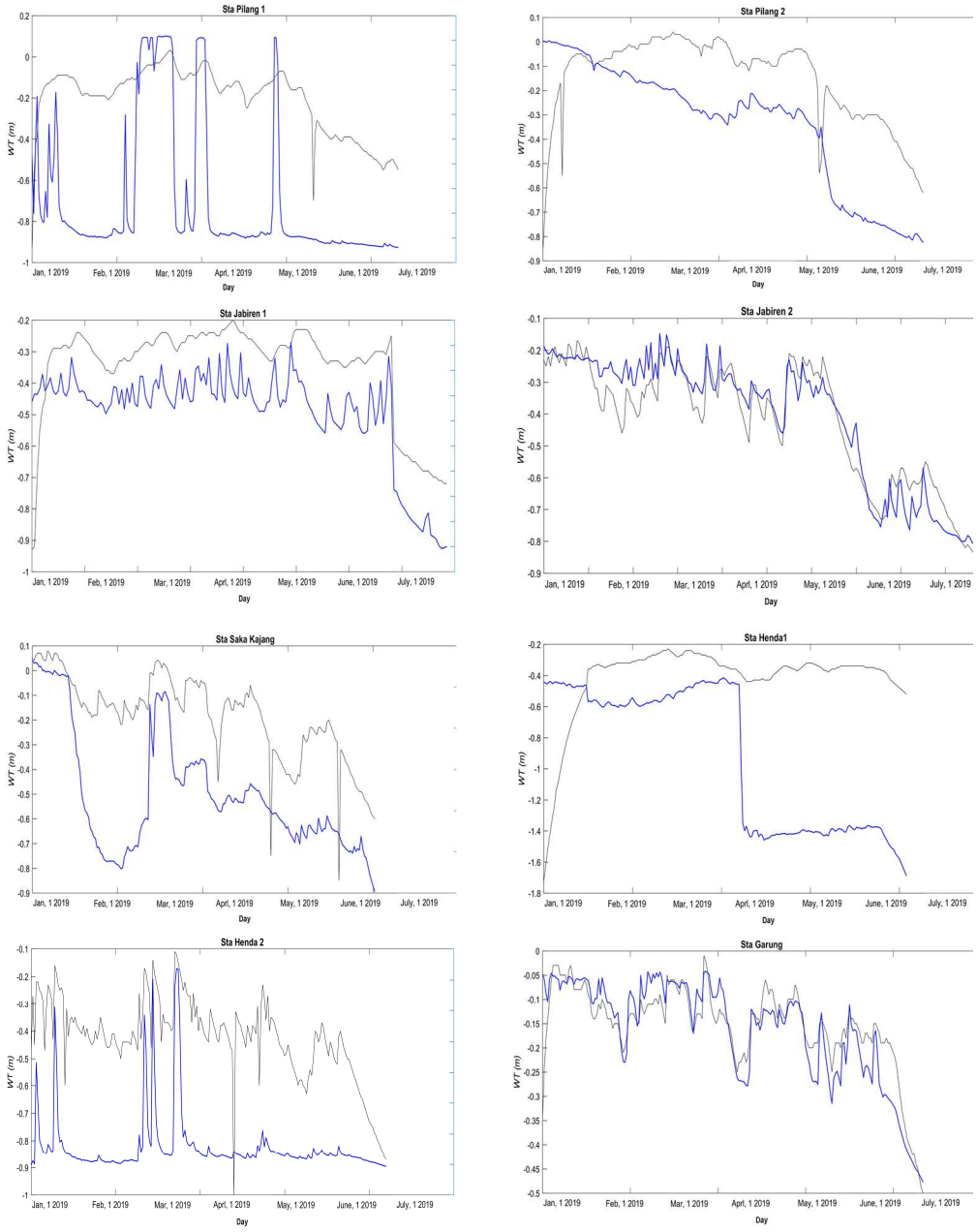

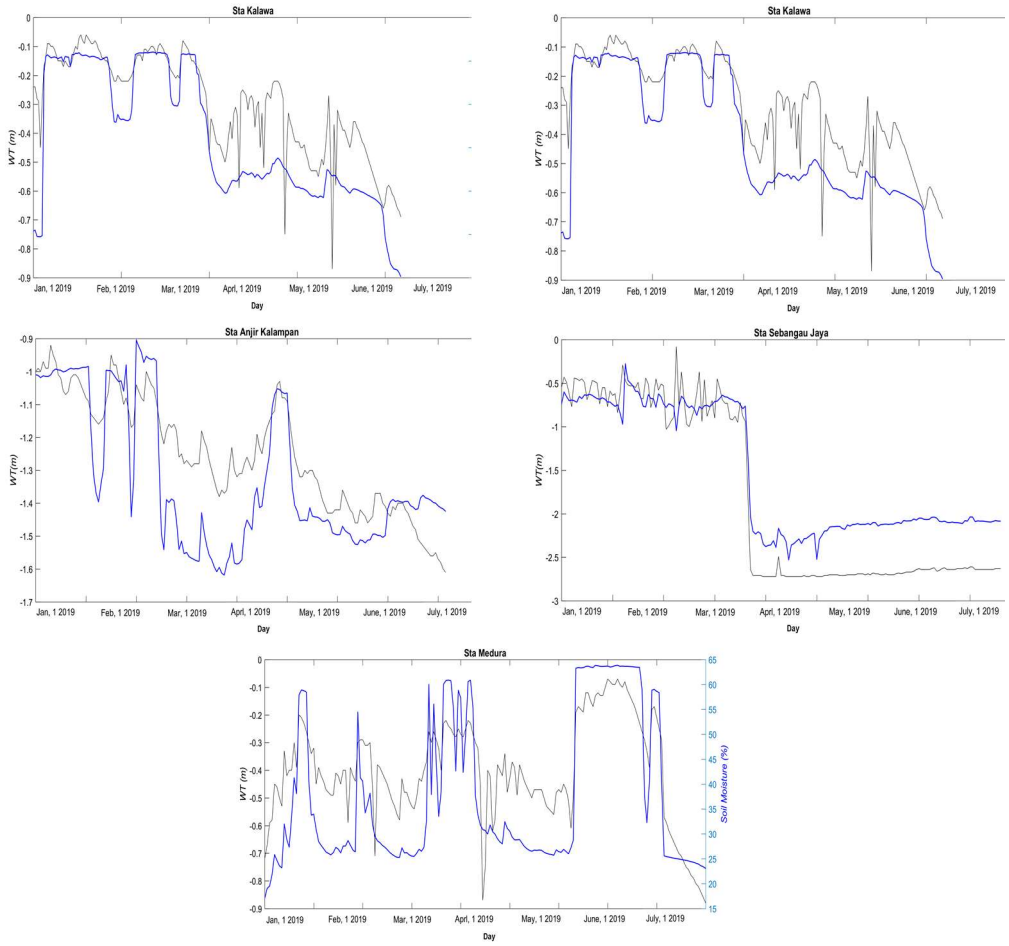

Figure 4. 13. Real-time water table depth graph of 13 stations of Pulang Pisau and Kapuas Regency [24]

As can be seen in Figure 4.10, based on Pilang Station 1, the conditions of the water table from June onwards and of Pilang Station 2 were less than 40 cm. The groundwater table level/WT depth status was also very volatile and decayed in July, based on data from Jabiren 1 station. The depth of WT dropped to less than 40 cm at Jabiren 2 station in early February and continued to deteriorate until July. In April at Saka Kajang, the depth of the WT decreased to below 40 cm, although the dynamics were quite high, and in July, the decrease was closer.

Even the state of the WT depth in Henda 1 station was deficient from January at minus 1.7 meters and continued under 40 cm until July. The decreasing condition below the 40 cm was also observed at Henda Station 2 in early January. Even

though not as weighty as at Henda Station 1, but also until July. The dropping of the WT depth at Garung station started in July. The depth decline at Kalawa Station began in January and increased slightly until April but continued until July. In Buntoi station, a similar pattern occurred.

The only station in the Kapuas Regency area in that research is the Anjir Kalampan Station, where WT depths were below 1 m from January to 1.6 m in July. From January onward, the WT depth at Sebangau Jaya station decreased below 1 m, and the condition worsened until July at 2.5 m underground level. Likewise, WT depths decreased in January from 70 cm at Medura station, and fluctuations increased until July at the height of 90 cm below the peatland level. Based on WT depth data from different stations, total peatlands in this field of research can be believed to be degraded.

This study has utilized ALOS-2 PALSAR-2 L-band wave data, the most extended existing wave in the field of satellite radar sensors that is very useful for accuracy, as the L-band sensors usually are better than C-band and X-band [34]. However, based on the SAR interferometry analysis, it looks that not all areas in this research are experiencing land subsidence, as explained earlier. This condition probably because of temporal decorrelation. Decorrelation consists of geometric decorrelation, volumetric decorrelation, temporal decorrelation, and thermal decorrelation [28]. Geometric and volumetric decorrelation is also called spatial decorrelation or baseline decorrelation respectively [29][30][31]. When sensor positions are dissimilar during acquisitions, geometric decorrelation occurs. Volumetric decorrelation is due to volume scattering, an example in the forest area. Temporal decorrelation has arisen due to changes in dielectric and structural properties of the scattered [67]. Thermal decorrelation is calculated by the thermal noise interferometric of instruments [67,68].

Figures 4.8 and 4.11 indicate land cover and land use in the vegetation-dominating areas, which is a very impenetrable forest on the western side and many farm sites

on the east. Volumetric decorrelation, therefore, leads to incoherence in many cases. Moreover, the gap in the time spent in data achievement for two years between February 2016 and 2018 is the explanation for temporal decorrelation.

Regardless of the decorrelation limitations, SAR interferometry able to measure land subsidence in peatlands. Then, with the Woosten model [20] and with the assumption that the WT depth is 40 cm characterized as a degraded peatland area [24], an overlay between the degraded peatland data and the forest fire data from BBSDLP and previous research [32] was created. The result, as publicized in Figure 4.11. This study demonstrates that the accuracy of the detection of degraded peatland areas by SAR interferometry is 88 percent, as shown in Table 4.5 when tested with forest fire data, which means that it is very accurate.

Based on all the graphs that are exposed in Figure 4.10, all groundwater table depth in the dry season shows the bottom of the water table being over 40 cm under the surface area. This condition means the peatlands have degraded and are highly risky due to their burning ability. The water table depth at Jabiren 1 and 2 stations is 56.25 cm, so the simulation results classify the water table depth into a degraded peat region, showed that this condition began in July 2019.

Table. 4. 8. Data of forest fire occurred in Pulang Pisau, Kalimantan and degraded peatland based on DinSAR and indicated by groundwater level stations

No	Forest Fire Area	Degraded Peatland Area	
		Based on SAR Interferometry	Based on WT Depth Monitoring System
1	F-1	✓	N/A
2	F-2	✓	N/A
3	F-3	✓	N/A
4	F-4	✓	N/A
5	F-5	✓	N/A
6	F-6	✓	✓
7	F-7	✓	N/A
8	F-8	✓	N/A
9	F-9	✓	N/A
10	F-10	✓	N/A
11	F-11	✓	N/A
12	F-12	✓	N/A
13	F-13	✓	N/A
14	F-14	✓	N/A
15	F-15	N/A	N/A
16	F-16	N/A	N/A
17	F-17	✓	N/A
18	F-18	✓	N/A
Coverage Level:		88%	5%

✓: Detected N/A: Not Available.

Under these circumstances, it is understood that peat fires have occurred in the Pulang Pisau district [33] during September 2019, in the Jabiren area [24]. Nevertheless, the overlying map between the water table (WT) depth or groundwater level of the site and the forest fire position indicates that forest fires have been observed only in two stations (Jabiren 1 and 2). Consequently, the cover level area of degraded peatland identification by using groundwater (WT) depth monitoring system installed in Central Kalimantan is only 5% related to forest fire, based on Table 4.5.

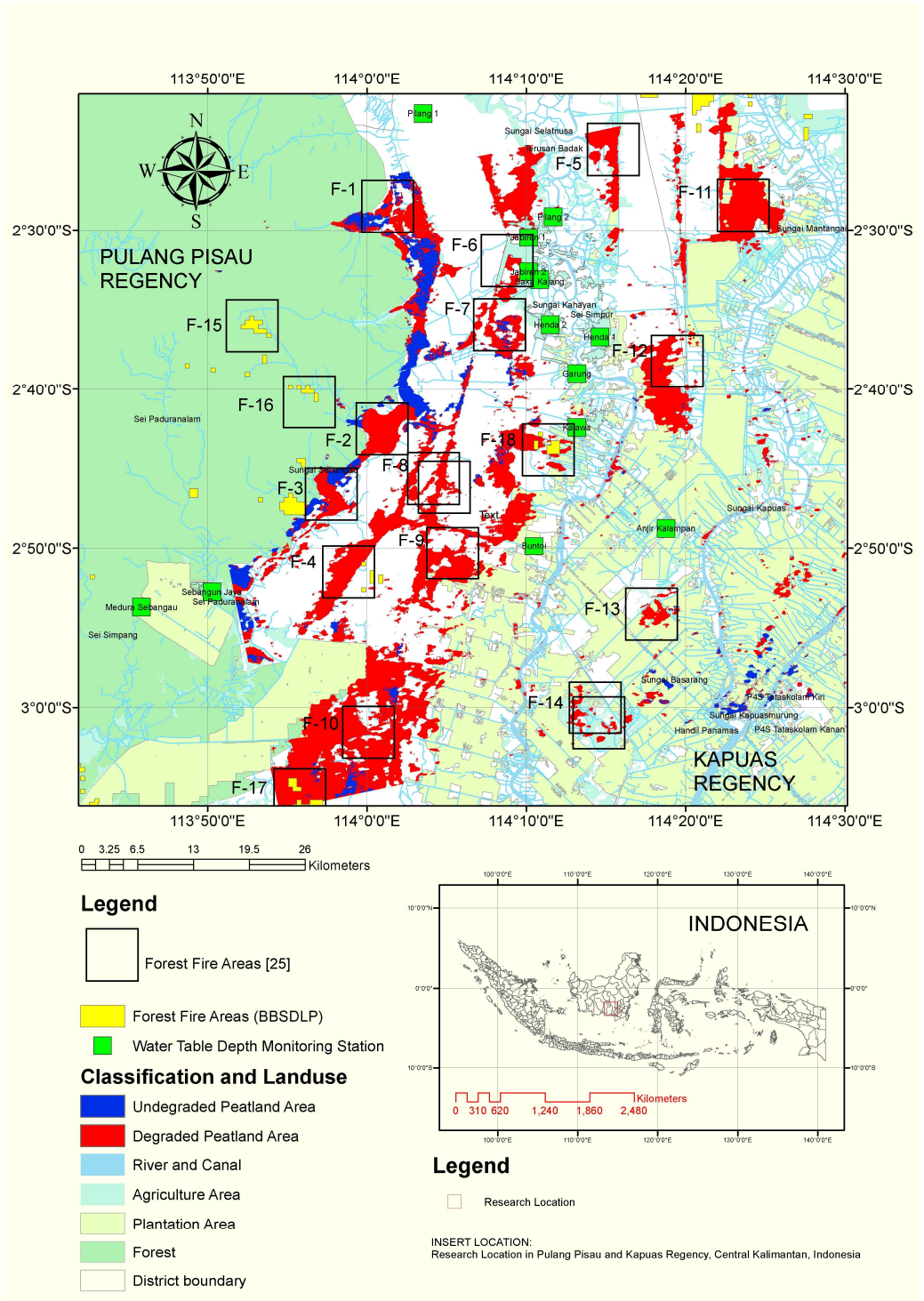

Figure 4. 14. Map of degraded peatland areas, and position of groundwater level station related to the forest fire in Pulang Pisau and Kapuas Regency in Kalimantan [24].

Based on the fact above, the detection by SAR interferometry of degraded peatland areas in relation to forest fires is cover wider than the groundwater (WT) depth stations. This phenomenon is probably because of a trend that forest fires typically arise in open areas [31] that are easily detected using SAR interferometry [28] and possibly in-built groundwater (WT) depth stations frequently in the vegetation field as shown in Figure 4.14.

Figure 4. 15. Forest fire in the peatland area, Kalimantan that occurred in the open area [73].

SAR interferometry by ALOS-2 PALSAR-2 may effectively and accurately map degraded peatland; the weakness is the detailed time unit because it was developed on the basis of yearly unit analysis.

This technique, therefore, still needs field calculation in situ. Thus, the combination of them was suggested to achieve complementary outcomes in the monitoring of degraded peatland areas.

Based on the facts above related to the application of DiNSAR identification to detect peatland that is prone to burning, it can be noted as follows:

1. In general, the results of processing with Interfemoteric SAR can show which areas are degraded, and overlay results are areas that experience forest fires; however, this method has a weakness because it can only simulate on a macro scale on an annual level.
2. This research also has limitations because, especially in the Kalimantan field area, it cannot show subsidence measurement data in the field as a comparison. The field comparison is only associated with groundwater level data, which is only represented by two observation stations in Jabiren 1 and Jabiren 2.
3. In order to observe flammable peatlands, it is recommended to use the results of the InSAR analysis as an initial method and then proceed with the installation of a groundwater table station for data validation.
4. The backscattering coefficient also has a strong relationship with the groundwater table, especially for HH and VV polarization, so that identification of the groundwater level by using the future polarimetric SAR also has the potential to be done.[34].

Chapter 5. Conclusion

The study successfully identified the peat fire risk area by using three layers of the new impedance model method, which involves the inclusion of soil roughness parameters as a layer between air and ground surface and as a novelty of this analysis. In Horizontal-horizontal Polarization ALOS-2 PALSAR-2 results. Fire Risk Area of peatland was identified as a back-scattering value between –11.5 to– 17.29 dB. Correlation between the simulation of the backscattering coefficient and ALOS-2 data measurement backscattering coefficient has given a high correlation, 0.8.

Based on the result, DInSAR also established the peat fire risk area successfully following the simulation of the groundwater table. The position with a groundwater table over 40 cm is related to the risk area of the peat fire. The correlation test also resulted in significant results for Pair A 0.71 and Pair B 0.85. Both the impedance model and DInSAR approaches provided a considerable achievement for the identification of the peat-fire hazard area and showed a high correlation coefficient. The blend of the current impedance model system with the DInSAR approach is shown to be a benefit in the form of accurate research results because of cross-checks.

Application of ALOS-2 PALSAR-2 interferometry to classify degraded peatlands gives 88 percent of the effective level related to a forest fire. This result is more

effective compare using groundwater table stations that only cover 5% of the fire event.

The combination of SAR interferometry and a WT depth control system in real-time is the best way to identify deteriorated forest fire-related peatlands in Indonesia. We suggest that the results of SAR interferometry be considered in deciding the position of the WT depth system station, as it may be maximized for peatland monitoring that is degraded and susceptible to burnt. The Indonesian government can also use this research as a guide for paying attention to the damaged areas to prevent forest fires.

Chapter 6. Summary

6.1. Summary of The Work

The research work presented in this report can be summarized as follows:

1. The use of SAR for applications, especially in the context of monitoring on peatlands in Indonesia becomes a matter of importance to note. It considering the superiority of Synthetic Aperture Radar (SAR) that can be used in all regions, both in rainy and cloudy conditions. The weather condition of Indonesia which is in the tropics and also always cloudy,
2. Forest fires in Indonesia is an annual phenomenon that must be anticipated. Many alternative methods and sensors are needed to be able to monitor the condition of flammable peatlands in Indonesia.
3. In this research, the use of the impedance model method using Synthetic Aperture Radar (SAR) ALOS-2 PALSAR-2 data has successfully shown good performance.
4. The study successfully identified the peat fire risk area by using three layers of the new impedance model method, which involves the inclusion of soil roughness parameters as a layer between air and ground surface and as a novelty of this analysis. In HH Polarization ALOS-2 PALSAR-2 results, Peat Fire Risk Area was identified as a back-scattering value between –11.5 to– 17.29 dB. The relationship between the simulation of the backscattering coefficient and the ALOS-2 PALSAR-2 data measurement backscattering coefficient has given a high correlation, 0.8.
5. The study also successfully identified the peat fire risk area by DInSAR approach, based on the position with a groundwater table over 40 cm is related to the risk area of the peat fire. The correlation test also resulted in significant results for Pair A 0.71 and Pair B 0.85.
6. Application of interferometry SAR to classify degraded peatlands gives effectivity level 88 percent. On the other side, the groundwater level station smaller only covers 5% event of a fire.

6.2. Contribution

The contributions of this research are summarized as follows:

1. We have developed a novel method to detect peat fire risk areas based on transmission line theory three layers, including soil roughness.
2. We have developed a method to detect peat fire risk areas based on Differential Interferometry Synthetic Aperture Radar (DInSAR).
3. We have made comparisons and evaluations to detect the peat fire risk area in peatland base on DInSAR and groundwater/water table depth stations.
4. We have measured the dielectric constant of peatland.
5. We have simulated and measured the backscattering coefficient of peatland.
6. We measured the surface roughness of peatland.
7. We measured the groundwater table of peatland.

6.3. Originality

The originality of the work lies in:

1. Realization of the idea to identify the peat fire risk area based on the polarimetric concept and impedance model of three layers: air, soil roughness, and peatland.
2. Realization of the idea to identify the peat fire risk area based on SAR interferometry
3. SAR Interferometry (DInSAR) and groundwater table (WT) monitoring stations comparison to identify degraded peatland areas related to the forest fire.

6.4. Significance of Work

The significance of the work lies in

1. The proposed to identify the peat fire risk area based on the polarimetric concept of impedance model of three-layer: air, soil roughness, and peatland.
2. The proposed to identify the peat fire risk area based on DInSAR of L-Band frequency combination with Woosten model.
3. The proposed to compare the identification degraded peatland area between SAR Interferometry (DInSAR) and groundwater table (WT) monitoring stations.

6.5. Limitation of Research

The limitation of the research as follows:

1. Field sampling is not precisely the same as satellite recording due to difficulties in accessing sample point positions.
2. There are not many points of observation due to time constraints, which are only approximately seven days before and after recording satellite data.
3. This research also has limitations because, especially in the Kalimantan field area, it cannot show subsidence measurement data in the field as a comparison. The field comparison is only associated with groundwater level data, which is only represented by two observation stations in Jabiren 1 and Jabiren 2.

6.6. Future Work

Taking advantage of the use of SAR data related to peatland study, the challenges worth the effort in the future may include but not limited to:

1. Improve the model by replacing the soil roughness data from to field to the soil roughness model from SAR images to simplify the technic.
2. Identify the relationship between groundwater table, soil moisture, and scattering by more comprehensive data.
3. Study on the comparative between L-Band and C-Band to identify peat fire risk areas
4. Calculate the relationship between dielectric constant and soil parameter in peatland.
5. Make an algorithm retrieval model of soil parameter in peatland by using SAR
6. Calculation of carbon emission from peatland based on DInSAR approach
7. Develop an artificial intelligence system to monitor peatland in Indonesia based on SAR data.

Appendix – List of Publications

1. Peer-reviewed Journal Papers

1. J. Widodo, Y. Izumi, A. Takahashi, H. Kausarian, D. Perissin, and J. T. Sri Sumantyo, "Detection of Peat Fire Risk Area Based on Impedance Model and DInSAR Approaches Using ALOS-2 PALSAR-2 Data," IEEE Access, Vol. 7, pp. 22395-22407, 2019, DOI: 10.1109/ACCESS.2019.2899080. Publication date: 13 February 2019

2. J. Widodo, A. Sulaiman, A. Awaluddin, A. Riyadi, M. Nasucha, D. Perissin, J.T. Sri Sumantyo, "Application of SAR Interferometry Using ALOS-2 PALSAR-2 Data as Precise Method to Identify Degraded Peatland Areas Related to Forest Fire," Geosciences, Vol.9, No.11, pp.1-14, 2019. DOI: 10.3390/geosciences9110484. Publication date: 16 November 2019

2. Conference Papers

1. J. Widodo, Y. Izumi, Babag Purbantoro, J.T. Sri Sumantyo, "Application of Interferometry Synthetic Aperture Radar for Carbon Loss Estimation in Peatland Area," Future Earth Kick-off Workshop, Chiba University, 2 March 2017
2. J. Widodo, A. Herlambang, A. Sulaiman, D. Perissin, Yohandri, P. Razi, J.T. Sri Sumantyo, "Land Subsidence rate Analysis of Jakarta Metropolitan Region based on DInSAR processing of Sentinel data C-Band frequency," Journal of Physic, Conference Series, International Conference on Research and Learning of Physics (ICRLP 2018), Padang, Indonesia, 9-10 August 2018.

3. J. Widodo, Y. Izumi, A. Takahashi, Husnul Kausarian, J.T. Sri Sumantyo, “Detection of Dry-Flammable Peatland Area by Using Backscattering Coefficient Information of ALOS-2 Data L-Band Frequency,” PIERS in Toyama Conference 2018, Toyama, Japan, 1-4 August 2018
4. J. Widodo, Y. Izumi, H. Kausarian, I. Riyanto, J.T. Sri Sumantyo, “Peat Soil Acidity Retrieval Model Based on Surface Scattering of ALOS-2 PALSAR-2 Data,” Indonesia Japan Joint Scientific Symposium 2018, Jakarta, Indonesia, 9-11 October 2018
5. J. Widodo, A. Takahashi, J.T. Sri Sumantyo, “Detection of Forest Fire Risk Area in Peatland Using ALOS-2 PALSAR-2 Data,” The 3rd Institute for Global Prominent Research Symposium, Chiba University, November 6, 2018
6. J. Widodo, J.T. Sri Sumantyo, A. Sulaiman, D. Perisin, K. Nishi, R. Pakhrur, “Peatland Assessment Based on DInSar Approach by Using ALOA-2 PALSAR-2 Data in Kalimantan Indonesia,” Japan Geoscience Union Meeting, Japan, May 26-30, 2019
7. J. Widodo, A. Takahashi, Y. Izumi, P. Sitompul, H. Kausarian, A. Suryadi, P. Razi, A. Munir, D. Perissin, J.T. Sri Sumantyo, “Application of Polarimetric Decomposition and Interferometric SAR by Using ALOS-2 PALSAR-2 Data to Detect Potential of Combustible Peatland Area,” PIERS in Rome Conference, 17 – 20 June 2019

8. J. Widodo, P. Sitompul, A. Munir, R. Abouelmagd, P. Razi, D. Perissin, J.T. Sri Sumantyo, “Land Deformation of Surabaya City, Indonesia Based on DInSAR and Multiple Images Interferometric SAR,” PIERS in Xiamen Conference, 17 – 20 December 2010
9. J. Widodo, D. Perissin, J.T. Sri Sumantyo, “DInSAR Method and Ground Water Table Stations Contrast for Detection of Combustible Peat Areas,” SeMIRES, Chiba University, February 21, 2020
10. P. Razi, J.T. Sri Sumantyo, K. Nishi, J. Widodo, A. Munir, F. Febriany, “Effect of Earthquake Intensity to Land Deformation Observed from Space,” 2019 PhotonIcs & Electromagnetics Research Symposium-Spring (PIERS-Spring), IEEE, 2123-2128, June 17, 2019
11. H. Kausarian, J.T. Sri Sumantyo, A. Takahashi, J. Widodo, Y. Izumi, “Application of microwave remote sensing polarimetric synthetic aperture radar for the new geological map of peatland distribution humidity and its sample properties in Regency of Siak, Riau Province, Indonesia,” Journal of Physics: Conference Series, 1363, November 2019
12. M. Nasucha, J.T. Sri Sumantyo, C.E. Santosa, P. Sitompul, A.H. Wahyudi, Y. Yu, J. Widodo, “Computation and Experiment on Linearly and Circularly Polarized Electromagnetic Wave Backscattering by Corner Reflectors in an Anechoic Chamber,” Computation, Volume 7, Issue 4, Page 55. 24 September 2019

13. H. Nusantara, RA Rizka Qori Yuliani Putri, J Widodo, A. Munir, "Multi-stage Ku-band waveguide BPF using CSRR-based dielectric frequency selective structure," IEEE, 3883-3886 June 17, 2019
14. Y. Izumi, J. Widodo, H. Kausarian, S. Demirci, A. Takahashi, J.T. Sri Sumantyo, M.Sato, "Soil moisture retrieval by means of adaptive polarimetric two-scale two-component model with fully polarimetric ALOS-2 data," IGARSS 2018-2018 IEEE International Geoscience and Remote Sensing Symposium, IEEE, 4619-4622, July 22, 2018.
15. Y. Izumi, J. Widodo, H. Kausarian, S. Demirci, A. Takahashi, P. Razi, M. Nasucha, H. Yang, J.T. Sri Sumantyo, "Potential of soil moisture retrieval for tropical peatlands in Indonesia using ALOS-2 L-band full-polarimetric SAR data," International Journal of Remote Sensing, Volume 40, Issue 15, p5938-5956, Taylor & Francis, August 3, 2019
16. P.Razi, J.T. Sri Sumantyo, D. Perissin, A.Putra, J. Widodo, B. Purbantoro, I. Dewata, "Ground deformation measurement of Sinabung vulcano eruption using DInSAR technique," Journal of Physics: Conference Series. Volume 1185, Issue 1, p012008, April 2019.
17. P. Razi , J.T. Sri Sumantyo, J. Widodo, Y. Izumi and D. Perissin " Land Deformation Monitoring Using D-Insar Technique During Lombok Earthquake Observed By Sentinel-1A/B" GEOMATE Journal, Volume 19, Issue 73, 2020

Bibliography

[1] G. E. Susilo, K. Yamamoto, T. Imai, and T. Inoue, "Effect of Canal Damming on the Surface Water Level Stability in the Tropical Peatland Area," vol. 11, no. 4, pp. 263–274, 2013.

[2] E. L. A. Law, B. R. A. Bryan, E. R. I. K. Meijaard, T. H. Mallawaarachchi, and M. A. Struebig, "Ecosystem services from a degraded peatland of Central Kalimantan : implications for policy, planning, and management," *Ecol. Appl.*, vol. 25, no. 1, pp. 70–87, 2015.

[3] A. Hooijer, M. Silvius, H Wösten, and S. Page, "Assessment of CO2 emissions from drained peatlands in SE Asia," *Delft Hydraul. Delft, Netherlands*, pp. 1–41, 2006.

[4] H. Boehm and F. Siegert, "Ecological impact of the One Million Hectare Rice Project in Central Kalimantan, Indonesia, using Remote Sensing and GIS," *Pap. Present. 22nd Asian Conf. Remote Sens.*, vol. 5, no. November, p. 6, 2001.

[5] S. N. Qodriyatun, "Kebijakan penanganan kebakaran hutan dan lahan," *Info Singk. Kesejaht. Sos. Pus. Pengkaj. Pengolah. Data Informasi, DPR-RI*, vol. VI, no. 06, pp. 9–12, 2014.

[6] P. Hirschberger, "FORESTS ABLAZE Causes and effects of global forest fires," *WWF Deutschland, Berlin, Ger.*, 2017.

[7] A. J. Glauber and I. Gunawan, "The cost of fire. An economic analysis of Indonesia's 2015 fire crisis," *World Bank*, vol. 17, no. 5, pp. 403–408, 2015.

[8] W. J. D. Groot, R. D. Field, M. A. Brady, O. Roswintiarti, and M. Mohamad, "Development of the Indonesian and Malaysian fire danger rating systems," *Mitig. Adapt. Strateg. Glob. Chang.*, vol. 12, no. 1, pp. 165–180, 2007.

[9] G. Caccamo, L. A. Chisholm, R. A. Bradstock, and M. L. Puotinen, "Using remotely-sensed fuel connectivity patterns as a tool for fire danger monitoring," *Geophys. Res. Lett.*, vol. 39, no. 1, pp. 1–5, 2012.

[10] E. H. Chowdhury and Q. K. Hassan, "Operational perspective of remote sensing-based forest fire danger forecasting systems," *ISPRS J. Photogramm.*

Remote Sens., vol. 104, pp. 224–236, 2015.

[11] B. Leblon, "Monitoring forest fire danger with remote sensing," *Nat. Hazards*, vol. 35, no. 3, pp. 343–359, 2005.

[12] H. Sunuprapto and Y. A. Hussin, "a Comparison Between Optical and Radar Satellite Images in Detecting Burnt Tropical Forest in South Sumatra, Indonesia," *Int. Arch. Photogramm. Remote Sens.*, vol. XXXIII, no. B7, pp. 580–587, 2000.

[13] L. L. Bourgeau-Chavez, E. S. Kasischke, and M. D. Rutherford, "Evaluation of ERS SAR Data for Prediction of Fire Danger in a Boreal Region," *Int. J. Wildl. Fire*, vol. 9, no. 3, pp. 183–194, 2000.

[14] L. L. Bourgeau-Chavez *et al.*, "Remote monitoring of spatial and temporal surface soil moisture in fire disturbed boreal forest ecosystems with ERS SAR imagery," *Int. J. Remote Sens.*, vol. 28, no. 10, pp. 2133–2162, 2007.

[15] M. A. Tanase, R. Panciera, K. Lowell, and C. Aponte, "Monitoring live fuel moisture in semiarid environments using L-band radar data," *Int. J. Wildl. Fire*, vol. 24, no. 4, p. 560, 2015.

[16] Y. Izumi *et al.*, "Potential of soil moisture retrieval for tropical peatlands in Indonesia using ALOS-2 L-band full-polarimetric SAR data," *Int. J. Remote Sens.*, vol. 40, no. 15, pp. 5938–5956, 2019.

[17] M. Osaki and N. Tsuji, *Tropical Peatland Ecosystems*, 2016th ed. Springer, Japan.

[18] J. Widodo, Y. Izumi, A. Takahashi, H. Kausarian, H. Kuze, and J. T. S. Sumantyo, "Detection of Dry-Flammable Peatland Area by Using Backscattering Coefficient Information of ALOS-2 Data L-Band Frequency," *Prog. Electromagn. Res. Symp.*, vol. 2018-August, pp. 916–920, 2018.

[19] A. P. Dimitrakopoulos and K. K. Papaioannou, "Flammability assessment of Mediterranean forest fuels," *Fire Technol.*, vol. 37, no. 2, pp. 143–152, 2001.

[20] Government of Indonesia, "Government Regulation number 71 of year 2014 about protection and management of peat ecosystems," pp. 1–25, 2014.

[21] Government of Indonesia, "Government regulation 57 of year 2016 about ammendment to Government Regulation number 71 of year 2014 about

protection and management of peat ecosystems," 2016.

[22] P. Mishra , S. Goel and D. Singh "An Impedance Based Approach To Determine Soil Moisture Using Radarsat-2 Data Department of Electronics and Computer Engineering, Indian Institute of Technology Roorkee," pp. 2724–2727, 2013.

[23] J. T. Sri Sumantyo, R. Tateishi, and N. Takeuchi, "Estimation of burnt coal seam thickness in central Borneo using JERS-1 SAR data," *Int. J. Remote Sens.*, vol. 24, no. 4, pp. 879–884, 2003.

[24] J.T. Sri Sumantyo, R. Tateishi, and N. Takeuchi, "A physical method to analyse scattered waves from burnt coal seam and its application to estimate thickness of fire scars in central Borneo using L-band SAR data," *Int. J. Remote Sens.*, vol. 24, no. 15, pp. 3119–3136, 2003.

[25] H. Al-Bilbisi, R. Tateishi, and S. S. J. Tetuko, "A technique to estimate topsoil thickness in arid and semi-arid areas of north-eastern Jordan using synthetic aperture radar data," *Int. J. Remote Sens.*, vol. 25, no. 19, pp. 3873–3882, 2004.

[26] H. Kausarian, J.T. Sri Sumantyo, H. Kuze, J. Aminuddin, and M. M. Waqar, "Analysis of Polarimetric Decomposition, Backscattering Coefficient and Sample Properties for Identification and Layer Thickness Estimation of Silica Sand Distribution using L Band Synthetic Aperture Radar," no. 113, pp. 1–43, 2016.

[27] A. J. Jaroci´nska, S. M. De Jong, and M. Schaepman, *Remote Sensing and Digital Image Processing Volume 20 EARSeL Series Editor*. .

[28] Z. Zhou, "PhD Thesis: The applications of InSAR time series analysis for monitoring long-term surface change in peatlands," pp. 1–231, 2013.

[29] Z. Zhou, Z. Li, S. Waldron, and A. Tanaka, "Monitoring peat subsidence and carbon emission in Indonesia peatlands using InSAR time series," *Int. Geosci. Remote Sens. Symp.*, vol. 2016-Novem, pp. 6797–6798, 2016.

[30] J. H. M. Wösten, A. B. Ismail, and A. L. M. Van Wijk, "Peat subsidence and its practical implications: A case study in Malaysia," *Geoderma*, vol. 78, no. 1–2, pp. 25–36, 1997.

[31] M. Taufik, A. A. Veldhuizen, J. H. M. Wösten, and H. A. J. van Lanen, “Exploration of the importance of physical properties of Indonesian peatlands to assess critical groundwater table depths, associated drought and fire hazard,” *Geoderma*, vol. 347, no. February, pp. 160–169, 2019.

[32] R. Weiss, N. J. Shurpali, T. Sallantaus, R. Laiho, J. Laine, and J. Alm, “Simulation of water table level and peat temperatures in boreal peatlands,” *Ecol. Modell.*, vol. 192, no. 3–4, pp. 441–456, 2006.

[33] N. T. Girkin, B. L. Turner, N. Ostle, J. Craigon, and S. Sjögersten, “Root exudate analogs accelerate CO2 and CH4 production in tropical peat,” *Soil Biol. Biochem.*, vol. 117, no. September 2017, pp. 48–55, 2018.

[34] N. T. Girkin, B. L. Turner, N. Ostle, and S. Sjögersten, “Composition and concentration of root exudate analogs regulate greenhouse gas fluxes from tropical peat,” *Soil Biol. Biochem.*, vol. 127, no. June, pp. 280–285, 2018.

[35] J. P. Krüger, J. Leifeld, S. Glatzel, S. Szidat, and C. Alewell, “Biogeochemical indicators of peatland degradation - A case study of a temperate bog in northern Germany,” *Biogeosciences*, vol. 12, no. 10, pp. 2861–2871, 2015.

[36] D. Carless, D. J. Luscombe, N. Gatis, K. Anderson, and R. E. Brazier, “Mapping landscape-scale peatland degradation using airborne lidar and multispectral data,” *Landsc. Ecol.*, vol. 34, no. 6, pp. 1329–1345, 2019.

[37] L. Alshammari *et al.*, “Long-term peatland condition assessment via surface motion monitoring using the ISBAS DInSAR technique over the Flow Country, Scotland,” *Remote Sens.*, vol. 10, no. 7, 2018.

[38] B. Dahdal, “The use of interferometric spaceborne radar and GIS to measure ground subsidence in peat soils in Indonesia,” *Univ. Leicester*, p. 378, 2011.

[39] A. Hooijer *et al.*, “Subsidence and carbon loss in drained tropical peatlands,” *Biogeosciences*, vol. 9, no. 3, pp. 1053–1071, 2012.

[40] G. E. Susilo, K. Yamamoto, and T. Imai, “Modeling Groundwater Level Fluctuation in the Tropical Peatland Areas under the Effect of El Nino,” *Procedia Environ. Sci.*, vol. 17, pp. 119–128, 2013.

[41] G. of Indonesia, “Peraturan Pemerintah Republik Indonesia Nomor 71 Tahun 2014 tentang Perlindungan dan Pengelolaan Ekosistem Gambut (Government Regulation of the Republic of Indonesia No. 71/2014 on the Protection and Management of Peatland Ecosystems),” 2014.

[42] A. Usup, Y. Hashimoto, H. Takahashi, and H. Hayasaka, “Combustion and thermal characteristics of a peat fire in tropical peatland in Central Kalimantan, Indonesia,” vol. 14, pp. 1–19, 2004.

[43] J. O. Rieley, A. S. E. Page, and J. Jauhiainen, “Wise use of tropical peatlands: focus on Southeast Asia : Synthesis of results and conclusions of the UK Darwin Initiative and the EU INCO EUTROP, STRAPEAT AND RESTORPEAT Partnerships together with proposals for implementing wise use of tropical peatlands,” in *Alterra, Wageningen University*, 2005.

[44] J. Widodo *et al.*, “Application of SAR interferometry using ALOS-2 PALSAR-2 data as a precise method to identify degraded peatland areas related to forest fire,” *Geosci.*, vol. 9, no. 11, 2019.

[45] F. Ulaby and D. Long, *Microwave Radar, and Radiometric Remote Sensing*. The University of Michigan Press, 2014.

[46] G. BREIT and M. A. TUVE, “A test of t h e existence of t h e conducting layer,” *Phys. Rev.*, vol. 16, no. 1925, pp. 15–16, 1926.

[47] Y. K. Chan and V. C. Koo, “An Introduction to Synthetic Aperture Radar (SAR),” *Prog. Electromagn. Res. B*. Vol. 2, pp. 27–60, 2008.

[48] M. Gade, “Synthetic Aperture Radar Applications in Coastal Waters,” no. October, pp. 6–10, 2015.

[49] J. Van Zyl and Y. Kim, *Synthetic Aperture Radar Polarimetry*. Hoboken, New Jersey, USA: John Wiley & Sons, Inc., 2011.

[50] Y. Huang and K. Boyle, *ANTENNAS*. West Sussex, United Kingdom: A John Wiley and Sons, Ltd, Publication, 2008.

[51] H. C. Rumsey, G. A. Morris, R. R. Green, and R. M. Goldstein, “A radar brightness and altitude image of a portion of Venus,” *Icarus*, vol. 23, no. 1, pp. 1–7, 1974.

[52] S. H. ZISK, “A New, Earth-Based Radar Technique For The Measurement Of Lunar Topography,” *Moon*, vol. 4(3-4), pp. 296–306, 1972.

[53] R. M. Goldstein, H. A. Zebker, and C. L. Werner, “Satellite radar interferometry: Two-dimensional phase unwrapping,” *Radio Sci.*, vol. 23, no. 4, pp. 713–720, 1988.

[54] D. Massonnet *et al.*, “The displacement field of the Landers earthquake mapped by radar interferometry,” *Nature*, vol. 364, no. 6433, pp. 138–142, 1993.

[55] P. A. Rosen, “Synthetic aperture radar interferometry,” *Proc. IEEE*, vol. 88, no. 3, pp. 333–380, 2000.

[56] S. Lyons and D. Sandwell, “Fault creep along the southern San Andreas from interferometric synthetic aperture radar, permanent scatterers, and stacking,” *J. Geophys. Res. Solid Earth*, vol. 108, no. B1, pp. 1–24, 2003.

[57] A. Ferretti, C. Prati, and F. Rocca, “Nonlinear subsidence rate estimation using permanent scatterers in differential SAR interferometry,” *IEEE Trans. Geosci. Remote Sens.*, vol. 38, no. 5 I, pp. 2202–2212, 2000.

[58] A. Ferretti, C. Prati, and F. Rocca, “Permanent scatterers in SAR interferometry,” *IEEE Trans. Geosci. Remote Sens.*, vol. 39, no. 1, pp. 8–20, 2001.

[59] O. Mora, R. Lanari, J. J. Mallorquí, P. Berardino, and E. Sansosti, “A new algorithm for monitoring localized deformation phenomena based on small baseline differential SAR interferograms,” *Int. Geosci. Remote Sens. Symp.*, vol. 2, no. 11, pp. 1237–1239, 2002.

[60] A. Hooper, P. Segall, and H. Zebker, “Persistent scatterer interferometric synthetic aperture radar for crustal deformation analysis, with application to Volcán Alcedo, Galápagos,” *J. Geophys. Res. Solid Earth*, vol. 112, no. 7, pp. 1–21, 2007.

[61] P. Shanker and H. Zebker, “Persistent scatterer selection using maximum likelihood estimation,” *Geophys. Res. Lett.*, vol. 34, no. 22, pp. 2–5, 2007.

[62] K. N. Abbott, B. Leblon, G. C. Staples, D. A. Maclean, and M. E. Alexander, “Fire danger monitoring using RADARSAT-1 over northern boreal forests,”

Int. J. Remote Sens., vol. 28, no. 6, pp. 1317–1338, 2007.

[63] J. Widodo, Y. Izumi, A. Takahashi, H. Kausarian, D. Perissin, and J. T. Sri Sumantyo, "Detection of Peat Fire Risk Area Based on Impedance Model and DInSAR Approaches Using ALOS-2 PALSAR-2 Data," *IEEE Access*, vol. 7, pp. 22395–22407, 2019.

[64] D. Perissin, "Interferometric SAR multitemporal processing: Techniques and applications," *Remote Sens. Digit. Image Process.*, vol. 20, pp. 145–176, 2016.

[65] T. Motohka, O. Isoguchi, M. Sakashita, and M. Shimada, "ALOS-2 PALSAR-2 Cal / Val Updates," 2018.

[66] J. D. Carlson and R. E. Burgan, "Review of user's needs in operational fire danger estimation: The Oklahoma example," *Int. J. Remote Sens.*, vol. 24, no. 8, pp. 1601–1620, 2003.

[67] J. Jung, D. J. Kim, M. Lavalle, and S. H. Yun, "Coherent change detection using temporal decorrelation model for volcanic ash detection," *Int. Geosci. Remote Sens. Symp.*, vol. 2016-Novem, no. 10, pp. 3394–3397, 2016.

[68] M. Wei and D. T. Sandwell, "Decorrelation of L-Band and C-Band Interferometry Over Vegetated Areas in California," vol. 48, no. 7, pp. 2942–2952, 2010.

[69] H. A. Zebker, S. Member, and J. Villasenor, "Decorrelation in Interferometric Radar Echoes," vol. 30, no. 5, pp. 950–959, 1992.

[70] J. I. H. Askne, P. B. G. Dammert, L. M. H. Ulander, and G. Smith, "C-Band Repeat-Pass Interferometric SAR Observations of the Forest," vol. 35, no. 1, pp. 25–35, 1997.

[71] E. C. Atwood, S. Englhart, E. Lorenz, W. Halle, W. Wiedemann, and F. Siegert, "Detection and Characterization of Low-Temperature Peat Fires during the 2015 Fire Catastrophe in Indonesia Using a New High-Sensitivity Fire Monitoring Satellite Sensor (FireBird)," *PLoS One*, vol. 11, no. 8, p. e0159410, Aug. 2016.

[72] W. R. Institute, "Intense Forest Fires Threaten to Derail Indonesia's Progress in Reducing Deforestation," vol. October 7, pp. 1–8, 2019.

[73] https://saveourborneo.org/lahan-istimewa-punya-siapa-2, Accesed June 1, 2020, Time: 23.05 PM